Development of an Energy Spectrum Measurement Deployment Device for a CubeSat

a project presented to

The Faculty of the Department of Aerospace Engineering

San José State University

in partial fulfillment of the requirements for the degree

Master of Science in Aerospace Engineering

by

Kendrick Wong

May 2026

approved by

Dr. Periklis Papadopoulos

Faculty Advisor



© 2026
Kendrick Wong
ALL RIGHTS RESERVED

ABSTRACT

Development of an Energy Spectrum Measurement Deployment Device for a CubeSat

By Kendrick Wong

The increasing accessibility of CubeSat platforms has enabled low-cost scientific missions capable of performing meaningful measurements in Low Earth Orbit (LEO). This thesis presents the development and preliminary validation of an Energy Spectrum Measurement Deployment (ESMD) device designed for integration within a 1U CubeSat form factor. The primary objective of the device is to support in-orbit measurement of energetic particle environments while conforming to standard CubeSat mechanical, structural, and operational constraints.

A complete mechanical architecture for the CubeSat structure and internal payload accommodation was developed using CAD modeling techniques. Structural integrity under launch loading conditions was evaluated through finite element analysis (FEA), including static acceleration loading and modal analysis. The structure was modeled using aluminum 7075-T6, and results demonstrate acceptable stress, displacement, and natural frequency margins relative to typical launch vehicle environments, indicating that the CubeSat is expected to survive launch loads without structural failure or excessive dynamic response.

To assess external aerodynamic behavior, computational fluid dynamics (CFD) simulations were performed under representative Low Earth Orbit flow conditions. Drag force, drag coefficient, pressure distribution, and wake formation were evaluated using a Reynolds-averaged Navier–Stokes (RANS) formulation with a k-ε turbulence model. The resulting drag coefficient and force values were shown to be internally consistent with analytical drag relations, providing first-order validation of the numerical results.

Lastly, a 3D printed structure of the CubeSat was printed out. The structure was printed out using PETG through a 3D printing splicer. After the parts were manufactured together, the electronic payloads were assembled within the structure. This consisted of a PCB, Arduino, RADFET detector, and a data acquisition system. Verification and validation tests were then performed on the completed assembly.

Overall, this work demonstrates the feasibility of the proposed CubeSat deployment device from a structural and aerodynamic standpoint. The modeling and validation methods presented establish a foundation for future refinement, including higher-fidelity rarefied flow modeling, experimental verification, and on-orbit performance assessment

Acknowledgements

I would like to thank the faculty and staff of the Aerospace Engineering Department of San José State University. Special thanks to Dr. Nikos Mourtos and Dr. Periklis Papadopoulos for allowing me to pursue the idea of the ESMD. Without their support, guidance, and mentorship, this would not have been possible.

I would also like to thank my family for their undying support. In particular, I would like to thank my mother for her constant encouragement and my father for being an inspiration for engineering. Their endless support encourages me to pursue my passion for aerospace engineering.

Table Of Contents

ABSTRACT……...iii
Acknowledgements…….iv
Table of Contents……v
List of Figures…….vi
List of Tables…….vii
List of Symbols……viii
1. Introduction……..1
1.1 Motivation……..1
1.2 Literature Review……...1
1.2.1 CubeSat Background and Design Standards……...1
1.2.2 Radiation Environment in Low Earth Orbit (LEO).....2
1.2.3 Missions with Radiation Dectors……4
1.2.4 Miniaturized Radiation Detectors for CubeSats……..…...5
1.2.5 Orbit and Thermal Environment Modeling Tools……..……...….6
1.2.6 Software Tools Integrated in CubeSat Missions…….7
1.3 Project Proposal…….7
1.4 Methodology……..9
1.4.1 Project Scope……..9
1.4.2 Software Simulation……9
1.4.3 1U CubeSat Structural Construction……...9
1.4.4 Miniaturized Radiation Energy Detectors……10
1.4.5 Electronics…….10
1.4.6 Verification and Validation Testing……..…....11
2. ESMD Architecture……...……12
2.1 Structural Architecture…….12
2.1.1 CubeSat Skeleton……..14
2.1.2 Payload Selection…….15
2.1.3 Baseplate & Internal Mounting…….……16
2.2 Electrical Architecture.……20
2.2.1 Arduino Setup…….…..……20

2.2.2 PCB Architecture……..……26
2.2.3 Power Distribution System……...28
2.2.4 Data Acquisition & Storage……..……30
2.3 Radiation Detector…….…..31
2.3.1 Radiation Detector Setup……..……31
2.3.2 Detector Supply and Regulation……...34
3. Orbital Trajectory and Radiation Analysis……36
3.1 ANSYS System Tool Kit Setup……...……36
3.1.1 CubeSat Expected Trajectory……37
3.2 Orbital Mechanics Calculations……...……38
3.3 Radiation and Thermal Environment Analysis……39
3.3.1 Radiation Environment……40
3.3.2 Expected Radiation Response……...41
4. Structural Analysis.……42
4.1 CubeSat CAD Model Development…….42
4.2 Structural Finite Element Analysis……..43
4.2.1 Static Load Analysis…….43
4.2.2 Modal Natural Frequency Analysis……..47
4.3 Discussion of Structural Results……..54
5. Computational Fluid Dynamics…….55
5.1 CFD Setup…….……..……57
5.1.1 Geometry and Meshing.…….……..…57
5.1.2 Boundary Conditions and Flow Conditions.…….……59
5.2 Aerodynamic Drag Results…….…….…….…….…….…….…….60
5.3 Visualization Contours…….…….…….…….…….……..62
5.4 Discussion and Validation…….…….…….…….…….…….…….64
6. ESMD Assembly……...……66
6.1 Structure Assembly……..66
6.1.1 CubeSat Assembly……66
6.1.2 Base Panel Assembly……68
6.1.3 Payload Mounting Assembly……70

6.2 Electrical Assembly……72
6.2.1 Arduino Assembly……72
6.2.2 PCB and Power System Assembly……...73
6.2.3 Data Acquisition System ……..74
6.2.4 Radiation Sensor Assembly……..75
6.2.5 Wiring and Connection……77
7. Verification and Validation Testing……...…….78
7.1 Verification……...…78
7.1.1 Power On Test……...78
7.1.2 Subsystems Check……80
7.1.3 Data Connectivity Test……..81
7.2 Validation……83
7.2.1 Functional Integration Test……...83
7.2.2 Environmental Testing Conditions……...85
7.2.3 Data Validation Test…….…88
8. Conclusion and Future Recommendations……92
References……..93
Appendix A: Arduino Pin Mapping……...98
Appendix B: RadFET Pin Description……106
Appendix C: Radiation Detector Schematic……107
Appendix D: Micro SD Card Schematic…….108
Appendix E: Arduino Code…….109

List of Figures

Figure 1.1:CubeSat size and launch status [9].....2
Figure 1.2: Low earth orbit radiation contributors [1,7].....3
Figure 1.3: Energy deposition map captured by SATRAM [11].....5
Figure 1.4: Tool integration [10][14].....7
Figure 1.5: Example of integrating STK and ANSYS into MBSE.....8
Figure 1.6: Skeleton of cubesat from solidworks.....9
Figure 1.7: Fully built 1U cubesat [15].....10
Figure 2.1: ESMD structural architecture.....12
Figure 2.2: CAD design of the ESMD 1U cubesat.....14
Figure 2.3: Baseplate design.....16
Figure 2.4: Chassis wall.....17
Figure 2.5: Connector plate.....18
Figure 2.6: Support rod.....19
Figure 2.7: Electrical architecture.....20
Figure 2.8: Arduino layout.....22
Figure 2.9: Additional arduino circuit layout.....23
Figure 2.10: Arduino 2560 PCB trace layout.....24
Figure 2.11: Three-dimensional CAD of arduino.....25
Figure 2.12: Physical three-dimensional arduino.....25
Figure 2.13: Example of printed circuit board.....27
Figure 2.14: Simplified schematic of power distribution.....29
Figure 2.15: Flow chart of data.....31
Figure 2.16: Selected radiation board.....33
Figure 2.17: Pin configuration of radiation board.....34
Figure 2.18: Bias and regulation flow chart.....35
Figure 3.1: STK Starling satellite tracking.....37
Figure 3.2: Estimated tracking of starling over radiation areas.....40
Figure 4.1: Stress pattern contour.....44
Figure 4.2: Displacement pattern contour.....45
Figure 4.3: Strain pattern contour.....46
Figure 4.4: First mode shape.....48
Figure 4.5: Second mode shape.....48
Figure 4.6: Third mode shape.....49
Figure 4.7: Fourth mode shape.....49
Figure 4.8: Fifth mode shape.....50
Figure 4.9: Sixth mode shape.....50
Figure 4.10: Frequency vs mode number graph.....51
Figure 5.1: CubeSat in boundary condition box.....57

Figure 5.2: Mesh Generated……...58
Figure 5.3: Drag coefficient results……...60
Figure 5.4: Drag force results……...60
Figure 5.5: Flow direction……..62
Figure 5.6: Velocity contour……..63
Figure 5.7: Static pressure contour……...…….63
Figure 6.1: Printed top panel……...…….67
Figure 6.2: Laid out components……...67
Figure 6.3: Vertical corner beams……..68
Figure 6.4: Chassis walls……...69
Figure 6.5: Connector pins…….69
Figure 6.6: CubeSat skeleton completely assembled…….71
Figure 6.7: Arduino microcontroller used for the ESMD payload……72
Figure 6.8: PCB breadboard used……..73
Figure 6.9: 9V battery used for portable power……...……..73
Figure 6.10: SD card compatible with arduino……...……..74
Figure 6.11: Geiger counter used……...……..75
Figure 6.12: Completed electrical wiring……..77
Figure 7.2: First power-on test……...……79
Figure 7.3: Second power-on test……...…79
Figure 7.4: System integrated μSv/h plot……..84
Figure 7.5: Baseline test condition…….85
Figure 7.6: Metallic interaction test……...86
Figure 7.7: Test environment and solar conditions……87
Figure 7.8: Baseline test results…….88
Figure 7.9: Baseline histogram of radiation dose rate……..…….89
Figure 7.10: Metallic test result…….90
Figure 7.11: Metallic histogram of radiation dose rate……..90
Figure 7.12: Comparison of dose rate measurements……91

List of Tables

Table 1.1: CubeSat missions with spectrum measuring payloads……...……4
Table 1.2: Summary of radiation detector options for cubesats……...6
Table 1.3: Radiation detector cost……..……10
Table 2.1: Baseplate parameters……13
Table 2.2: Subsystem specifications……..……15
Table 2.3: Lists nominal voltage and current requirements……..….21
Table 2.4: Estimated power budget……..…….....……..….29
Table 3.1: TLE snippet……...38
Table 4.1: Modal analysis results…….....……..……..…….....51
Table 5.1: Representation of different conditions……..59
Table 6.1: ESMD structural components…….……..66
Table 7.1 :DAQ dataset received……...81

List of Symbols

Symbol	**Definition**	**Unit (SI)**
Greek Symbols		
ω	Natural circular frequency	rad/s
ε	Normal Strain	----------
k	Turbulent Kinetic Energy	m^2/s^s
p	Static Pressure	Pa
ρ	Fluid Density	kg/m^3
μ	Dynamic Viscosity	Pa*s
t	Time	s
v	Kinematic Viscosity	m^2/s
▽	Nabla operator (spatial differential operator)	----------
Subscripts		
σ_y	Yield Strength	Pa
σ_{max}	Max Stress	Pa
D	Drag	----------
E	Young's Modulus	Pa
FoS	Factor of Safety	----------
u_{max}	Max Displacement	mm
ref	Reference Value	----------
F_D	Aerodynamic Drag Force	----------
C_D	Drag Coefficient	----------

Acronyms		
CFD	Computational Fluid Dynamics	----------
ESMD	Energy Spectrum Measurement Device	----------
FEA	Finite Element Analysis	----------
LEO	Low Earth Orbit	----------
MBSE	Model-Based Systems Engineering	----------
PCB	Printed Circuit Board	----------
PETG	Polyethylene Terephthalate Glycol	----------
RANS	Reynolds-Averaged Navier-Stokes	----------
SPENVIS	Space Environment Information System	----------
STK	System Tool Kit	----------

1. Introduction

1.1 Motivation

The Low Earth Orbit (LEO) environment is covered by high-energy particles originating from solar activity, trapped radiation belts, and galactic cosmic rays. These particles contribute to a complex radiation spectrum that can degrade satellite electronics, induce single-event upsets, and shorten mission lifespans [1]. The ability to accurately characterize the energy spectrum in LEO has become increasingly important, especially with the rise in CubeSat deployments for both scientific and commercial applications.

Radiation damage is a key driver of mission failure in small spacecraft that lack the shielding and radiation-hardened electronics of larger satellites [2]. If we can understand the intensity and variability of the energy spectrum, this will allow mission designers to anticipate degradation effects better. Not only will this help mitigate degradation effects, but mission designers can also select appropriate electronic components and define shielding requirements [3]. This is especially critical for CubeSats. CubeSats typically operate in high-inclination orbits that expose them to the South Atlantic Anomaly (SAA) and the outer Van Allen belt [4], which are two zones of energetic charged particles that can degrade CubeSats and their lifespans.

CubeSats offer a unique opportunity for distributed, low-cost measurements of the radiation environment as they are extremely cost and time-efficient. Recent missions such as ELFIN and CeRES have demonstrated that compact detectors can be integrated into CubeSat platforms to perform meaningful spectrum measurements [5][6]. Using tools such as Solidworks, ANSYS, SPENVIS, STK, and Thermal Desktop, researchers can model expected radiation environments, the trajectory of CubeSats, and validate measurement methodologies before launch [7].

This thesis project focuses on the conceptual design, simulation, and partial development of a 1U CubeSat to measure the energy spectrum in LEO. The approach involves structural design using CAD and FEA, and radiation environment modeling using STK and Thermal Desktop. The ultimate goal is to demonstrate that CubeSat-class platforms can be used for targeted environmental data collection and pre-launch validation of radiation-tolerant satellite designs.

1.2 Literature Review

1.2.1 CubeSat Background and Design Standards

CubeSats were first introduced in 1999 by Cal Poly and Stanford University as a low-cost, modular satellite platform for academic use [8]. Since then, the standard 1U (10 × 10 × 10 cm) format has evolved into various sizes, including 3U, 6U, and 12U configurations that enable more complex missions. With improvements in miniaturization, CubeSats are now used for technology demonstration, remote sensing, and even interplanetary missions [9].

According to data from nanosats.eu, the majority of launched CubeSats are 3U or smaller, with 1U and 3U being the most common due to their balance of volume and deployability.

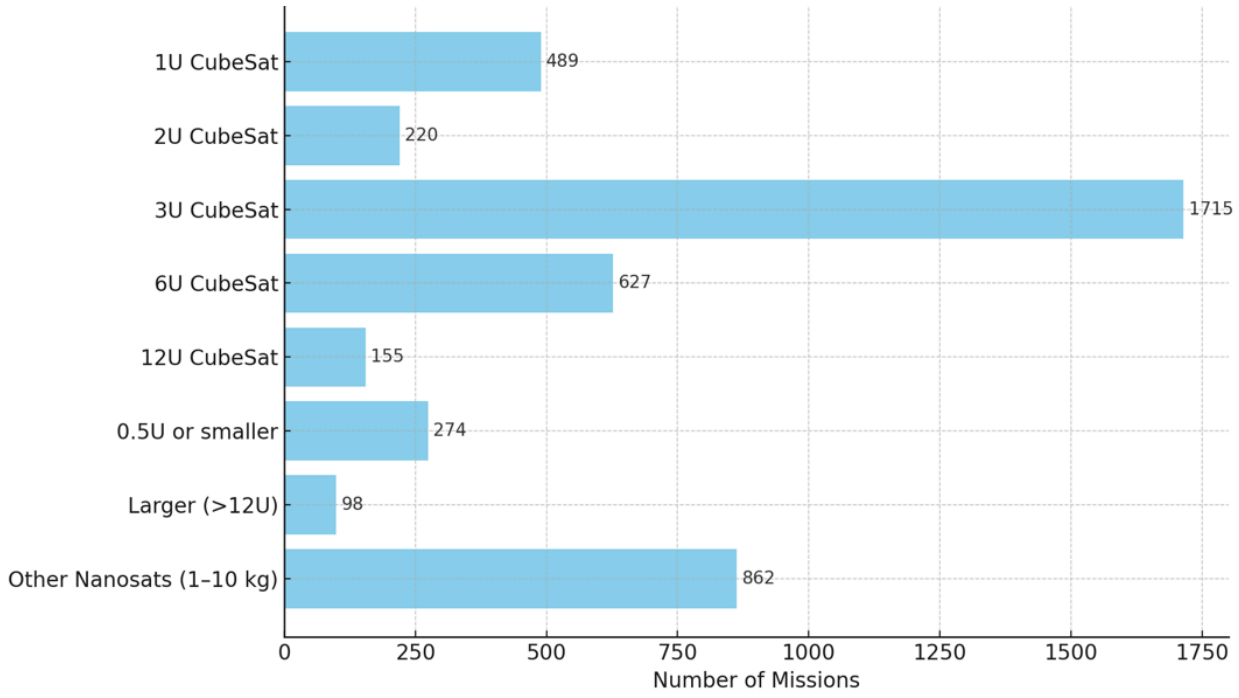


Figure 1.1 Cubesat size and launch status [9].

CubeSats can be seen as low-cost and time-efficient investments for space programs. The comparison to a CubeSat would be a conventional satellite. CubeSats can be used to contribute towards scientific research, educational projects, observation tools, remote sensing, and commercial applications such as internet services and GPS navigation.

1.2.2 Radiation Environment in Low Earth Orbit (LEO)

Low Earth Orbits presents a dynamic radiation environment dominated by solar energetic particles, galactic cosmic rays, and particles trapped in the Van Allen belts [10]. These radiation sources vary based on altitude, inclination, and solar activity, causing challenges for both satellite electronics and payloads. This can cause damage, which will result in a spacecraft's lifespan to drastically shortened.

If we understand the energy spectrum, we can incorporate this into a LEO CubeSat to measure these particles. Understanding the energy spectrum enables us to plan for crucial design in space electronics, shielding, and sensitive missions. NASA's AE9/AP9/SPM models and the ESA's SPENVIS tool are commonly used to predict time-averaged radiation levels, single event effects, total ionizing dose, and displacement damage dose (DDD) [11][12].

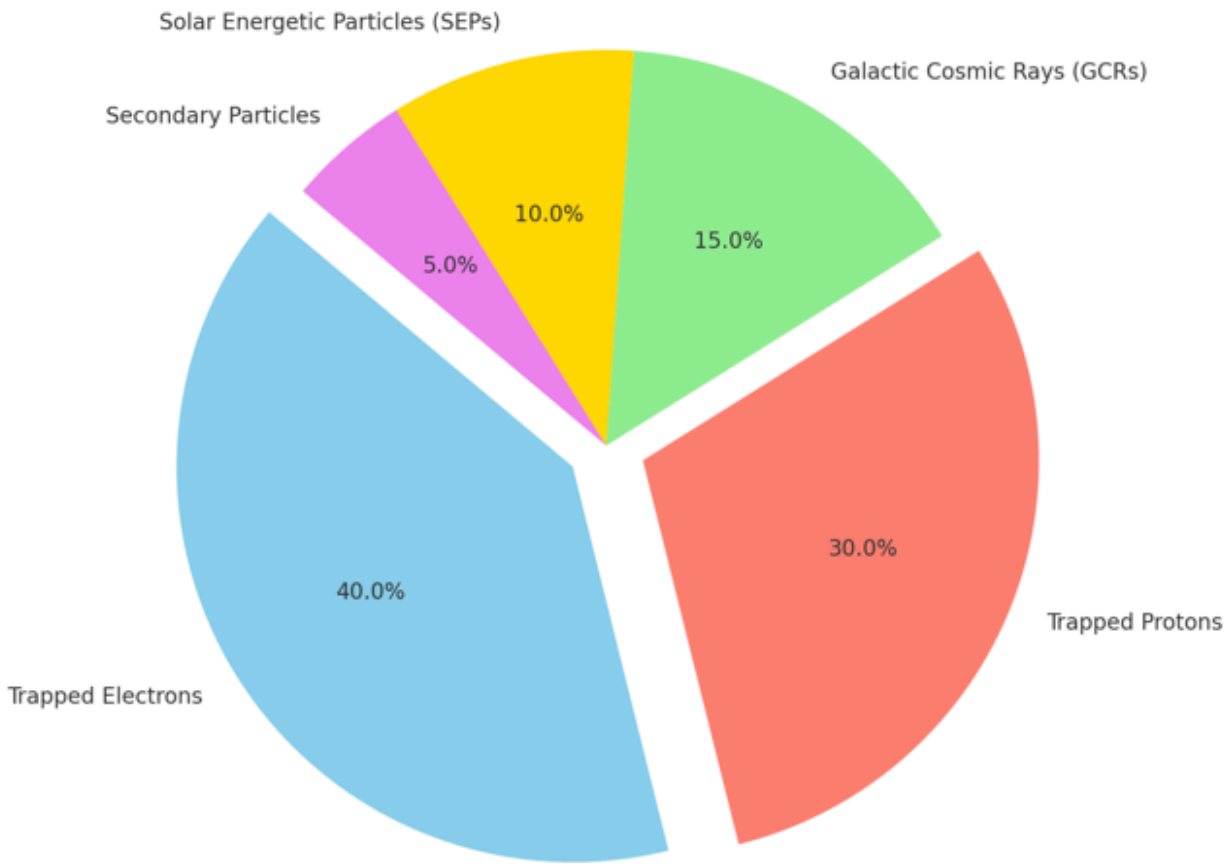


Figure 1.2 Low earth orbit radiation contributors [1,7]

1.2.3 Missions with Radiation Detectors

A growing number of CubeSat-class missions have successfully demonstrated the use of onboard radiation detectors in Low Earth Orbit. These missions validate the viability of small-form-factor sensors in capturing energetic particle flux, quantifying total ionizing dose, and mapping the space environment. One of the most well-known missions is ESA's PROBA-V, which carries the SATRAM payload. This payload is equipped with a Timepix pixel detector developed by CERN. The Timepix pixel detector operates in a sun-synchronous orbit, which is around 820 km from Earth. SATRAM has produced a detailed radiation map of Earth's trapped radiation belts and the South Atlantic Anomaly. This was captured using its Time-over-Threshold and Time-of-Arrival capabilities [11].

Another important mission is ELFIN, also known as Electron Losses and Fields Investigation. This mission was launched by UCLA and was designed to study relativistic electron precipitation from the outer Van Allen belt. ELFIN uses a combination of fluxgate magnetometers and energetic particle detectors to study space weather effects such as auroral substorms and electromagnetic wave–particle interactions [5].

Similarly, a mission named CeRES CubeSat (Compact Radiation Environment Spectrometer) was developed at the NASA Goddard Space Flight Center. CeRES integrates radiation dosimeters and sensors aimed at characterizing the local particle environment. It emphasizes miniaturization of traditional radiation instruments while maintaining accuracy in mapping radiation intensity across orbit segments [6].

Several missions funded through the NASA CubeSat Launch Initiative (e.g., RadFXSat, RadSat-G) have focused specifically on the survivability and degradation of electronic components due to space radiation. These missions primarily use RadFET and PIN diode sensors to assess single-event effects and total dose damage on commercial off-the-shelf components [10], [11].

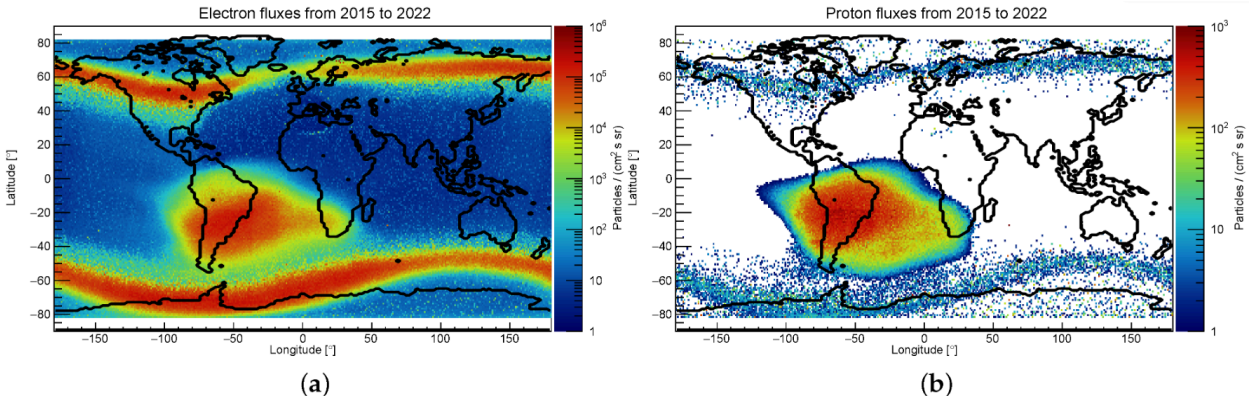
Table 1.1 CubeSat missions with spectrum measuring payloads

Mission	Sensor Type	Orbit Altitude	Objective focus
ELFIN	Electron Spectrometer	300-800 km LEO	Van Allen electron flux
CeRES	Charged Particle sensor	400-600 km LEO	Innr belt and SAA data
RadFXSat	RadFET, PIN Diode	LEO	SEE/TID monitoring
PROBA-V	Particle Telescope	Sun-synch LEO	Radiation Model Validation

Together, these missions highlight the evolving role of CubeSats in complementing larger spacecraft missions by offering in-situ measurements of radiation belts, cosmic rays, and solar energetic particles—often at much lower cost and faster development timelines [4], [10].

1.2.4 Miniaturized Radiation Detectors for CubeSats

Modern CubeSats benefit from the integration of small, compact, and low-power radiation detectors that allow for precise particle flux and energy spectrum measurements without exceeding volume or power budgets. Among these, a Timepix-based hybrid pixel detector, developed by CERN, has demonstrated exceptional capabilities. These detectors feature a matrix of 256×256 pixels, which are each 55 µm², and operate in modes such as Time-over-Threshold for energy measurement and Time-of-Arrival for event timing, making them highly suitable for orbital radiation spectroscopy [12].



(a) (b)

Figure 1.3: Energy deposition map captured by SATRAM [11]

As mentioned earlier, another notable implementation is the SATRAM payload aboard ESA's PROBA-V satellite, which orbits in a sun-synchronous LEO at approximately 820 km altitude. Over more than a decade of operation, SATRAM has mapped global proton and electron flux levels, validating the resilience and spatial resolution of Timepix detectors in high-radiation zones such as the South Atlantic Anomaly (SAA) [11].

Table 1.2: Summary of radiation detector options for cubesats

Detector Type	Energy Resolution	Power Consumption	Suitability
Timepix	High	2-6 W	Excellent for spectral measurement
RADFET/ PIN Diodes	Low	Less than 0.1W	Nest for monitoring
Scintillator + SiPM	Medium	Around 1 W	Useful for high-energy photon detection

1.2.5 Orbit and Thermal Environment Modeling Tools

For radiation-detecting CubeSats, it is essential to evaluate not only the orbital exposure to radiation but also the thermal environment. Factors to look out for are coming from both direct solar illumination and internal power dissipation. We can evaluate these exposures with tools such as Systems Tool Kit (STK), SPENVIS, and Thermal Desktop with RadCAD, which are widely used in today's industry[10], [14].

In a standard workflow, the CubeSat's orbital parameters like inclination, altitude, and nodal precession can be modeled in STK. Modeling this in STK allows precise calculation of the time-varying position, eclipse patterns, and radiation exposure zones like the Van Allen belts or South Atlantic Anomaly [10]. These outputs can then be exported into SPENVIS to generate particle flux spectra, dose rates, and shielding effects based on AE9/AP9 radiation belt models or the ISO 15390 galactic cosmic ray standard [7].

The final layer involves importing these radiation and orbital inputs into Thermal Desktop with RadCAD, which computes the temperature profile of the CubeSat over time. By accounting for surface emissivity, heat conduction paths, and component power dissipation, RadCAD enables robust thermal modeling under realistic space conditions [14].

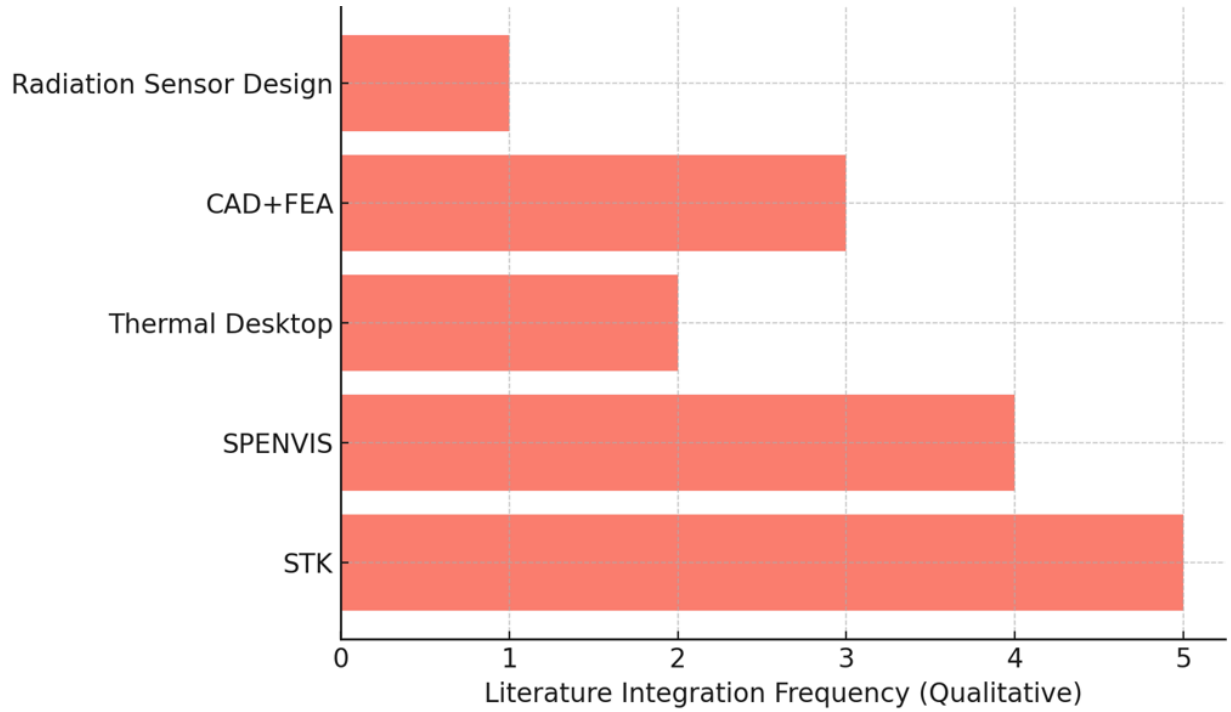


Figure 1.4: Tool integration [10][14]

1.2.6 Software Tools Integrated in CubeSat Missions

Although each modeling tool has been effectively used in prior studies, very few CubeSat projects, especially 1U-scale missions, have fully integrated them into a unified, mission-level simulation workflow. Most investigations in the literature focus on either orbital dynamics, radiation environment modeling, thermal analysis, or structural simulation in isolation, without linking them under a single systems design framework [10], [14].

For example, the PATCOOL project performed a detailed thermal simulation using Thermal Desktop, but it did not incorporate STK-derived orbital parameters or SPENVIS-based radiation flux into its analysis. This scenario led to siloed results that limited mission realism [15]. Similarly, other efforts, such as the ABEX MBSE framework, have integrated tools like STK, Simulink, and MATLAB under a model-based systems engineering approach, but these projects were constrained to specific subsystems and did not include payload-level sensor modeling [16].

This combination of modeling tools is visualized in Figure 1.5, which summarizes the relative frequency of toolchain integration across CubeSat studies. As shown, full-system coupling is very rare (fewer than 10%) in reviewed papers that performed comprehensive integration of orbital, thermal, and radiation environments into a single design loop [14].

This systems-level coupling not only enhances simulation accuracy but also provides essential insights into how CubeSats can be optimized for radiation environment sensing in Low Earth Orbit (LEO), especially in dynamic regions like the South Atlantic Anomaly and polar auroral zones [1], [4], [10].

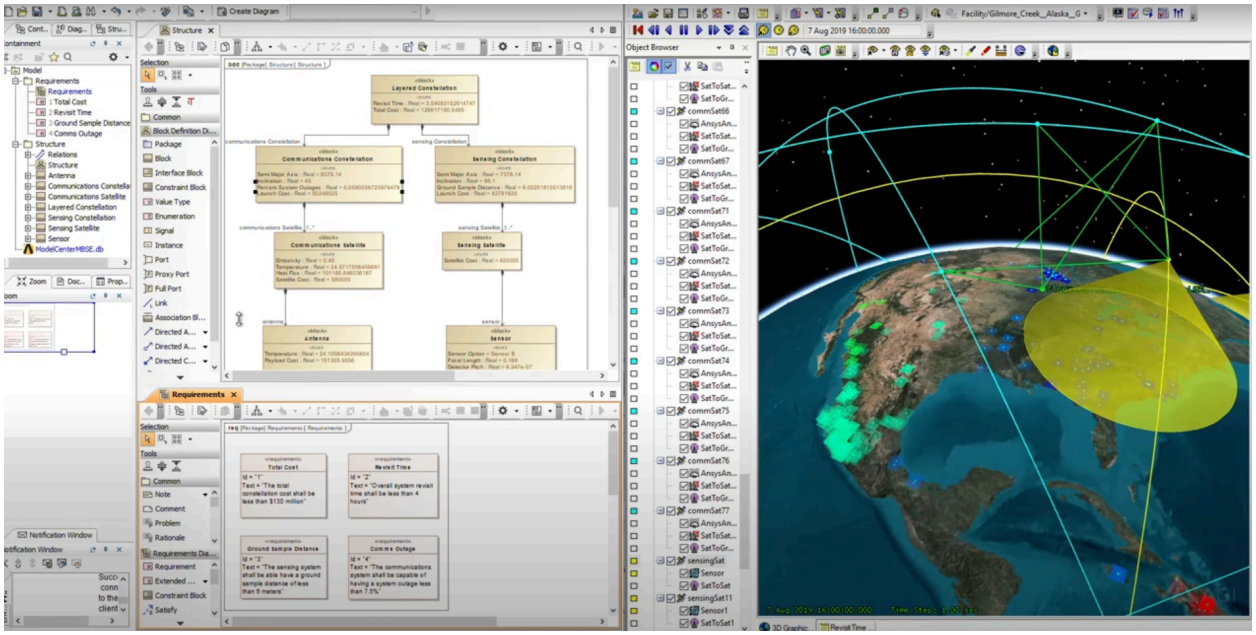


Figure 1.5: Example of integrating STK and ANSYS into MBSE

1.3. Project Proposal

The objective of this project is to develop and evaluate a mission-level simulation framework for a 1U CubeSat in LEO that will characterize the radiation energy spectrum using onboard miniaturized detectors. This will include modeling the satellite's orbit, environmental radiation exposure, thermal response, and structural analysis while integrating outputs across multiple tools such as STK, Thermal Desktop, RadCAD, and ANSYS FEA.

By implementing these software tools, this study can further assess the viability of radiation measurement in LEO by simulating the particle exposure based on time-varying orbital positions in STK, evaluate the payload thermal behaviors in Thermal Desktop, and analyze the structural behavior of the 1U CubeSat by performing modal analysis in ANSYS FEA. This unified approach will address the key gaps in our existing literature by linking space environment modeling with thermal and structural constraints. In the end, this will ultimately provide a validated path toward reliable CubeSat-based radiation mapping.

1.4. Methodology

1.4.1 Project Scope

The objective of the project is to model, simulate, and evaluate the performance of a 1U CubeSat capable of characterizing the energy spectrum of radiation in Low Earth Orbit. The methodology incorporates orbital modeling, structural construction, radiation detector integration, electronics design, and power system testing to ensure the feasibility of the mission concept.

1.4.2 Software Simulation

This step incorporates STK, Thermal Desktop, and FEA analysis into the 1U CubeSat. The first phase will rely on software-based modeling to establish the orbital trajectory and environmental conditions. STK will be used to propagate CubeSat orbits and map trajectories. Taking the trajectory data, we can import this into SPENVIS and generate maps of cosmic rays and solar energies based on our CubeSat's position. We can then incorporate this into Thermal Desktop with RadCAD and analyze the thermal loading and cycling throughout this orbit. Finally, FEA will be performed on the structural modes and will evaluate their response to each operation.

1.4.3 1U CubeSat Structural Construction

The next step will model the CubeSat's 1U frame and subsystems using CAD. After completing the CAD design, we can then import this into a splicing software to 3D print the skeleton structure of the 1U CubeSat. The dimensions will be 10x10x10 cm. This skeleton will accommodate payload detectors, solar panels, and PCBs while respecting CubeSat standards. As mentioned earlier, FEA simulations will validate the structural resilience to launch loads, vibration, and modal frequency requirements, ensuring compliance with rideshare launch standards.



Figure 1.6: Skeleton of cubesat from solidworks

1.4.4 Miniaturized Radiation Energy Detectors

This stage incorporates miniaturized radiation detectors into the CubeSat. Options such as Timepix, RadFETs, and PIN diodes will be evaluated based on power consumption, sensitivity, and payload constraints. The detectors will be positioned relative to solar cells and structural elements to maximize measurement fidelity while minimizing interference. Integration will draw on lessons learned from missions such as PROBA-V/SATRAM [11], ELFIN [5], and CeRES [6].

Table 1.3: Radiation detector cost

Radiation detector	Estimated power consumption	Cost
Timpepix	~2–6 W	$15,000–$25,000
RadFET/PIN Diodes	<0.1 W	$1,000–$3,000
Scintillator + SiPM	~1 W	$5,000–$10,000

1.4.5 Electronics

The electronic components necessary to operate the CubeSat will include a microcontroller unit, sun sensors, electric motors, solar panels, and power distribution boards. A PCB will be implemented to consolidate system functionality into a compact form factor. For flight readiness, all electrical components must operate within the thermal range of –65 °C to +125 °C, consistent with LEO requirements. This ensures the survivability of both the detectors and control electronics during eclipse-driven heating and cooling cycles.

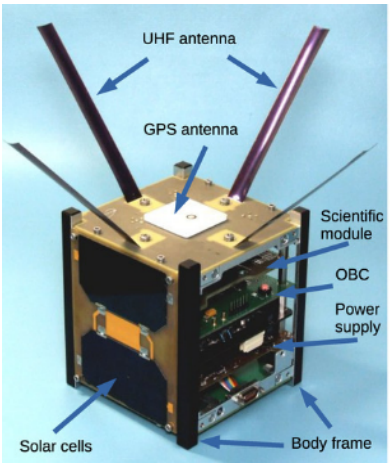


Figure 1.7: Fully built 1U cubesat [15].

1.4.6 Verification and Validation Testing

The final stage of the project will focus on verifying and validating that the CubeSat system operates as intended under ground-based conditions. Although in-orbit testing is beyond the scope of this study, functional tests will be conducted to ensure that the integrated payload, electronics, and software perform reliably. A grade of pass/fail will be given out in the following proposed V&V methodology testing:

Step 1: System Power-On Test

- Verify that the CubeSat system powers on correctly when connected to the power supply.
- Confirm that all subsystems, such as the detector, sensors, and PCB, initialize properly.

Step 2: Conditions of Testing

- Testing will be performed under controlled conditions to minimize variability.
- Testing sessions will be limited to a fixed time window, 11 AM–3 PM, to maintain maximum solar exposure.
- Weather conditions must be clear and sunny; testing will not occur during cloudy or rainy days.

Step 3: Data Collection

- The 1U CubeSat will be connected to a computer via USB
- Data logging software will be used to confirm real-time readouts from the radiation detector.
- Recorded outputs will be compared against expected baselines to verify system functionality.

Step 4: Additional Functional Tests

- A repeatability test will be performed. In this test, the CubeSat will perform multiple runs to ensure consistent results.
- Next, a power cycling test will occur. The CubeSat will be turned off and on several times to confirm stable reboot behavior.
- To ensure error logs, intentional disconnects will be introduced to test the system response and fault recovery.
- Data files generated during the test will be checked for completeness and proper formatting.
- Battery Performance will also be tested, verifying battery discharge/recharge cycles.

2. ESMD Architecture

2.1 Structural Architecture

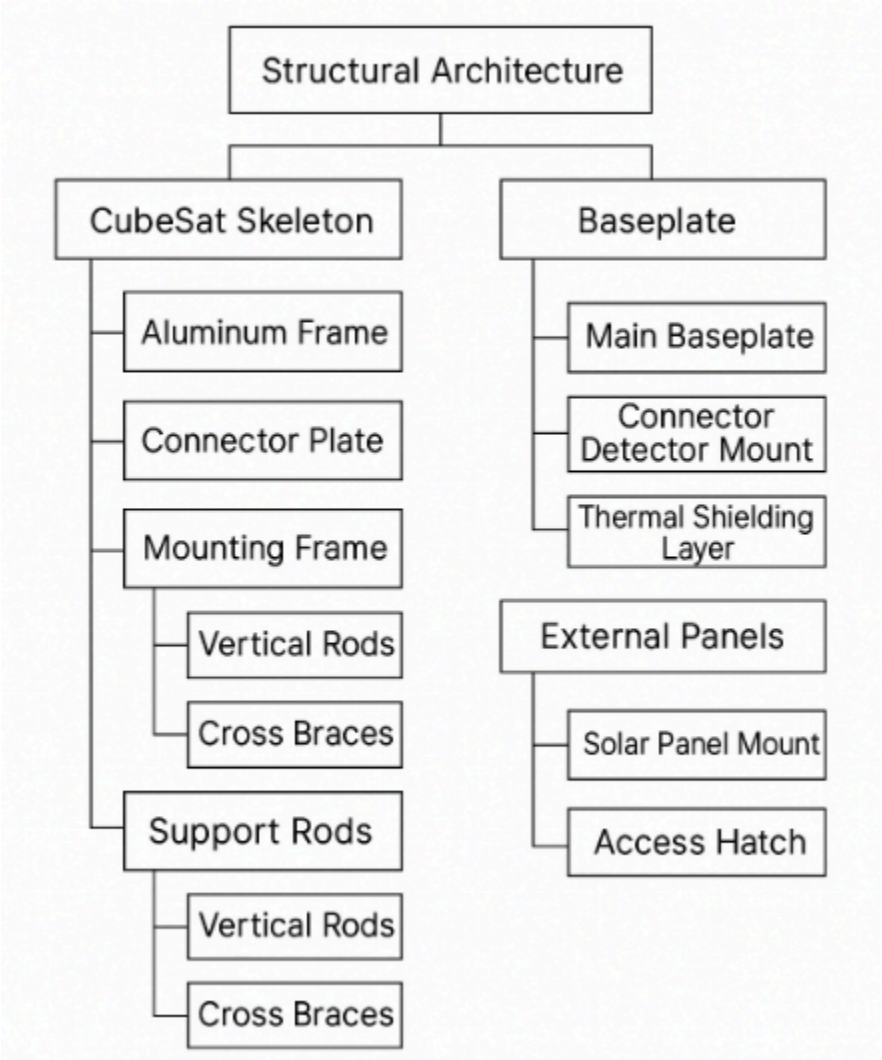


Figure 2.1: ESMD structural architecture

Main structural components:

- **Chassis wall:** The chassis wall forms the outer skeleton of the 1U CubeSat, which will provide both structural rigidity and protection for the internal payload. It is typically made from Aluminum 7075-T6 or 6061-T6; however, in my case, I will be using PLA. This will still offer a high strength-to-weight ratio. The wall includes mounting interfaces for the baseplate, external solar panels, and internal support rods.
    - Purpose: Protects internal components from mechanical stress during launch and provides thermal conduction paths.
    - Features: Precision-machined cutouts for electrical harnesses and payload ports.
    - Dimensions: 10 cm × 10 cm × 10 cm (in a 1U form factor).

- **Baseplate:** The main baseplate will serve as the entire foundation of the 1U CubeSat structure. It connects directly to the chassis rails and provides a flat interface for both the detector housing and electrical subsystem.
    - Purpose: Transfers launch loads between internal components and external deployer rails.
    - Material: Same as the chassis
    - Features: Integrated holes for PCB mounting, thermal sensors, and wiring pass-throughs.
    - Design Considerations: Must withstand compressive loads during deployment.

Table 2.1: Baseplate parameters

Parameter	**Specification**
Material	3D printed PLA
Dimensions	10 cm x 10 cm x 10 cm (1U)
Max Load Capacity	Deployment loads
Mounting Holes	Tapped holes with 2mm screws

- **Connector plate:** The connector plate links the baseplate to the upper skeleton structure and provides attachment points for the radiation detector housing.
    - Purpose: Provides a mechanical and electrical interconnect between structural and payload sections.
    - Features: Contains embedded brass inserts or screw holes for removable payload and extra panel installation
    - Thermal Role: Acts as a heat-sink interface between the detector housing and the CubeSat wall.
    - Fabrication: 3D printed with a resin printer for extra fine measurements

- **Support rods:** Support rods provide axial reinforcement within the CubeSat body, maintaining structural alignment of the internal subsystems such as PCB, power supply, and solar panels.
    - Purpose: Structural stability against vibration and launch acceleration.
    - Material: Carbon-fiber composite or 3D print PLA
    - Configuration: Four rods spaced symmetrically within the frame to connect the baseplate and the top panel.
    - Benefits: Lightweight, easy to disassemble for modular subsystem testing.

2.1.1 CubeSat Skeleton

The CubeSat skeleton serves as the primary load-bearing structure that houses all mechanical and electrical subsystems. The frame adheres to the 1U CubeSat standard dimensions of 10cm × 10cm × 10cm, ensuring compatibility with P-POD or NRCSD deployers. The skeleton includes four corner rails that provide the necessary contact surfaces for launch vehicle deployment and structural rigidity during ascent.

The skeleton will be CNC-machined from aluminum 7075-T6, chosen for its high yield strength and low density, with anodized surfaces to improve emissivity and corrosion resistance. For prototype purposes, a 3D-printed PLA frame may be used to allow low-cost validation of subsystem placement and wiring integration.

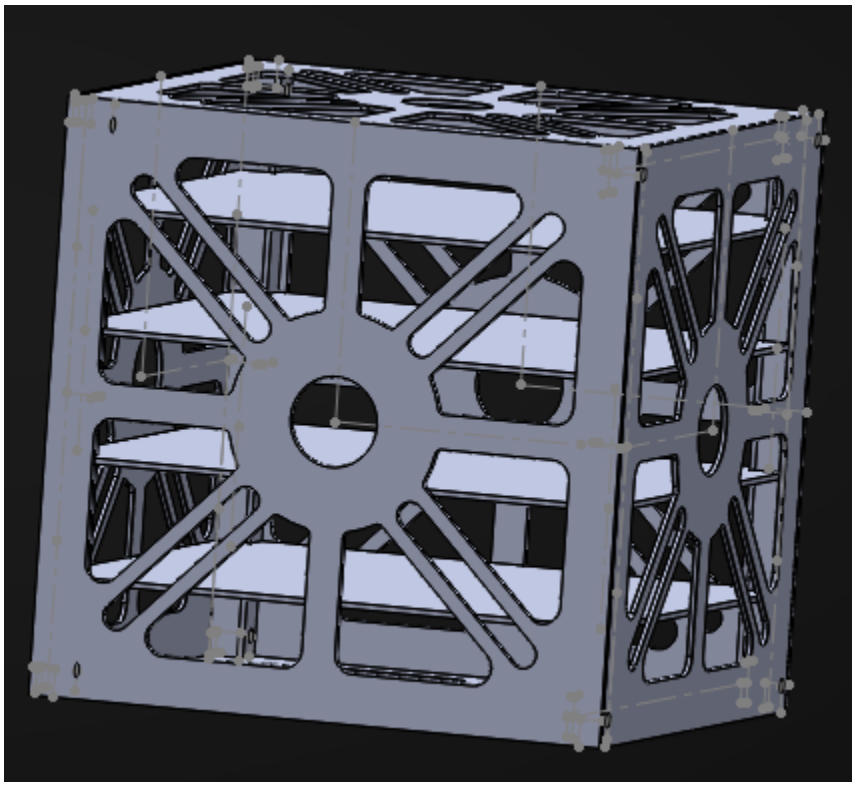


Figure 2.2: CAD design of the ESMD 1U CubeSat

2.1.2 Payload Selection

The payload configuration selected for the ESMD CubeSat was designed to balance scientific functionality with the strict volumetric and mass limits of a 1U CubeSat. The payload consists of a compact combination of power, sensing, and data-processing components required to measure energetic particle radiation in LEO.

The selected subsystems are:

- **Radiation Detector Board** – primary sensor module for collecting radiation counts and dose data.
- **Arduino Microcontroller** – serves as the command and data-handling unit responsible for detector control, data logging, and serial communication.
- **Battery Pack** – rechargeable lithium-ion battery that provides stored power during eclipse and stabilizes voltage fluctuations.
- **Power Management Board (PCB)**– regulates incoming power from the solar panels, controls charging, and distributes voltage to the electronics.
- **Data Acquisition Module (DAQ)** – interfaces with the detector to digitize and store radiation-energy spectra.

These components were chosen for their low mass, open-architecture compatibility, and availability of CubeSat-scale hardware. Table 2.2 summarizes the physical characteristics and mounting locations of each subsystem.

Table 2.2: Subsystem specifications

Subsystem	**Cost ($)**	**Dimension (mm)**	**Mass (g)**	**Location**
Arduino	28.99	88 x 53 x 15	25	Center
Radiation Board	199.99	50 x 50 x 100	40	Adjacent to housing
PCB	34.95	60 x 40 x 100	35	Lower Section
Battery Pack	24.50	60 x 40 x 15	60	Under PCB
DAQ	12.99	50 x 35 x 10	30	Near Radiation Board

Component prices are currently based on the market as of 2025. The payload occupies roughly 35 % of the internal volume, leaving adequate space for wiring channels, thermal control surfaces, and structural fasteners.

The combination of these components allows the CubeSat to operate autonomously while acquiring and storing radiation-spectrum data.

2.1.3 Baseplate and Internal Mounting

The baseplate forms the central structural platform that supports all internal subsystems. It connects directly to the CubeSat rails via four M3 fasteners and provides threaded holes for subsystem mounting brackets. The plate is machined from aluminum 6061-T6, chosen for its balance of strength, machinability, and thermal conductivity. For ground-based testing and educational prototypes, a 3D-printed PLA baseplate may also be used.

Subsystems are mounted on the baseplate in a layered configuration:

- The power and battery modules are placed along the bottom to keep the center of mass near the geometric center.
- The Arduino microcontroller is positioned centrally to minimize cable lengths and electromagnetic interference.
- The detector board and data acquisition module are installed in the upper section, adjacent to the payload housing, to shorten signal paths.
- Four support rods connect the baseplate to the top panel, maintaining structural rigidity under vibration.

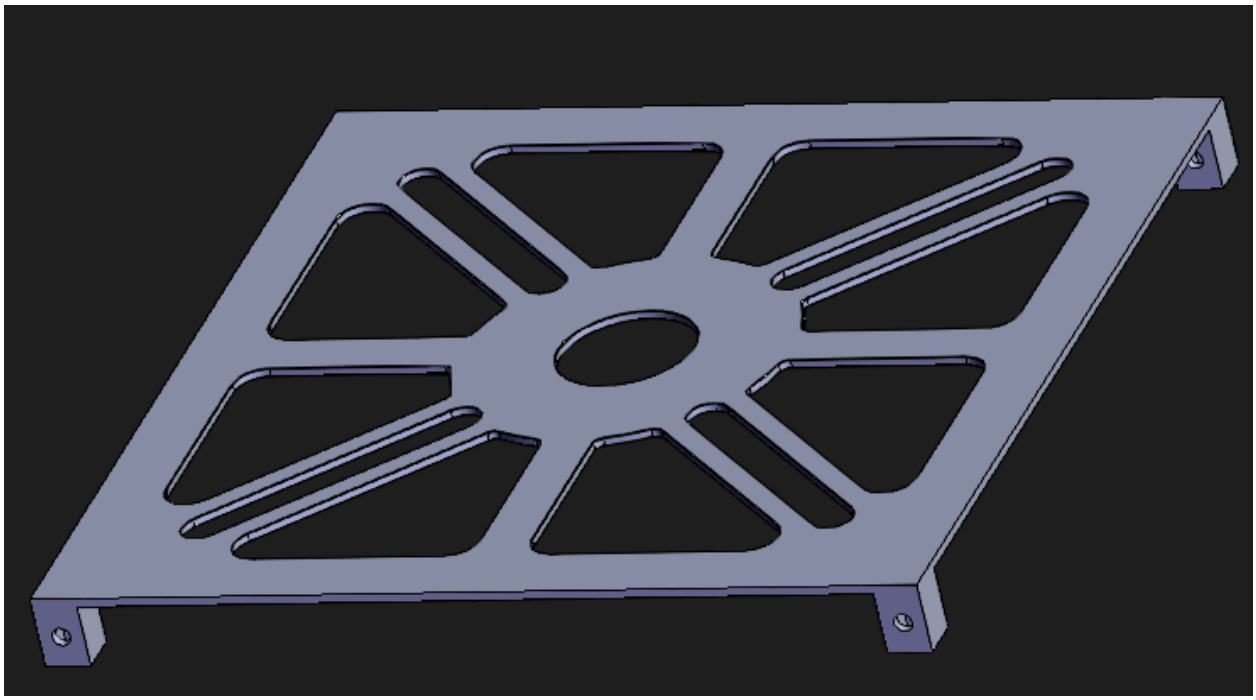


Figure 2.3: Baseplate design

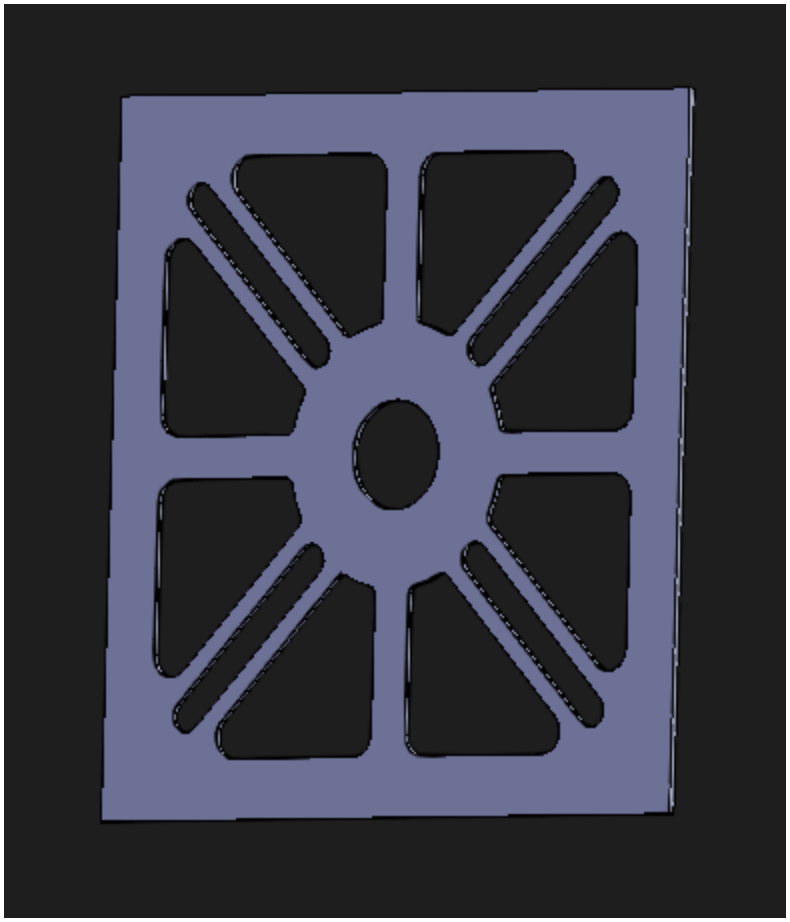


Figure 2.4: Chassis wall

The chassis wall will serve as the primary outer enclosure of the CubeSat. The wall will form the boundary that protects all internal components from mechanical stress and environmental exposure. It is typically constructed from aluminum alloy 7075-T6 because it provides an excellent strength-to-weight ratio and resistance to deformation under launch loads. However, due to budget costs, our 1U cubesat will be a 3D-printed PLA version. Furthermore, each wall panel is 100 mm × 100 mm, which follows the 1U CubeSat standard form factor. The chassis not only provides structural support but also functions as a thermal conduction path, helping dissipate heat from internal electronics to the external surfaces. For ground testing, the 3D-printed PLA version of the chassis wall will be used to validate internal mounting and subsystem alignment before aluminum machining.

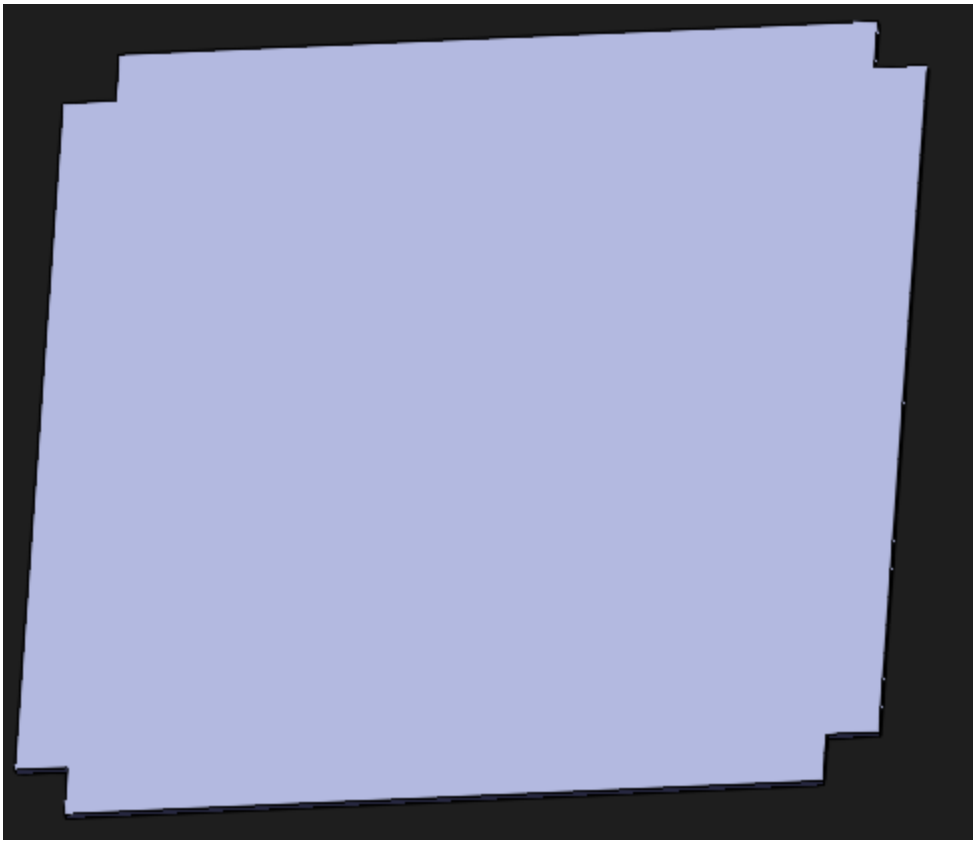


Figure 2.5: Connector plate

The connector plate serves as the mechanical and electrical interface between the baseplate and the upper structural frame of the CubeSat. Its primary function is to provide a stable platform for attaching internal subsystems. These subsystems will include the radiation detector housing, power distribution board, Arduino, and data acquisition systems. The plate has precision-drilled mounting holes and threaded inserts that can allow for secure subsystem attachment while minimizing mechanical vibration transfer during launch. In addition to its structural role, the connector plate acts as a thermal bridge, conducting heat away from electronic components and into the chassis walls. This dual-purpose design simplifies assembly while improving system thermal performance and mechanical reliability.

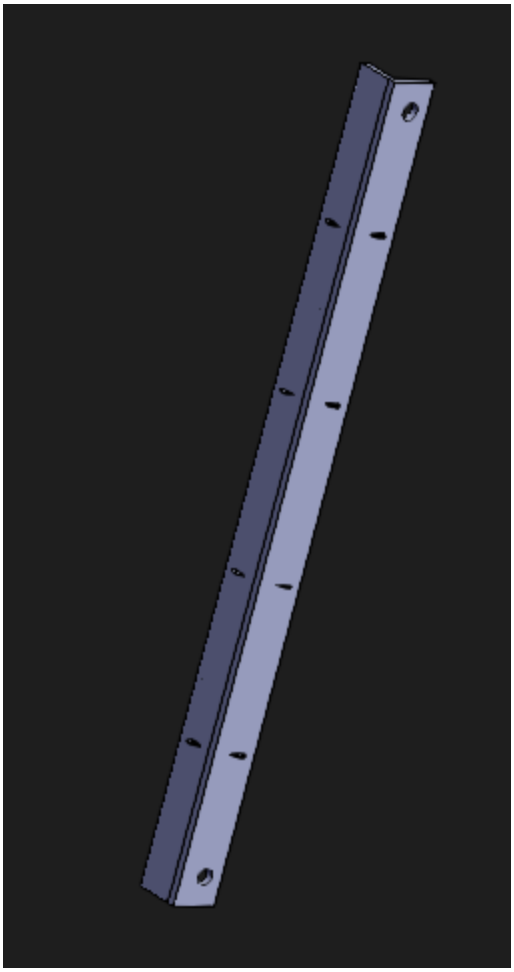


Figure 2.6: Support rod

The support rods provide internal reinforcement within the CubeSat structure, ensuring precise alignment and mechanical stability of the mounted subsystems during vibration and launch loading. Four rods are symmetrically positioned along the vertical corners of the CubeSat, connecting the baseplate, connector plate, and top structural frame. This configuration distributes axial loads evenly and prevents flexing or torsion of the internal assembly. Each rod is fabricated from 3D printed PLA composite to achieve high stiffness with minimal added mass, although aluminum 7075-T6 may also be used for machining in prototype configurations. The rods are secured using M2 fasteners with vibration-damping washers to reduce micro-movements under dynamic conditions. In addition to their structural purpose, the rods also serve as mounting rails for wiring harnesses, providing an organized internal cable management path between electronic subsystems.

2.2 Electrical Architecture

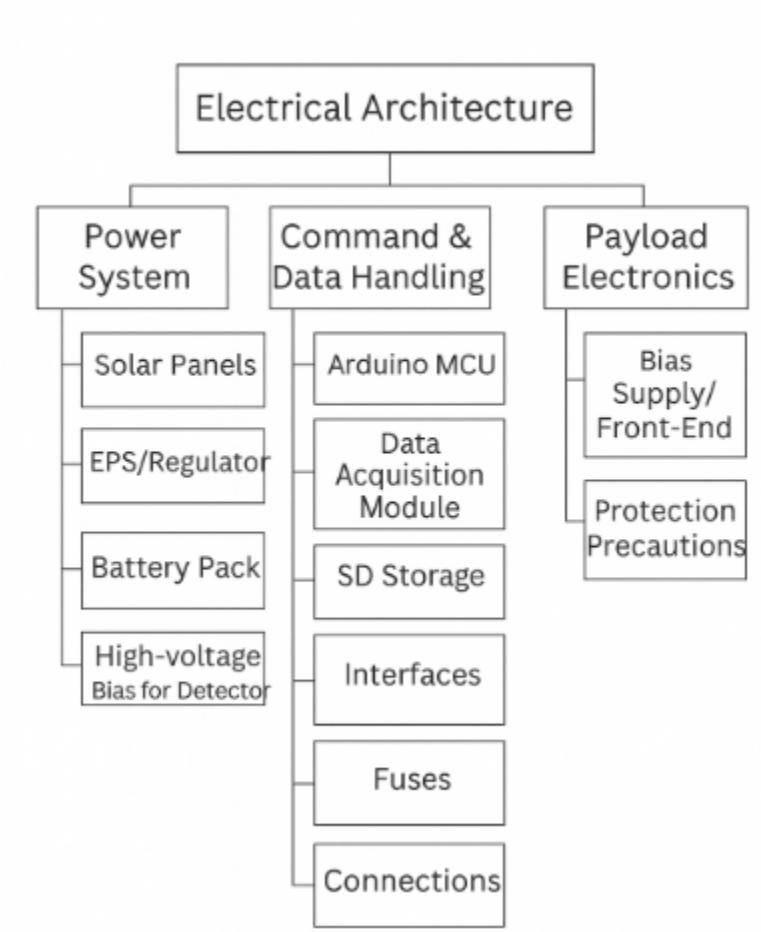


Figure 2.7: Electrical architecture

2.2.1 Arduino Setup

The Arduino microcontroller serves as the central command and data-handling unit for the CubeSat. It governs detector readout, voltage regulation, and data storage. Its lightweight architecture, simple programming interface, and low power consumption make it ideal for 1U-scale missions.

The selected model for this project is the Arduino Mega 2560 Rev3, chosen for its 54 digital I/O pins, 16 analog inputs, and 256 KB of flash memory—enough for detector control and logging operations. The board operates on 5 V and consumes approximately 70 mA during nominal operation.
Alternative microcontrollers, such as the Arduino Nano Every or Due, were considered for size and current draw comparisons, as shown in Table 2.4.

The Arduino receives power from the 5V bus of the EPS and regulates logic signals to 3.3V for sensitive detector interfaces.
Typical connections include:

- SPI Bus → Radiation detector (Timepix or RadFET board)
- I²C Bus → Temperature and voltage sensors
- UART → SD storage module or telemetry port
- Digital Pins D2–D8 → Control and safety interrupts

Table 2.3 Lists nominal voltage and current requirements.

Subsystem	**Voltage (V)**	**Current (A)**	**Description**
Arduino Mega 2560	5	0.07	Main MCU
Detector	3.3	0.12	SPI data communication
SD Storage	3.3	0.02	Logging and data
Sensory Array (I²C)	3.3	0.05	Temp and voltage reader
USB/ Debug port	5	0.10	External power or data upload

Table 2.4: Comparison of microcontroller options

Model	**Clock Speed (MHz)**	**Memory(KB)**	**Voltage (V)**	**Cost (USD)**
Arduino Mega 2560	16	256	5	25
Arduino Nano Every	20	48	5	12
Arduino Due	84	512	3.3	45
STM32 Blue Pill	72	64	3.3	8

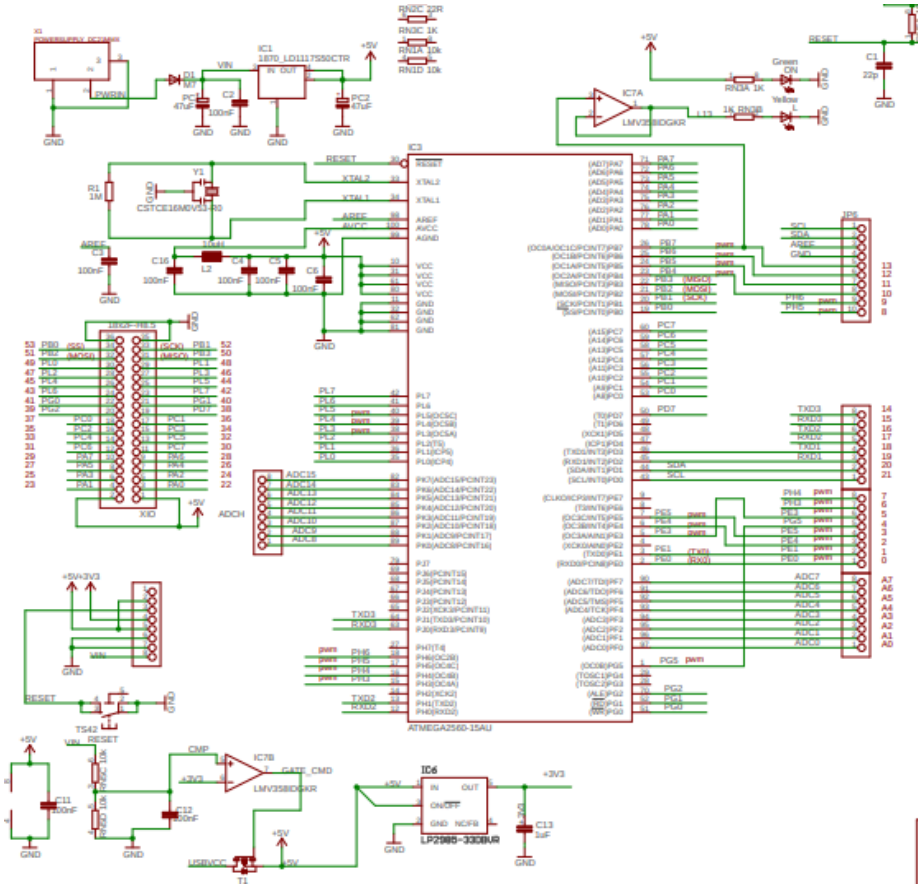


Figure 2.8: Arduino layout

As we can see above, Figure 2.8 illustrates the electrical layout of the Arduino Mega 2560 Rev3. This Arduino board will serve as the central processing unit for the CubeSat's electrical subsystem. The Arduino Mega was selected due to its high pin count (54 digital I/O pins, 16 analog inputs) and reliable 5 V operating logic. This was deemed the most well-suited for integrating multiple sensors, detectors, and communication interfaces within a 1U CubeSat frame. Additional layouts can also be seen in Figure 2.9.

Figure 2.8 shows a labeled diagram of the Arduino Mega, highlighting critical features including the USB interface, voltage regulator, and ATmega2560 microcontroller unit. These features will manage power distribution and serial communication. The source will run between the CubeSat's payload, the data acquisition system, and the external power bus. The USB port enables programming and data transfer. Furthermore, the power jack supports external 7–12 V inputs regulated to a stable 5 V for onboard logic circuits.

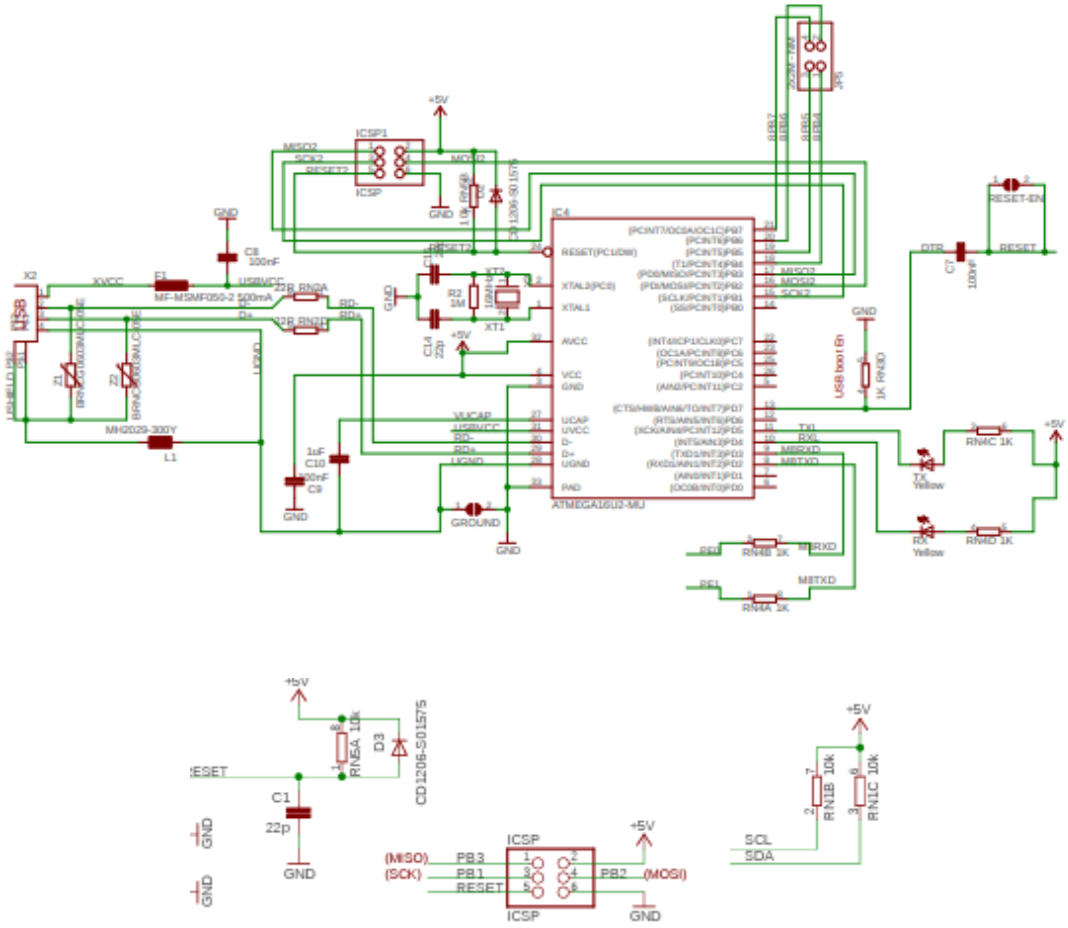


Figure 2.9:Additional arduino circuit layout

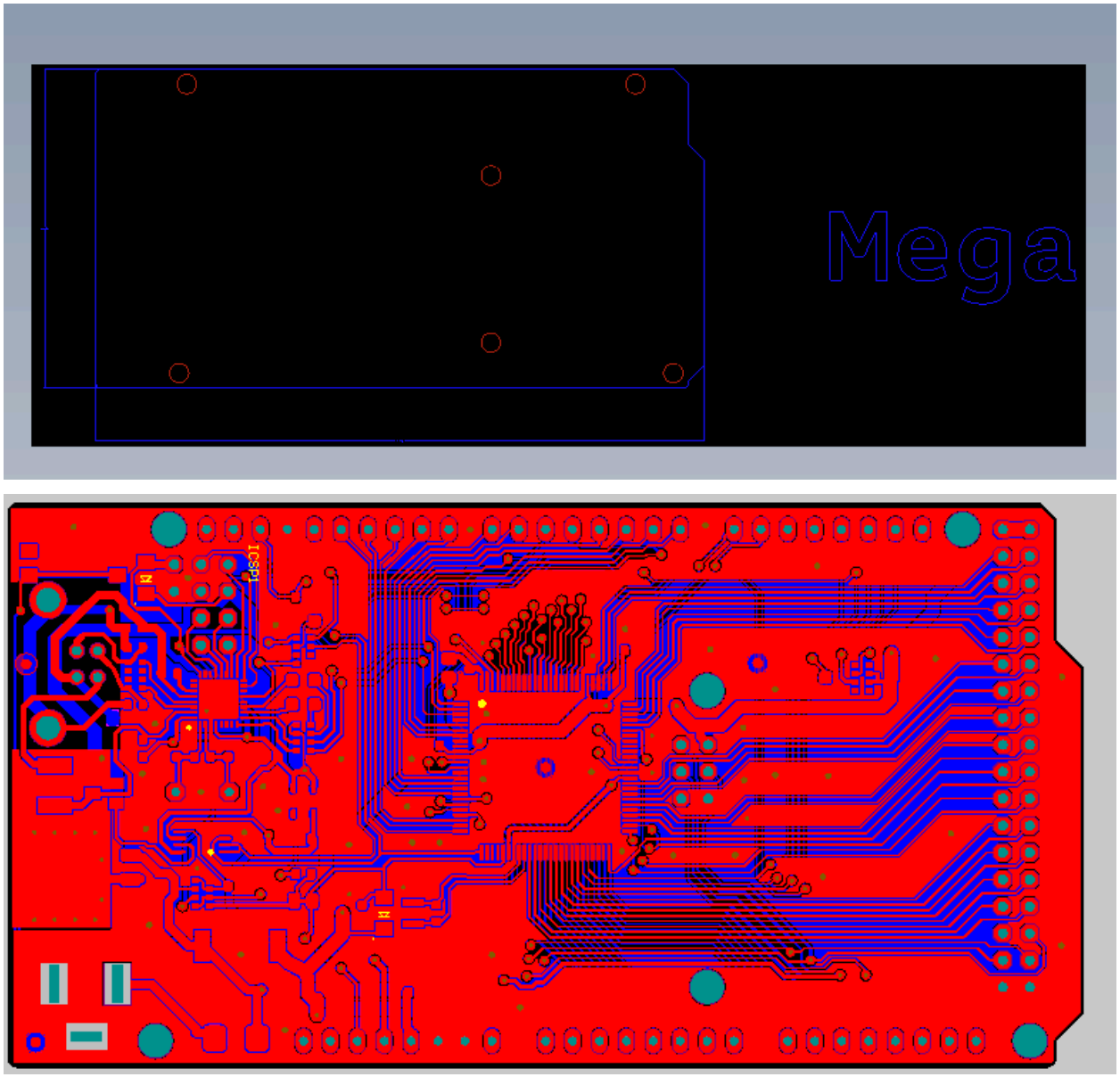


Figure 2.10: Arduino 2560 PCB trace layout

Figure 2.10 presents the Arduino Mega 2560 printed circuit board trace layout. The black plane represents the CAD model of the printed circuit board. In addition, the red copper plane represents the top-layer power and signal traces, while the blue paths indicate the ground and communication routing on the underside. This is key to understanding how the printed circuit board works in an Arduino. This dual-layer routing configuration minimizes electromagnetic interference and ensures low-resistance paths for high-frequency SPI/I²C signals between the detector, data storage, and control interfaces.

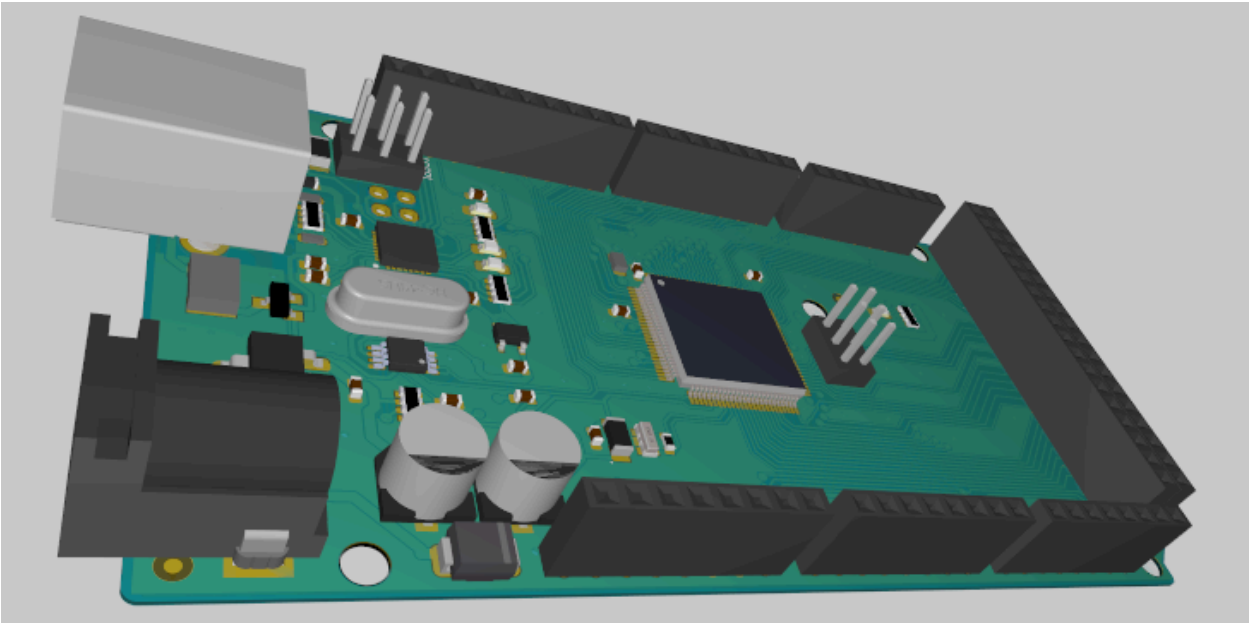


Figure 2.11: Three-dimensional CAD of arduino

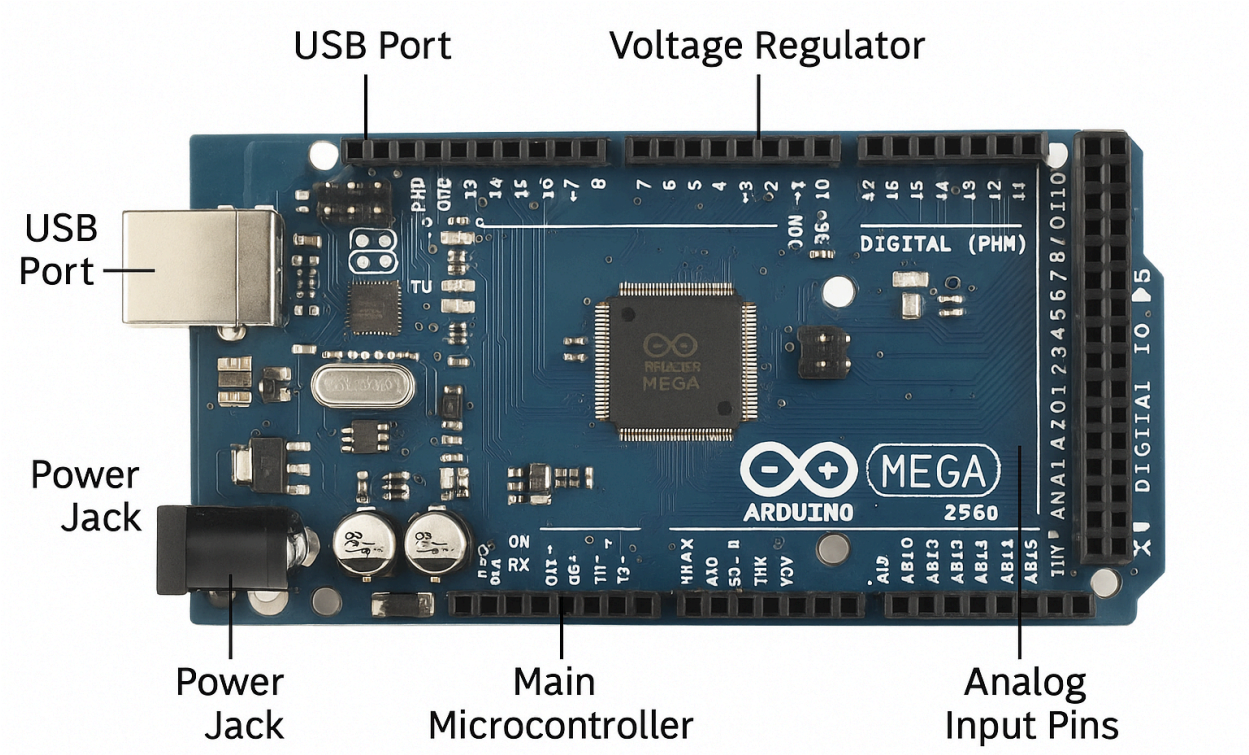


Figure 2.12: Physical three-dimensional arduino

Figure 2.11 provides a three-dimensional visualization of the Arduino's physical configuration, while Figure 2.12 provides a physical three-dimensional model of the Arduino. This model emphasizes the component height distribution, which is crucial for internal CubeSat integration. This is crucial because we need to ensure there is a sufficient amount of spacing between stacked boards. Stacked boards include the PCB, power management module, and data acquisition systems. The three-dimensional CAD view also confirms component accessibility for wiring harnesses and connector headers during assembly.

In the project's prototype phase, the Arduino SA MEGA2560 Rev3e will act as a command and data handling hub. It will manage data acquisition from the radiation detector module, log measurements to SD storage, and interact with the CubeSat's power system through regulated 5 V and 3.3 V buses. This setup offers flexibility for iterative subsystem testing and will later transition to a custom PCB for compact integration within the 1U CubeSat enclosure.

2.2.2 PCB Architecture

The printed circuit board is a key component of the ESMD CubeSat's electrical system. This printed circuit board will act as the central hub that connects all subsystems. These subsystems include the Arduino microcontroller, power management board, battery pack, and radiation detector module.
This printed circuit board simplifies wiring, ensures consistent signal integrity, and reduces potential failure points associated with loose connectors or extended harnesses.

The reason why the PCB is so efficient is because the board layout was designed to handle both power distribution and data communication. This incorporates distinct routing layers for 5 V and 3.3 V power rails, as well as dedicated ground planes for noise isolation.
Signal traces from the Arduino's SPI and I^2C lines are routed directly to the detector and sensor interfaces to minimize electromagnetic interference and timing delays.

Altogether, this PCB integrates:

- Low-dropout voltage regulators for converting a 5 V input to a 3.3 V output
- Bypass and decoupling capacitors are placed near each IC to suppress switching noise.
- Pin headers and JST connectors to simplify component replacement and subsystem testing.
- SMD-mounted fuses and transient voltage suppressors to protect sensitive electronics.

The PCB will be modeled and simulated in LTspice to validate circuit performance and electrical behavior. This test mainly sees if the capacitors and power source align with each other. Furthermore, LTspice simulations confirmed that there was a stable voltage regulation across both buses during peak current draw. The board was then routed as a dual-layer FR-4 substrate with 2 oz copper thickness and ENIG finish for high thermal conductivity and corrosion resistance.

Below will be a generated example of our PCB. This image will illustrate the CubeSat's PCB layout, showing the 5 V and 3.3 V buses, subsystem interconnections, and dedicated grounding planes used to enhance reliability during extended orbital operation.

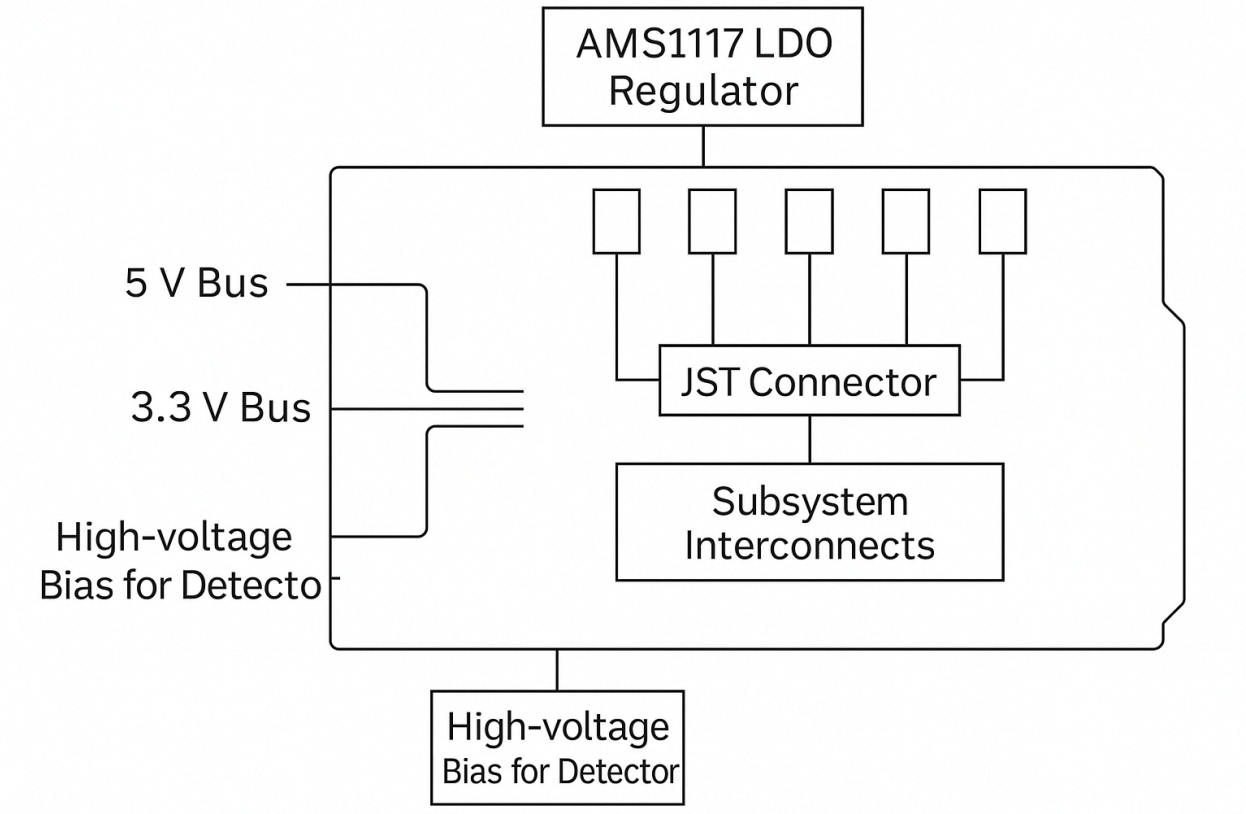


Figure 2.13: Example of printed circuit board

2.2.3 Power Distribution System

The power distribution system provides power to all subsystems of the ESMD CubeSat. These systems include the Arduino microcontroller, radiation detector, data acquisition module, and sensor interfaces. The power distribution system architecture is designed to ensure uninterrupted power delivery during sunlight exposure and eclipse conditions while maintaining system stability and preventing overloads.

The power distribution system will consist of four primary elements:

1. Solar Power Input – The CubeSat utilizes body-mounted solar panels on four exterior faces to generate power during daylight hours in orbit. Each panel provides an average of 2.2 W at 5 V, depending on solar incidence angle and orbital position.

2. Energy Storage Unit – A lithium-ion battery pack (3.7 V, 2200 mAh) stores energy to power the CubeSat during the eclipse phases when solar input is unavailable.

3. Electrical Power System Board – The electrical power system board regulates input voltage from solar cells and manages battery charging through a constant-current/constant-voltage algorithm. It will also provide overvoltage and short-circuit protection.

4. Power Bus Distribution – The regulated output is routed to the subsystems via the PCB, supplying 5 V for logic-level components and 3.3 V for low-power sensors and the radiation detector.

Two key factors contribute to power regulation. We see this through low-dropout regulators and buck converters that ensure stable voltage under transient load changes. Decoupling capacitors and protection diodes placed near key components prevent a number of things, such as voltage dips, reverse current flow, and electromagnetic interference. The 5 V bus powers high-demand subsystems such as the microcontroller and data acquisition board, while the 3.3 V bus is reserved for low-power detector and sensor operations.

Below will be a figure of our power distribution system. This figure will show a simplified schematic of the CubeSat's power distribution system, including solar panel input, EPS control, and subsystem output buses.

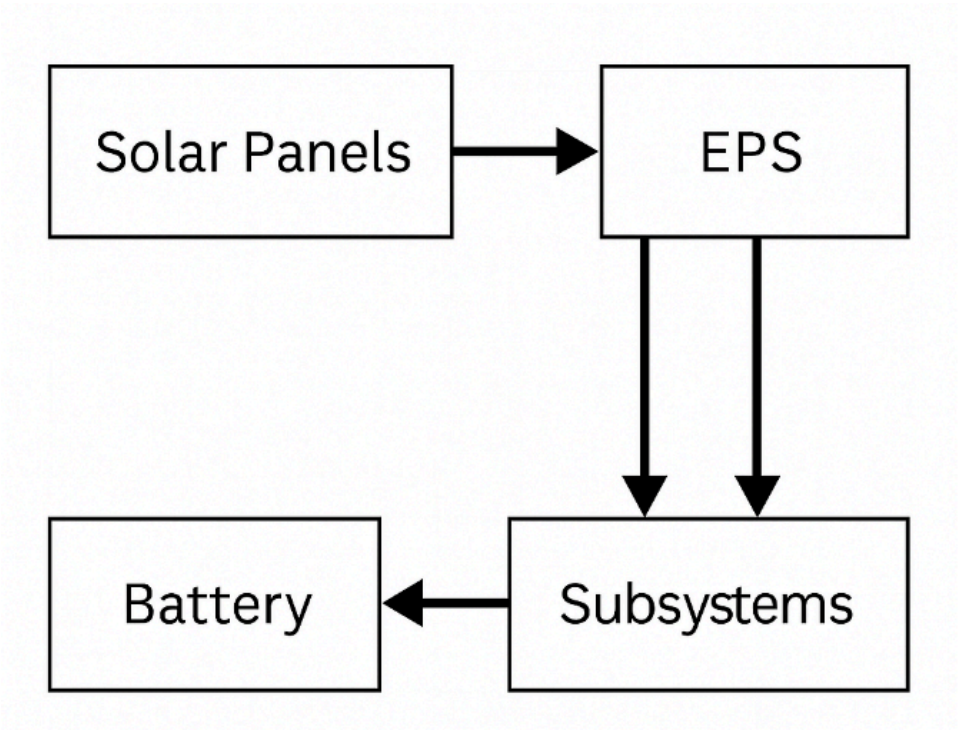


Figure 2.14: Simplified schematic of power distribution

Table 2.4: Estimated power budget

Subsystem	**Voltage (V)**	**Current (A)**	**Power (W)**	**Cycle (%)**	**Average Power (W)**
Arduino	5	0.07	0.35	90	0.32
Radiation Detector	3.3	0.12	0.40	80	0.32
DAQ	3.3	0.02	0.07	30	0.02
Battery Charge	5.0	0.20	1.00	60	0.60
Sensors/Interface	5.0	0.05	0.25	40	0.10
Total Power Consumption	———	———	2.07	———	1.36

From the table, we can see that the total power demand remains below the maximum generation capacity of 8.8 W. Factors that contribute range from the solar array, allowing sufficient margin for battery charging and voltage regulation losses. During an eclipse, the battery pack supplies approximately 1.3 W of sustained power, maintaining system functionality for up to 35 minutes of shadow duration.

To ensure redundancy, the system includes controlled switches that isolate each bus during faults, preventing cascading failures. Additionally, the EPS continuously monitors the voltage of both the solar input and battery output, transmitting health data to the Arduino for logging and power management logic.

This design ensures that the CubeSat maintains electrical autonomy, supporting mission operations without external power intervention and protecting all components under varying orbital conditions.

2.2.4 Data Acquisition and Storage

The data acquisition and storage subsystem mainly focuses on collecting, organizing, and storing data from the radiation detectors and Arduino. This subsystem allows us to have the ability to perform post-mission analysis on data collected in LEO. The data acquisition system will be able to provide timestamped datasets of detector counts, temperature readings, and power voltages.

Data first begins to flow at the radiation detector, which will transmit data through the SPI interface to the Arduino microcontroller. The Arduino will then process and format the data into a structured format created by its user. These structured formats can include data parameters such as dose rate, particle count, time, voltage, and system temperature. This set of data is then written and transmitted to the micro-SD storage module using the built-in SPI communication protocol. Figure 2.15 will provide a visual aid in a flow chart of how the data is being processed.

The micro-SD storage module will have a storage capacity of 16 GB, which is sufficient for operation throughout its orbital pass. Data can be stored in this micro-SD in CSV-formatted logs and can be directly accessed upon payload recovery or even tested in ground simulations. To improve the reliability of the system, a redundant write cycle will be implemented after each data entry. If there were to be a failure or voltage drop detected, the Arduino’s timer will automatically reinitialize the SD to prevent any sort of data corruption.



Figure 2.15: Flow chart of data

2.3 Radiation Detector

Radiation detectors are compact sensing devices. They are designed to measure charged particles, photons, and high-energy radiation fluxes within the spacecraft environment. This is a perfect fit for CubeSats in LEO because CubeSats are continuously exposed to a vast amount of energetic protons, electrons, and trapped radiation within the Van Allen belts. These particles can induce the degradation of electronic components and alter material properties over time. Accurately quantifying these effects can be critical for assessing spacecraft survivability and validating radiation models.

Radiation detectors operate by converting incident radiation energy into an electrical signal that can be processed and interpreted. There are detectors such as semiconductor-based hybrid pixels, cumulative ionization sensors, and scintillators coupled with photodiodes or photomultipliers. To choose the accurate detector, we must take into account a couple of factors, such as mission duration, target energy range, power constraints, and available volume within the payload bay.

For this project, the ESMD employs a RadFET-based radiation detector due to its simplicity, low power consumption, and cost-effectiveness. Unlike pixel detectors, RadFET sensors record total ionizing dose TID accumulated over time. This cumulative measurement approach is ideal for CubeSat-class missions with limited onboard processing and power capacity. Additionally, RadFETs have a well-documented radiation response curve, which gives us a reliable conversion from voltage shift to absorbed dose.

The selected detector system is integrated with the CubeSat’s data acquisition board through an analog interface connected to the Arduino microcontroller. As shown in Table 2.4, several detector options were initially considered before the final selection was mainly made based on cost.

Table 2.5: Comparison of radiation detectors

Detector	Power Used	Mass	Cost	Suitability for Mission
RadFET/PIN	<0.1 W	30g	$199.99	Lower power, low cost
Timepix	~ 2-6 W	50g	$3,000	High power, high cost
Scintilator/SiPM	~ 1 W	80g	$800	High weight, medium cost

Ultimately, the RadFET detector was selected for its balance of low-power operation, proven heritage, and mainly its cost. Its integration with the ESMD system ensures continuous radiation monitoring throughout orbital operations, supporting the mission's goal of validating radiation models and quantifying long-term total ionizing dose in LEO.

2.3.1 Radiation Detector Setup

The radiation detector selected for the ESMD CubeSat is a RadFET read-out board. This board will be equipped with analog outputs, which are suitable for integration with the Arduino microcontroller. This board was procured from Varadis, and its model number is RM-VT01-A. The VT01 provides a buffered analog voltage output corresponding to accumulated dose via RADFET threshold voltage shift. Varadis board supports a single-supply operation and includes an analog interface that can be directly sampled by the Arduino's analog-to-digital converter channels.

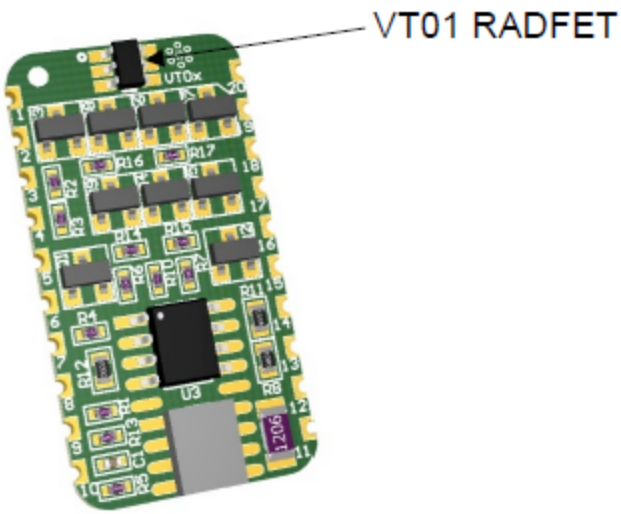


Figure 2.16: Selected radiation board

The cost of the unit falls well within the project budget. While fully space-qualified models can cost a few thousand dollars, the engineering model at the time of purchase was approximately USD $200. Our initial budget is labeled in Table 2.2. This low-cost sensor allows for dose tracking without exceeding the budget constraints of a 1U CubeSat design.

The electrical connection is straightforward and as follows:

- RadFET board is powered by the 3.3 V rail, with ground referenced to the CubeSat common ground.

- The analog output is fed into the Arduino's ADC channels. A decoupling capacitor near the board ensures stable biasing and minimizes noise during orbital operations.

- A digital logic line from the Arduino enables or disables the detector read-out mode via CTRL_EN on the RadFET board. A timer is then started every 10 seconds, which sends data output to our SD storage.

As for the assembly of our radiation board, it will be mounted directly to the internal baseplate of the CubeSat. This is adjacent to the power management board but isolated by standoffs to minimize thermal coupling and mechanical stress. This orientation ensures minimal intervening structural material and maximizes exposure to incident energetic particles while ensuring that the sensor remains inside the deployable internal volume. A thin enclosure provides EMI shielding from the Arduino and power electronics without significantly impeding particle flux.

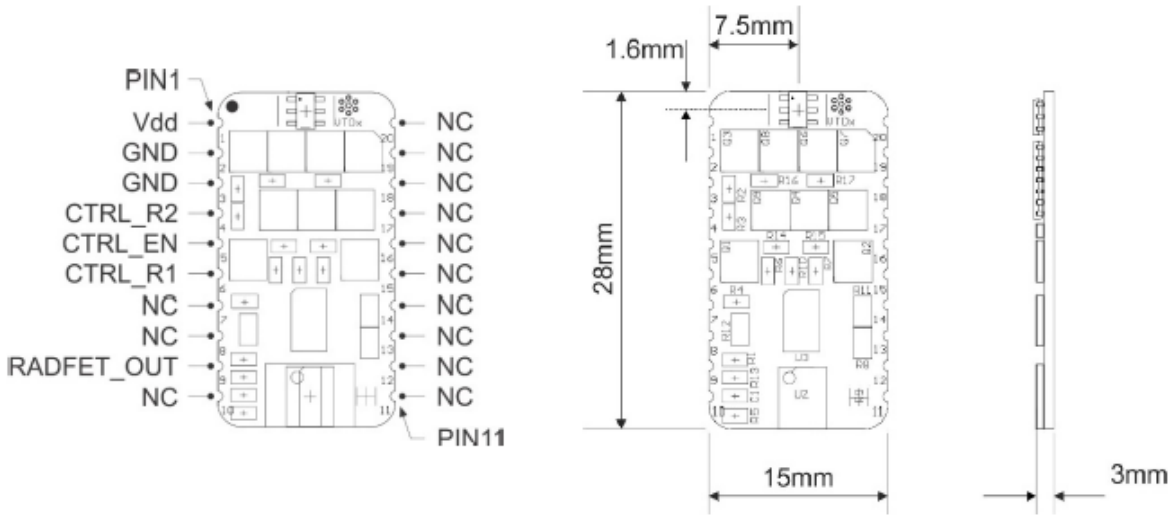


Figure 2.17: Pin configuration of radiation board

The Varadis VT01A radiation dosimeter board measures 28 mm × 15 mm × 3 mm in size, providing a compact and suitable design for integration into our 1U CubeSat. Figure 2.17 illustrates the pinout configuration, which includes dedicated terminals for power input, ground, control signals, and an analog output used for measurement. The RADFET_OUT pin transmits a voltage proportional to the absorbed radiation dose, giving us a direct interface with the CubeSat's Arduino analog-to-digital converter.

This board's small thickness and low power consumption make it an ideal board for integration in direct exposure to the LEO radiation environment. Its low-mass aluminum substrate and minimal component density minimize thermal conduction effects, ensuring accurate dosimetry.

2.3.2 Detector Supply and Regulation

To ensure accuracy in the measurement of radiation to voltage, the VT01A RadFET requires a low-noise, stable voltage. Small variations in supply potential can induce threshold voltage drift in the semiconductor of the RadFET. This can cause a non-linear response. To mitigate this, a dedicated bias and regulation circuit will be implemented within the CubeSat's EPS framework.



Figure 2.18: Bias and regulation flow chart

Figure 2.18 will show the flow chart of the bias and regulation. LTspice can be used to show the conversion and filtering path from the 5 V system to the detector input. The circuit uses a buck-boost converter to maintain a constant 3.3 V output, followed by a regulator to further reduce ripple below 50 mV. A 10 microfarad bypass capacitor is placed in parallel to smooth transient current spikes during sampling.

The regulated 3.3 V line is routed through a precision resistor network that biases the RadFET source terminal while isolating the control lines from analog ground. This ensures that the output signal remains unaffected by small bus fluctuations coming from other subsystems within the CubeSat.

Overall, this regulation scheme provides a ±1% voltage stability margin and ≤10 mW power draw, which is sufficient to support continuous detector operation throughout an orbital period, including eclipse transitions.

3.0 Orbital Trajectory and Radiation Analysis

This chapter establishes the orbital environment and radiation exposure assumptions used to evaluate the ESMD CubeSat. Since the external space environment directly influences particle flux exposure, thermal loading, and long-term mission performance, an understanding of the CubeSat's representative orbital behavior is essential. In the absence of a finalized deployment trajectory for the ESMD CubeSat, a Starling-like LEO is adopted as a reference case. The Starling mission operates within a comparable altitude range and CubeSat mission class, making it an appropriate proxy for estimating orbital characteristics, velocity profiles, and radiation exposure trends relevant to this study.

3.1 ANSYS System Tool Kit Setup

ANSYS System Tool Kit is a very well-known aerospace analysis software for modeling satellites. Analysis can include orbits, mission geometry, and space environment interactions. In this scenario, STK was incorporated to define the spacecraft's orbit, propagate its motion over time, and visualize where it would be over the Earth at a specific time. This capability enables me to evaluate orbital coverage, velocity profiles, eclipse periods, and regional exposure to space radiation.

Orbital propagation within STK is commonly performed by importing Two-Line Element data obtained from publicly available sources such as CelesTrak or Space-Track. These Two-Line Elements describe the spacecraft's orbital parameters at a given epoch and are propagated forward in time using the Simplified General Perturbations Model 4. The SGP4 propagator accounts for many effects, such as perturbative effects in LEO and Earth's atmospheric drag. This is beneficial in our case, as we are operating in LEO.

Once the orbit is defined, STK provides both two-dimensional ground track visualizations and three-dimensional Earth-centered inertial views of the spacecraft trajectory. These visual tools are commonly used to assess orbital inclination, latitude coverage, and altitude variation over the mission duration. In addition, STK supports integration with radiation environment models and external analysis tools to estimate particle flux exposure along the orbit.

Although live orbit propagation was not performed for the ESMD CubeSat within this study due to software licensing constraints, the established STK workflow and methodology remain applicable. The conceptual setup described here ensures that the orbital assumptions and trajectory references used in subsequent analyses are grounded in standard industry practices and validated modeling techniques commonly applied to CubeSat mission design.

3.1.1 CubeSat Expected Trajectory



Figure 3.1: STK starling satellite tracking

For this study, the example given in STK, Starling, was chosen as our trajectory for the ESMD CubeSat mission. Starling operates at an altitude of 300-500km and at a moderate orbital inclination. This is perfect for our case study because Starling's behavior is consistent with the behavior of many CubeSat platforms. If we use Starling's trajectory, this will provide us with a realistic approximation of orbital velocity, ground coverage, and space environment exposure without requiring a mission-specific orbit determination.

In Figure 3.1, we can see a visualization of Starling's path and trajectory. This trajectory was mapped by using a two-dimensional ground track representation on a flat surface of the Earth. This shows us the satellite's motion relative to the Earth's surface over time. The two-dimensional representation is beneficial to our case study because it highlights the latitude coverage and repeated orbital passes characteristic of the ESMD. We can use this projection to track the radiation exposure in regions such as the South Atlantic Anomaly.

Since the ESMD CubeSat does not have a finalized orbit, the use of a Starling-like trajectory gives us a better estimation of what orbital behavior and environmental exposure will look like. This approach is commonly adopted during early mission design phases, where representative or heritage orbits are used to bound expected operational conditions before final launch integration.

3.2 Orbital Mechanics Calculations

Table 3.1: TLE snippet

Time (UTC)	Semi-Major Axis (km)	Vx (km/s)	Vy (km/s)	Vz (km/s)	Eccentricity	Inclination (deg)
1 Oct 2024 20:00:00	6933.19	-4.54	3.77	3.66	0.001419	99.559
1 Oct 2024 20:01:00	6934.16	-4.53	3.76	3.56	0.001446	99.559
1 Oct 2024 20:02:00	6935.49	-4.53	3.75	3.46	0.001518	99.559
1 Oct 2024 20:03:00	6935.41	-4.53	3.74	3.36	0.001519	99.559
1 Oct 2024 20:04:00	6936.40	-4.53	3.73	3.26	0.001530	99.559

Orbital mechanics parameters for the ESMD CubeSat were estimated using publicly available Two-Line Element (TLE) data representative of a Starling-class Low Earth Orbit mission. TLEs prove to be a valuable source of information. TLE's can provide a standardized format for describing satellite orbital elements, including inclination, mean motion, eccentricity, and epoch. In addition, TLE's are widely used in conjunction with numerical propagators such as SGP4.

A set of TLE data can look extremely intimidating. Fortunately, only certain rows are of interest when looking for a particular set of data. For the ESMD, we will be focusing on orbital velocity magnitude as it directly influences aerodynamic drag, atmospheric interaction, and radiation exposure rates. For near-circular LEO orbits, orbital velocity may be approximated as nearly constant over an orbit and dominated by Earth's gravitational field.

To assess velocity variation between successive orbital states, component-wise velocity differences may be expressed as:

$$\Delta V_{x_i} = |V_{x_i} - V_{x_i-1}| \tag{3.1}$$

$$\Delta V_{y_i} = |V_{y_i} - V_{y_i-1}| \tag{3.2}$$

$$\Delta V_{z_i} = |V_{z_i} - V_{z_i-1}| \tag{3.3}$$

Where ΔV_{x_i}, ΔV_{y_i}, ΔV_{z_i} represent the velocity components with respect to the Earth's frame. These variables help quantify changes in velocity between successive time steps, which is useful for identifying variations during the mission from perturbations such as atmospheric drag or gravitational harmonics.

The total velocity magnitude at a given orbital state may then be expressed as:

$$\Delta V_i = \sqrt{V_{x_i}^{\,2} + V_{y_i}^{\,2} + V_{z_i}^{\,2}} \tag{3.4}$$

As mentioned above, the ESMD will follow Starling's trajectory. Calculating for ΔV_i the orbital velocity magnitude is around 7.6–7.8 km/s. This result is consistent with circular orbits at altitudes between approximately 300 km and 500 km. This velocity range is similar to many legacy CubeSat missions and will be used as a representative input for subsequent aerodynamic drag and radiation environment analyses later on.

It is emphasized that these calculations are intended to provide first-order validation and physical context rather than a complete re-propagation of the orbit. The use of TLE-derived velocity magnitudes ensures consistency with real on-orbit behavior while maintaining the scope appropriate for a conceptual mission analysis.

3.3 Radiation and Thermal Environment Analysis

A CubeSat's exposure to radiation in Low Earth Orbit is strongly dependent on factors such as orbital altitude, inclination, and geographic position. As the CubeSat glides and floats through different regions of the Earth's magnetosphere, it is exposed to varying populations of trapped

protons, trapped electrons, galactic cosmic rays, and solar energetic particles. This section establishes the expected radiation environment for the ESMD CubeSat based on a representative Starling-like trajectory and provides a first-order estimate of the particle flux levels relevant to the onboard radiation detector.

3.3.1 Radiation Environment

Using the Starling-like Low Earth Orbit trajectory defined in Section 3.1.1, the radiation environment was assessed qualitatively by examining geographic regions known to exhibit elevated particle fluxes. One of the most important areas is the South Atlantic Anomaly (SAA). This is a region where the inner Van Allen radiation belt approaches closest to the Earth's surface, which results in an increased amount of exposure to trapped protons and electrons. If we take a look at the trajectory of Starling we obtained from the STK study, the selected trajectory repeatedly intersects this region during each orbital period.

In Figure 3.3, the reference trajectory map illustrates global latitude coverage and highlights the ESMD's orbital pass through both equatorial and mid-latitude regions. This trajectory is similar to many CubeSat missions deployed from the International Space Station. While exact radiation levels vary with solar activity and geomagnetic conditions, the projected trajectory provides a relatively accurate estimate for expected environmental conditions and flux particles.

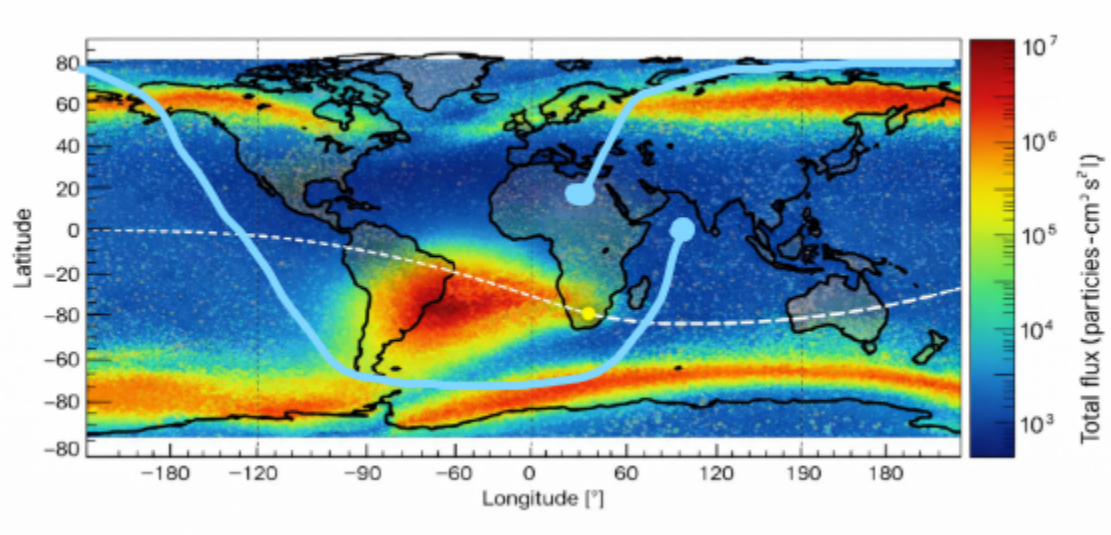


Figure 3.3: Estimated tracking of starling over radiation areas

3.3.2 Expected Radiation Response

Based on the representative orbital altitude and inclination, the dominant radiation contributors for the ESMD CubeSat are expected to be trapped electrons and trapped protons originating from the Earth's radiation belts. For typical LEO altitudes between approximately 300 km and 500 km, trapped electron fluxes on the order of 10^4 to $10^7 particles * cm^{-2} * s^{-1}$ may be encountered, with peak values occurring during SAA crossings. In our case, the path of starling faces ranges from 10^3 to $10^7 particles * cm^{-2} * s^{-1}$, however does an excellent job avoiding most unnecessary radiation paths. This will give us a good range of data that will range from no radiation orbit to huge amounts of radiation.

Using STK and a radiation map with latitude and longitude for analysis and comparisons, electron energies in LEO are commonly concentrated below several MeV, while proton energies in the SAA can extend into the tens to hundreds of MeV range. The overall exposure expected for the ESMD is therefore mainly seen with short, high-intensity encounters rather than continuous uniform radiation.

These estimated flux levels are consistent with previously flown CubeSat radiation missions and provide a meaningful operational range for the ESMD radiation detector. The detector selection and placement described in Chapter 2 were made to ensure sensitivity to these expected particle populations while remaining within power, mass, and cost constraints. The estimated radiation environment presented here serves as the basis for evaluating detector performance and interpreting future measurement data.

4.0 Structural Analysis

The structural integrity of the CubeSat is critical. We must ensure survivability during launch, deployment, and LEO. The current ESMD CubeSat is 3D-printed for prototype purposes. However, its structural layout and component placement must still comply with the CubeSat Design Specification to ensure compatibility with standard deployers and to withstand typical environmental loads such as vibration, shock, and modal changes.

This chapter presents the development of the 1U CubeSat CAD model and the corresponding structural analyses used to evaluate its performance under expected mechanical loads. A complete digital assembly of the CubeSat was constructed in SolidWorks, integrating the chassis, baseplate, payload housing, support rods, and internal electronics. This CAD model serves as the baseline geometry for FEA conducted in ANSYS.

Three primary analyses were performed:

- **Static Load Analysis:** to simulate the deformation and stress conditions experienced during launch.
- **Modal Analysis:** to identify natural frequencies and mode shapes and ensure the structure avoids resonance with the launch vehicle's vibration spectrum.
- **Harmonic Response:** Analysis to evaluate how the CubeSat responds to a sinusoidal load. This test will consist of harmonic lateral directional testing and vertical testing.

These analyses provide a comprehensive understanding of how the ESMD CubeSat behaves under mechanical loading and validate that the prototype design maintains structural stability. The following sections detail the CAD development process, FEA setup, and the results of each structural analysis.

4.1 CubeSat CAD Model Development

The complete 1U CubeSat geometry was designed using SolidWorks. The dimensions of the CubeSat fall within the constraints specification 100 mm × 100 mm × 100 mm. The baseplate, chassis walls, connector plate, and support rods were modeled to match the internal subsystem arrangement described previously in Chapter 2.

All components of the CubeSat will be printed using PLA material properties for physical assembly testing. PLA provides sufficient rigidity for ground-based evaluation at a cost. For real-life scenario analysis, however, the CAD geometry will be assigned Aluminum 7075-T6 material properties. Aluminum 7075-T6 offers a high strength-to-weight performance suitable for launch vibration.

The full structural CAD assembly will be able to integrate all internal subsystems, which include the Arduino microcontroller, power distribution board, battery system, radiation detector, and support hardware. The geometry shown in Figures 2.3–2.6 should be referenced for detailed visualization of each structural element:

- Figure 2.3 – Baseplate design
- Figure 2.4 – Chassis wall
- Figure 2.5 – Connector plate
- Figure 2.6 – Support rod

4.2 Structural Finite Element Analysis

4.2.1 Static Load Analysis

The first structural analysis performed on the ESMD CubeSat will be the Static Load Analysis. In this analysis, I will be mainly focusing on three parts. I will be focusing on the stress pattern, the displacement pattern, and the strain pattern. The weight of the entire structure and the force of seventy newtons will act on the structure. The force of seventy newtons was able to be obtained through the equation below:

$$F = m * n * g \tag{4.1}$$

With the load of 7g axial load, I was able to plug in the numbers and obtain a force of seventy newtons. This 70 N load is applied as a uniformly distributed pressure on the top panel, while the bottom panel is fully constrained to represent the CubeSat being bolted to the deployer rails.

Theoretically, the average normal stress in a region carrying the axial load can be approximated by calculations. The equation we use to approximate the average normal stress in the region is:

$$\sigma = \frac{F}{A} \tag{4.2}$$

where A is the effective load area of the top plate. Next, the elastic response is governed by Hooke's law, which states:

$$\sigma = E * \varepsilon \tag{4.3}$$

where E is the Young's modulus and ε is the normal strain. For the selected material of aluminum 7075-T6, we have a value of 71 GPa for E. The yield strength used in the simulation is $\sigma_y = 5.05 \times 10^8$Pa. These are typical, consistent values with general textbooks and provide the basis for evaluating margins of safety in the FEA results.

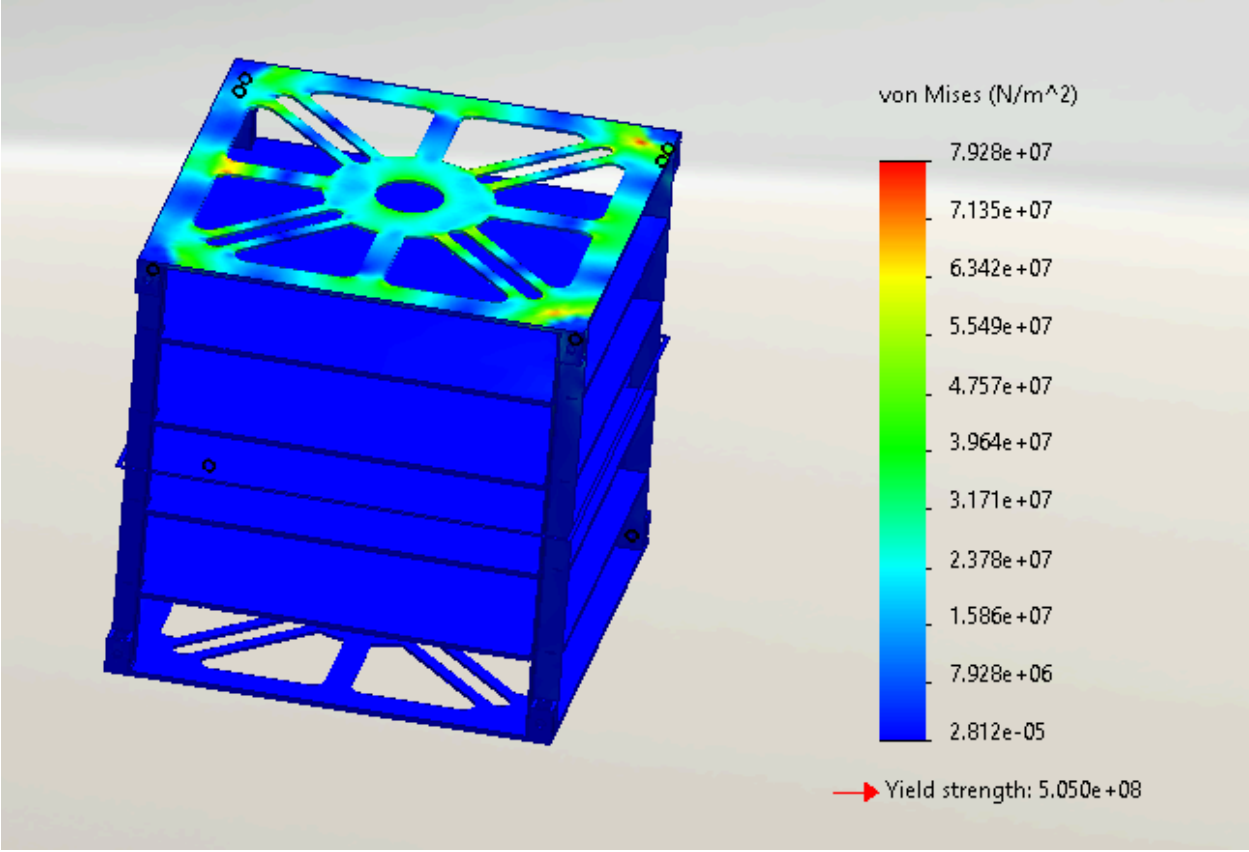


Figure 4.1: Stress pattern contour

The stress pattern contour results for the seventy newtons of force case are shown in Figure 4.1. As we can see, there are peak stresses that occur around the filleted edges and support-rod attachment points of the top panel, where load is transferred into the vertical rails. This is good because we know the seventy newtons of force will be able to spread out around the surface and dissipate. The maximum von Mises stress is approximately 7.9×10^7Pa, which is well below the yield strength of 7075-T,6 which is around 5.05×10^8Pa, meaning our structure will hold its strain. We can then calculate the static factor of safety by using the equation below.

$$FOS = \frac{\sigma_y}{\sigma_{max}} \approx \frac{5.05\times10^8}{7.9\times10^7} \approx 6.4 \quad (4.4)$$

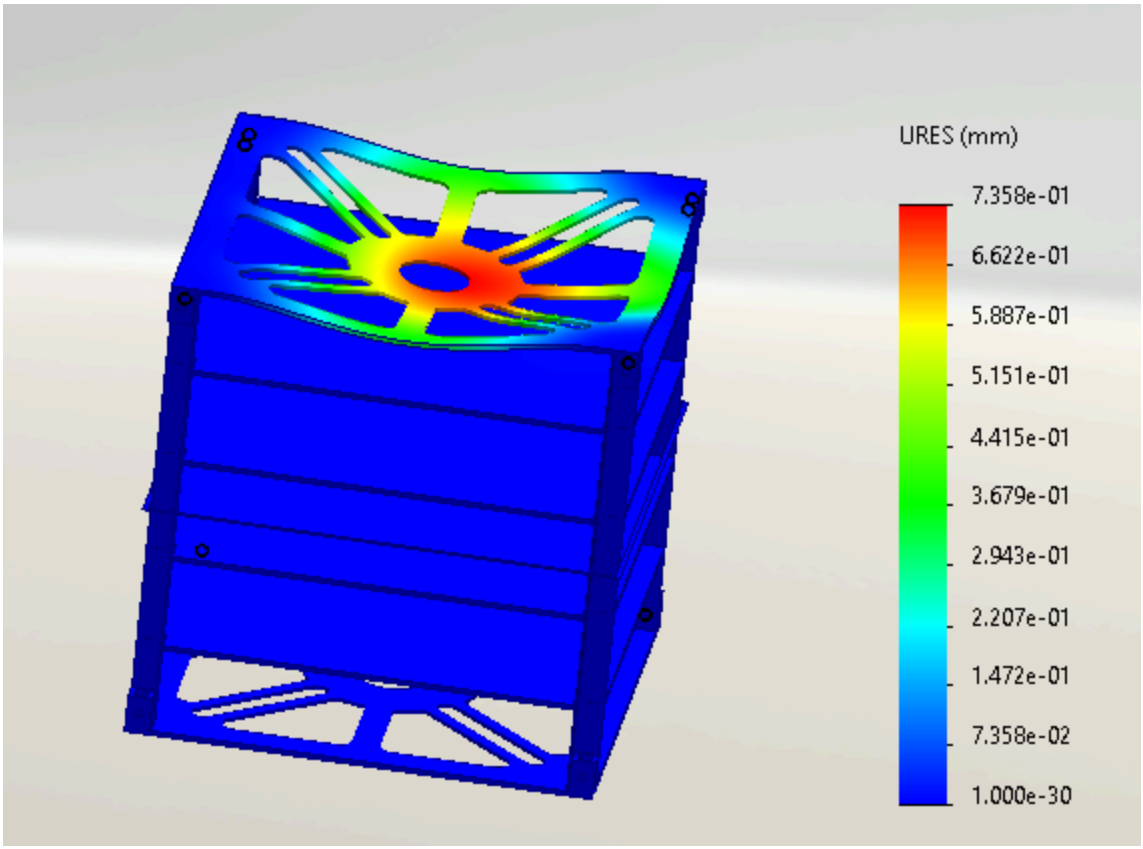


Figure 4.2: Displacement pattern contour

Figure 4.2 presents our displacement pattern contour. The maximum deflection occurs near the center of the top baseplate, where the panel is most flexible. This makes sense as there are no support rods in the middle of the CubeSat, and there are support rods towards the corners. Using the measuring tool on ANSYS and the scale on the right, we can see that the peak displacement u_{max} is approximately 0.74 mm. The middle caves down while the side rails and bottom plate remain nearly rigid. We can consider this deflection to be small compared to the CubeSat and is unlikely to interfere with deployer clearances or internal component alignments.

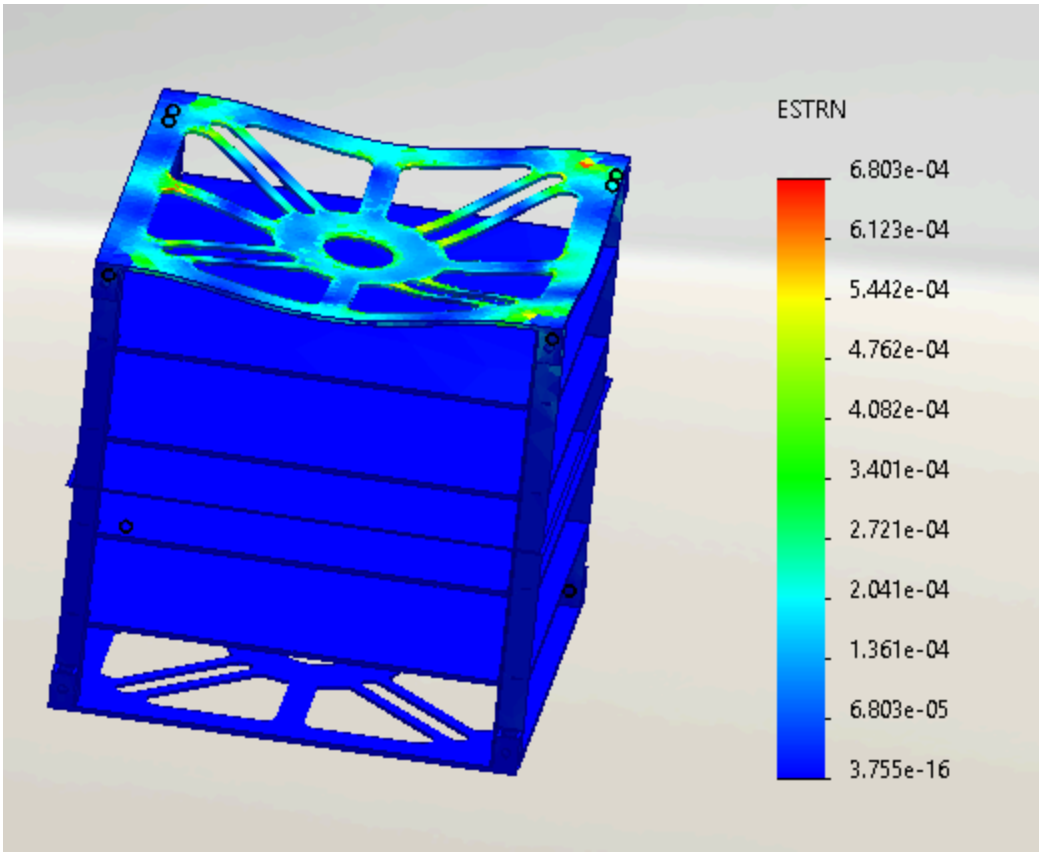


Figure 4.3: Strain pattern contour

The results for the strain pattern contour are shown in Figure 4.3. As we can see, the value of the maximum equivalent strains is 6.8×10^{-4}concentrated at the same high-stress regions along fillets and rail intersections. We can see that there is a slight coupling with the stress and strain patterns, which is expected as there is a relation. Using Hooke's law, these strain values are consistent with the stress levels predicted in Figure 4.1, confirming that the structure remains in the linear elastic regime.

Overall, the static load analysis conducted with FEA demonstrated that the CubeSat can safely withstand an axial launch load of 7g's with more than enough margin against yielding and deflection. These results provide a slight confidence boost that the current structural design is suitable for subsequent dynamic analyses in the future sections.

4.2.2 Modal Natural Frequency Analysis

Modal analysis is the next step in the FEA analysis of the ESMD CubeSat. The primary objective is to determine the natural frequencies and their corresponding mode shapes. This will help describe how the structure deforms when subjected to loads. Every physical structure has an infinite number of natural modes, each with its own frequency and deformation pattern. This is why identifying them is critical for ensuring that the CubeSat does not unintentionally deform during launch and operation.

The relevance of modal analysis for space systems comes from the fact that launch vehicles exhibit strong vibrational environments. There can be vibrational environments within the 20–2000 Hz range. If any of the CubeSat's natural frequencies lie within these high-energy bands, the structure may experience amplified vibration. This can potentially cause loosening, electronic failure, or structural cracking. Fortunately, these issues are avoidable. Industries implement modal analysis to ensure that the fundamental frequency of a CubeSat is well above the operating range to avoid coupling with primary launch loads.

Mathematically, modal analysis solves the generalized eigenvalue problem:

$$(K - \omega^2 M)\phi = 0 \tag{4.5}$$

$$f = \frac{\omega}{w\pi} \tag{4.6}$$

Where:

$K = global\ stiffness$

$M = Global\ mass$

$\omega = natural\ frequency$

$\phi = mode\ shape$

Since the number of possible modal responses is infinite, this study follows the reference CubeSat thesis and extracts the first six modes, which contain the most significant structural behaviors. These lower modes are the most critical for assessing launch survivability.

For each mode, the deformation shape and corresponding natural frequency are recorded. These results provide insight into which parts of the CubeSat are most sensitive to dynamic motion, such as flexing of the top panel, torsion of side walls, or bending of support rods.

Figures 4.4 through 4.9 will show the six computed mode shapes, along with their associated frequencies. Together, these results provide a complete picture of the CubeSat's dynamic response and allow verification that the system meets launch vibration requirements.

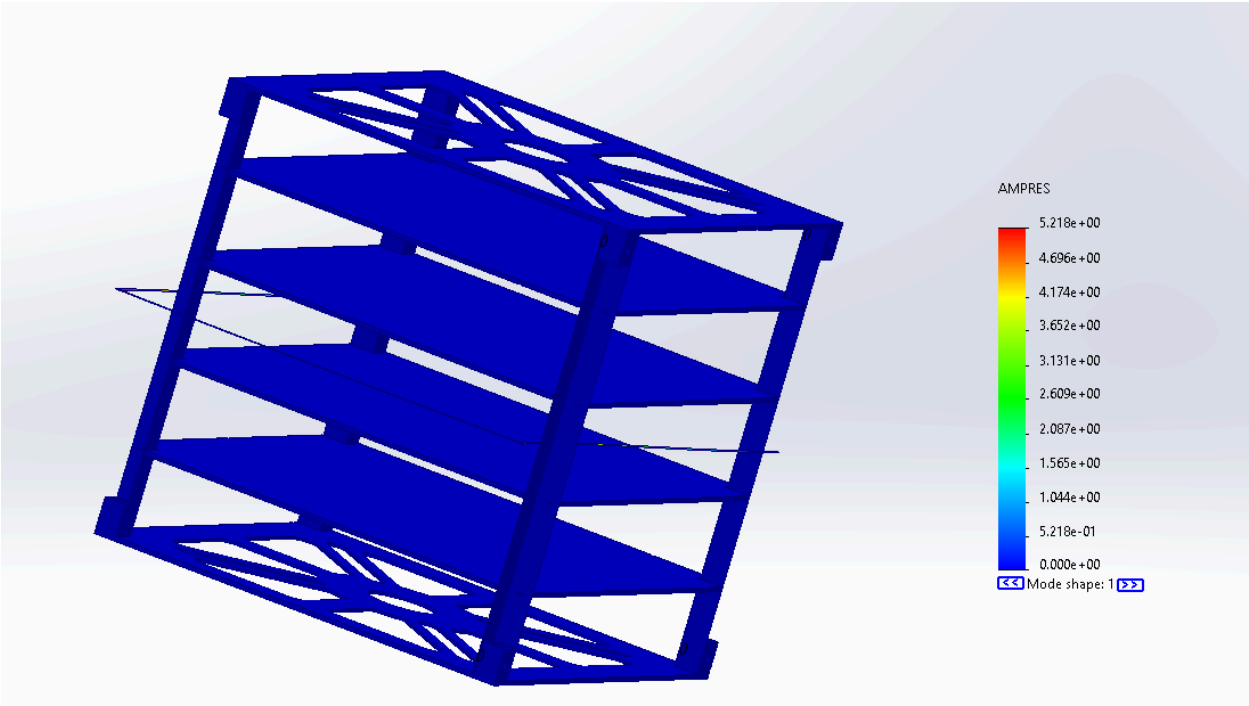


Figure 4.4: First mode shape

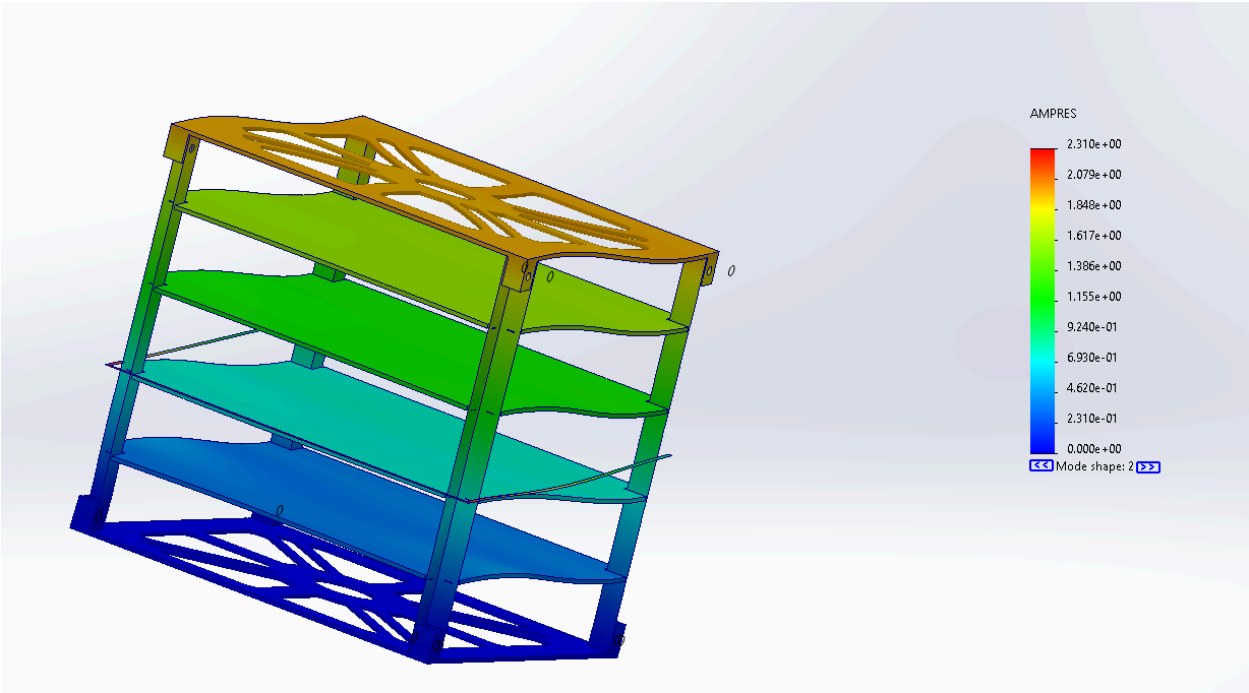


Figure 4.5: Second mode shape

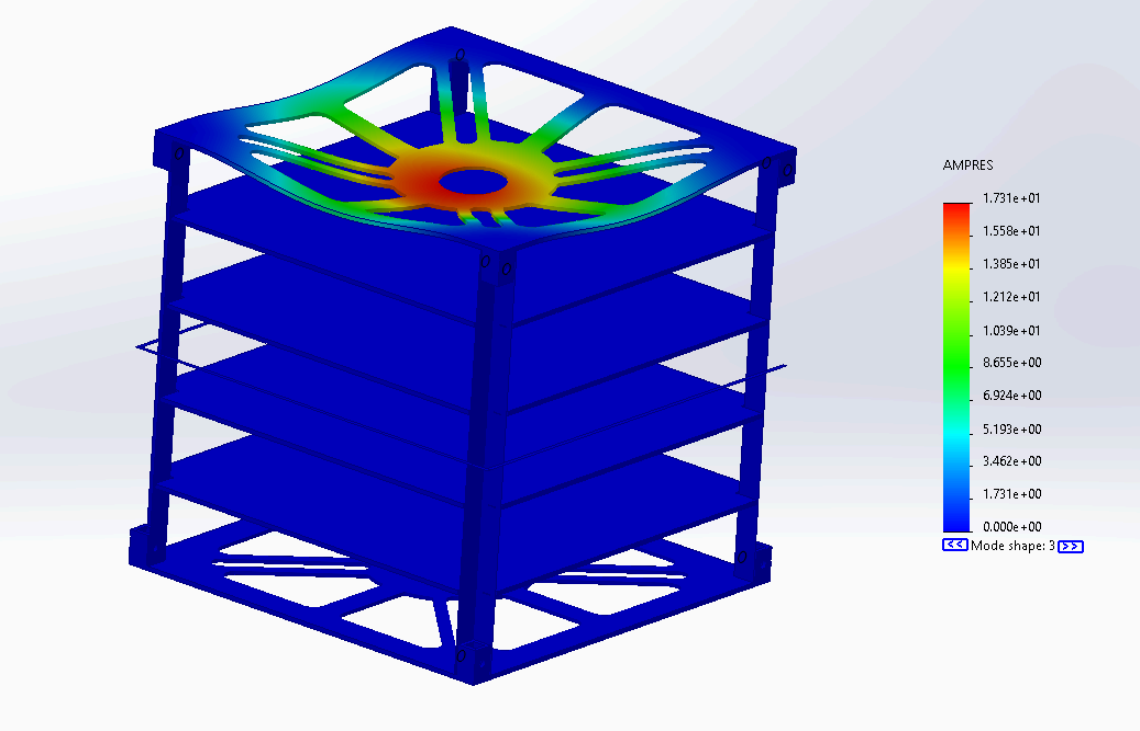


Figure 4.6: Third mode shape

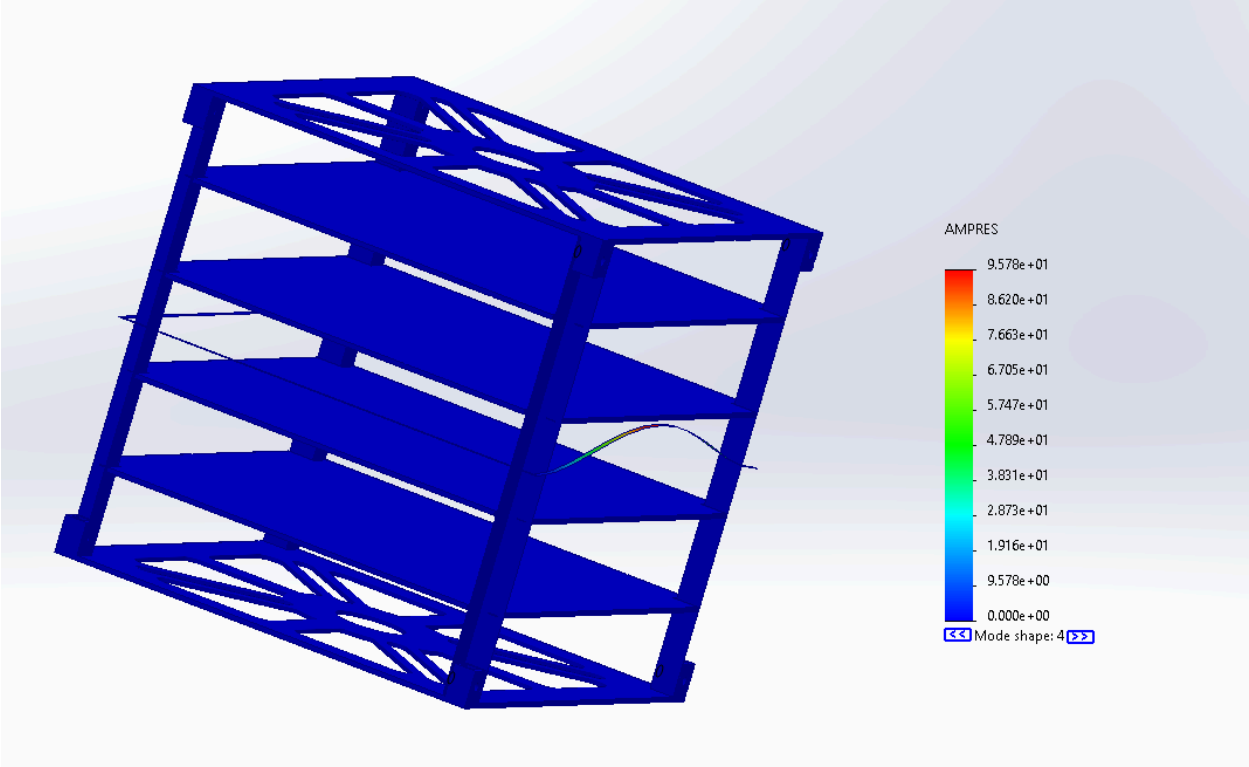


Figure 4.7: Fourth mode shape

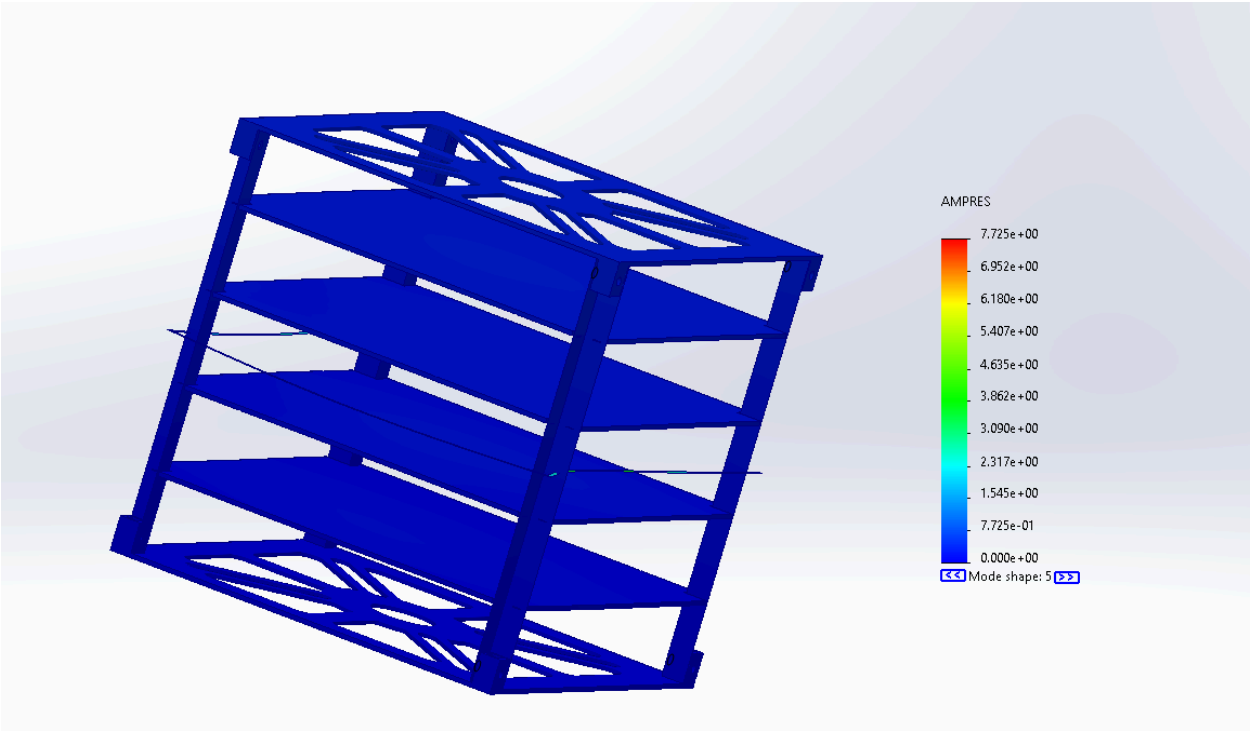


Figure 4.8: Fifth mode shape

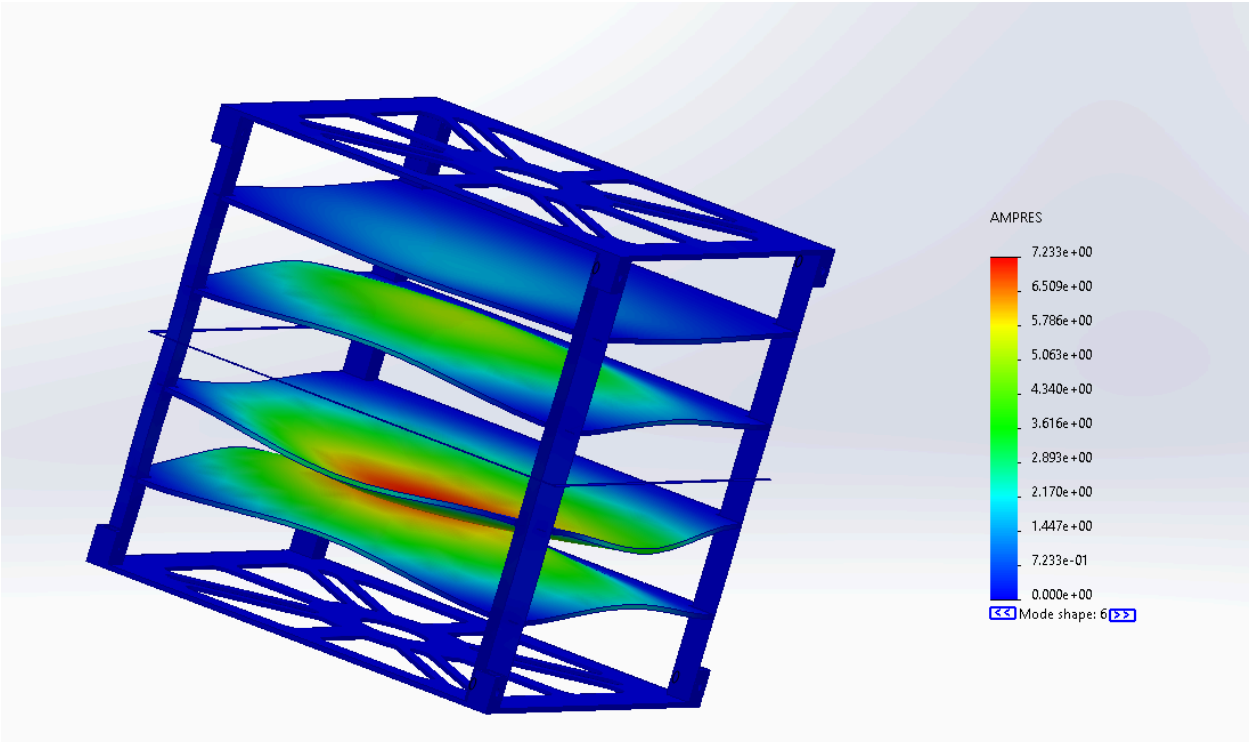


Figure 4.9: Sixth mode shape

Table 4.1: Modal analysis results

Mode	Natural Frequency (Rad/Sec)	Period (ms)	Deformation Character
1	783.45	8.02	Global bending
2	1634.82	3.84	Torsion (twist about the vertical axis)
3	3051.93	2.06	Bending of top panel flexure near top face
4	3469.27	1.82	Side-frame shear
5	4426.82	1.42	Corner-post bending and panel racking
6	4572.40	1.37	Higher-order bending

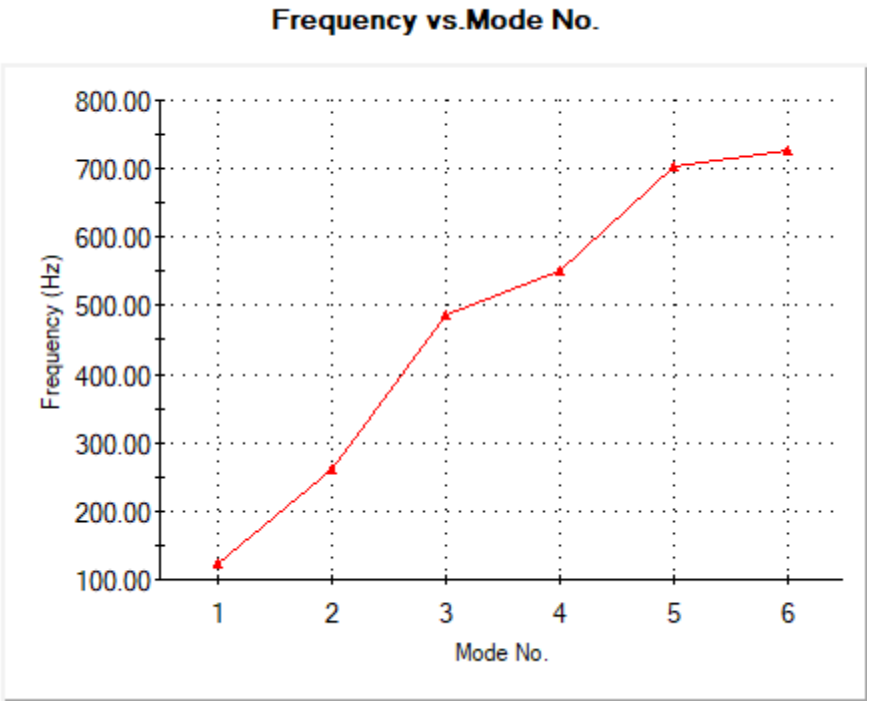


Figure 4.10: Frequency vs mode number graph

A modal analysis was performed to identify the ESMD CubeSat's natural frequencies and corresponding mode shapes. This analysis was performed to see how the structure reacts when there is a force, such as vibration, acting upon the CubeSat. As mentioned earlier, the CubeSat's body is made of Aluminum 7075-T6. Aluminum 7075-T6 has a modulus of elasticity of 71.7 GPa, which is a moderately high stiffness-to-weight ratio, making it suitable for small satellite primary structures.

To maintain consistency and produce results related to the static load case, the modal analysis study used the same boundary conditions as the static analysis. These conditions include the bottom face of the CubeSat being fixed to represent a strap-down to the spaceship during launch. To better observe the behavior and results of the internal payload, the side wall panels were hidden but not removed in the mode shape plots. The primary goal was to clearly interpret the frame/rail bending and torsional behavior that governs global stiffness in the configuration shown.

Six modes were extracted for this study, and the results are summarized in Table 4.1. The plotted shapes in Figures 4.4–4.9 show the deformation pattern associated with each mode.

As we can see, the first mode shows a low-order global bending behavior of the overall structure. This means that this mode will represent the softest change the structure can undergo. Because this is the first case, it is the most critical frequency to track when assessing survivability in a vibration environment. The observed deformation is consistent with a frame-like structure where bending stiffness is governed by the corner posts and rails, while the stiffness is coupled between the top and bottom plates.

The second mode is dominated by torsional motion. This mode represents a twisting motion, which indicates that the structure has a distinct torsional resonance separate from pure bending, which is expected for a symmetric, lightweight frame. Torsion modes are important because they can drive relative motion at mounting interfaces and can excite payload alignment errors if internal hardware is mounted across corners or rails.

Next, in the third mode, we can see a stronger concentration of deformation near the top of the panel. This means that the top of the plate will be flexible, unlike the corner posts and support beams. This is expected and consistent with the geometry: the top plate contains cutouts that reduce bending stiffness, so local flexure can appear at higher modes even when the global frame remains comparatively rigid.

Mode 4 gives us a result that we can interpret as a bending of the side frame motion, where the structure deforms in a skewed manner. In CubeSat-like frames, this behavior is typically governed by how strongly the rails, cross-members, and plate interfaces constrain lateral

distortion. This type of mode is expected in lightweight space frames and can be mitigated by increasing joint stiffness or adding bracing/cross-coupling features.

Moving on, in mode 5, we can see a combined behavior involving the corner posts and frame alignment. Higher modes often couple multiple effects, which can range from a combination of bending, shear, and even local plate flexure. From a design standpoint, seeing this mode at a relatively high frequency indicates that the structure remains globally stiff and only transitions into more complex deformation patterns at higher excitation levels.

The sixth and last mode is another higher-order bending response where deformation becomes more localized and pattern-driven, rather than a simple first-order bending or twist. These higher modes are generally less critical unless a known vibration environment contains strong energy content at those frequencies or if a sensitive component has its own resonance that couples to the structure.

If we take a look at Figure 4.10, we can see a graph showing the mode number vs the frequency. As expected, a monotonic increase in frequency follows along with the mode number. Higher modes typically require higher strain energy, which corresponds to a higher natural frequency. The curve rises rapidly from Mode 1 to Mode 3 and then increases more gradually through Modes 4–6. This behavior suggests the structure's dominant low-frequency compliance is governed by a small number of global motions from bending and torsion. After those are used up, the remaining modes transition into more localized shapes with smaller incremental frequency separation.

If we take into account the requirement for survivability during the mission, the most important result is the first natural frequency at 124.69 Hz. In many small satellite structural design practices, a first mode above roughly ~100 Hz is often considered a favorable indicator of sufficient stiffness for launch vibration environments, which depends on the exact requirements of the launch provider, constraints, and the system's mass distribution. Since this design's first mode exceeds that rule-of-thumb threshold, the structure appears stiff enough to reduce the risk of large resonance amplification at very low frequencies. Additionally, the remaining modes occur at significantly higher frequencies, 260–728 Hz, indicating that the structure transitions quickly into higher-order responses rather than remaining highly compliant.

It is also important to note that modal plots are typically shown with an exaggerated deformation scale for visibility, meaning the displayed deflections do not represent real physical displacement magnitude under a particular force. Modal analysis primarily indicates shape and frequency, and survivability must ultimately be supported by stress/strain checks, which have been completed in Section 4.2.1, and by vibration response analysis if required.

4.3 Discussion of Structural Results

Altogether, the objective of the structural analysis performed on the CubeSat in Chapter four was to validate the structure and whether or not it could withstand launch conditions. We approximated these launch conditions with a static load of approximately 6 g's in SolidWorks. The static analysis evaluated the stress, strain, and displacement of our CubeSat. Under the conditions, the maximum stress placed on our CubeSat was just about $8 \times 10^7 \, Pa$ what remained relatively below the maximum yield strength of aluminum 7075-T6. In terms of the modal analysis, we can see consistent expected behaviors with a stiff lightweight CubeSat frame. Based on the results of the static and modal analysis, we can conclude that the CubeSat will provide adequate strength, stiffness, and dynamic performance for launch conditions. 6 g's did not produce stresses or strains to break the materials' limit, and the natural frequencies were high to avoid critical resonance.

5. Computational Fluid Dynamics

In the previous chapter, we primarily focused on the structural integrity of the ESMD during launch. In this chapter, we will address the external aerodynamic environments that the ESMD CubeSat will face during operation. A series of CFD tests will be used to perform an analysis of the CubeSat and the surrounding rarefied flow. Specifically, we will be looking at the aerodynamic drag, surface pressure distribution, and thermal effects for survivability measures.

The CubeSats will operate in a near-vacuum environment, so atmospheric drag remains a non-negligible perturbation in LEO. Atmospheric drag can be taken into account to directly influence orbital decay, attitude stability, and mission lifetime. Understanding the aerodynamic behavior of the CubeSat is therefore essential for predicting long-term orbital performance and validating the external geometry used throughout this study.

In this chapter, CFD simulations are performed to:

- Estimate the aerodynamic drag force acting on the CubeSat in LEO
- Evaluate surface pressure and flow patterns around the structure.
- Provide first-order estimates of surface heating and wake effects.

The CubeSat assembly developed in SolidWorks is reused for consistency. The CFD analysis will be done using ANSYS Student Fluent 2025. The boundary conditions used for the simulation are under known LEO flow conditions. A brief overview below outlines the numerical setup, boundary conditions, and assumptions employed in the CFD analysis. Lastly, a thorough analysis will be presented, given the results from our aerodynamic and thermal results.

To model the external aerodynamic flow around the CubeSat, the governing equations of fluid motion are considered. The behavior of the surrounding fluid is described by the Navier–Stokes equations, which enforce conservation of mass, momentum, and energy for a viscous flow field.

The continuity equation represents the conservation of mass:

$$\nabla * v = 0 \tag{5.1}$$

which ensures that mass is neither created nor destroyed within the computational domain.

The conservation of momentum is governed by the Navier–Stokes equations:

$$\rho(\frac{\delta v}{\delta t} + v * \nabla v) = -\nabla p + \mu\nabla^2 v \tag{5.2}$$

where ρ is the fluid density, v is the velocity vector, p is the pressure, and μ is the dynamic viscosity. These equations capture the effects of inertial forces, pressure gradients, and viscous stresses as the flow interacts with the CubeSat geometry.

To account for turbulence effects in the external flow, the RANS formulation is employed. In this approach, the instantaneous velocity field is decomposed into mean and fluctuating components, introducing additional Reynolds stresses that must be modeled.

The k–ε turbulence model was selected in the ANSYS solver to close the RANS equations. This model introduces two additional transport equations. There is one for the turbulent kinetic energy and one for the turbulent dissipation rate. The t equation is expressed as:

$$\frac{\delta(\rho k)}{\delta t} + \nabla * (\rho k v) = P_k + \rho\varepsilon + \nabla * [(\mu + \frac{\mu_t}{\sigma_k})\nabla k] \quad (5.3)$$

and the dissipation rate equation is given by:

$$\frac{\delta(\rho\varepsilon)}{\delta t} + \nabla * (\rho\varepsilon v) = C_{1\varepsilon}\frac{\varepsilon}{k}P_k - C_{2\varepsilon}\rho\frac{\varepsilon^2}{k} + \nabla * [(\mu + \frac{\mu_t}{\sigma_k})\nabla\varepsilon] \quad (5.4)$$

where P_k represents the production of turbulent kinetic energy and μ_t is the turbulent eddy viscosity.

These governing equations are solved numerically within the defined fluid domain to obtain velocity, pressure, and turbulence fields around the CubeSat. The resulting flow solution enables estimation of aerodynamic drag forces, surface pressure distributions, and wake behavior under representative LEO conditions. While higher-fidelity rarefied flow models are required for detailed LEO analysis, this formulation provides a reasonable first-order aerodynamic assessment suitable for preliminary design validation.

5.1 CFD Setup

5.1.1 Geometry and Meshing

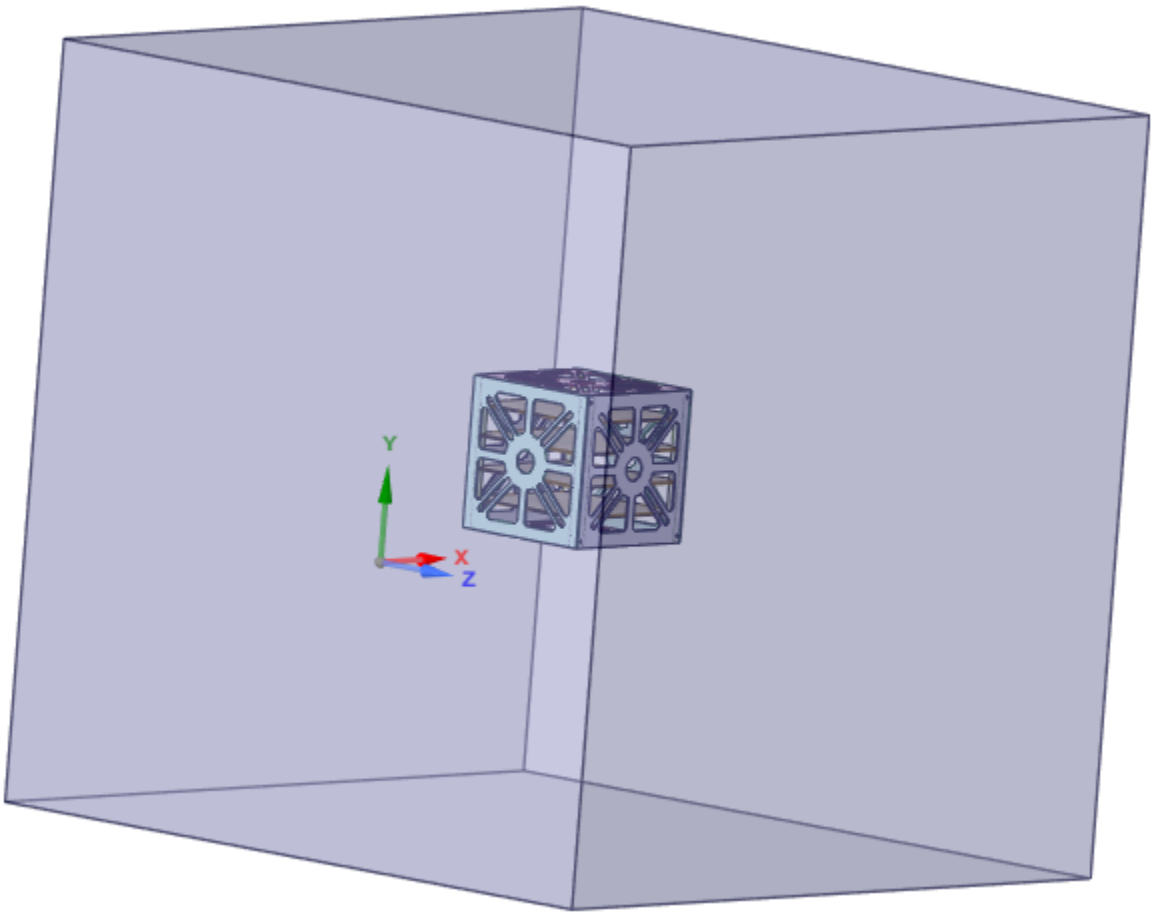


Figure 5.1: CubeSat in boundary condition box

As mentioned earlier, the geometry modeled in SolidWorks was transported as a STEP file and reused in ANSYS for the CFD analysis. In order to model the external flow, a three-dimensional fluid domain was constructed around the CubeSat, as shown in Figure 5.1. To complete this task, an enclosure operation was performed. The CubeSat was positioned directly in the center of the domain to minimize boundary interference. To allow sufficient space for flow, I made sure the enclosure was at least 3-4 times the CubeSat size.

The CubeSat walls were treated as a solid body with no-slip walls. As mentioned above, the enclosure represents the freestream environment and provides a decent amount of accuracy for the flow solver. In addition, a Boolean subtraction function was used so that the solver can handle the interactions between the solid and fluid regions directly.

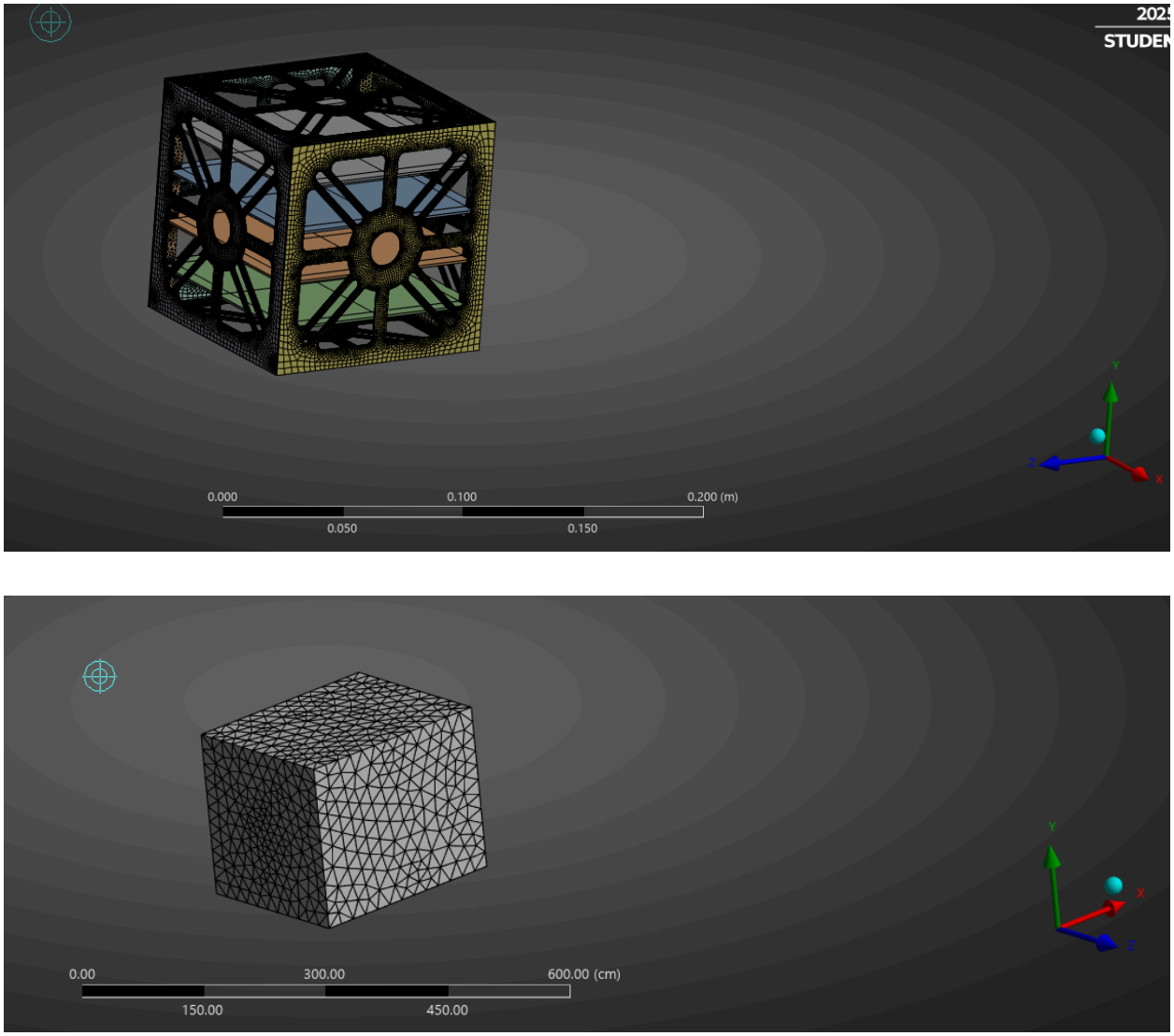


Figure 5.2: Mesh generated

The following mesh was generated using ANSYS Workbench and its meshing tool. To create the mesh, I took the completed assembly and the enclosed box into ANSYS's meshing tool. A quick generation gave a fairly solid topology of the mesh, and a few sizings were needed to adjust the cell size. The cells were reduced to 1 cm due to ANSYS Fluent Student having a maximum cell count. Lastly, the inlet, outlet, walls, body, and fluid sections were created so we can begin the simulation flow in the next step.

5.1.2 Boundary Conditions and Flow Conditions

The CubeSat’s conditions were mottled under LEO, where atompsoheric drag remains non-negligible. To capture this behavior, the simulation's boundary and flow conditions need to match LEO conditions. A few representative orbital altitudes are presented to us when talking about LEO. Table 5.1 provides a quick summary of the estimates. These conditions were placed where CFD provides qualitative trends. The condition of 400 km and 7.67 km/s was chosen.

Table 5.1: Representation of different conditions

Altitude	**Velocity**	**Regime**
300 km	7.73 km/s	Rarefield
400 km	7.67 km/s	Rarefield
500 km	7.61 km/s	Transitional

The inlet boundary was selected as a uniform velocity, which aligns with the CubeSat's body axis, representing the motion of the satellite as it goes through the atmosphere. The freestream velocity was set according to the altitude of 400 km as well as the density. The outlet was modeled as a pressure outlet, allowing flow to convect out of the domain.

Additionally, the surface of the cubesat was set to a no-slip wall, enforcing zero velocity at the solid boundary. A pressure-based solver was implemented, and gravity was applied to the y-axis, as we are still in LEO. Turbulence effects were modeled using the k-ε turbulent model. This model was selected for its robustness and consistency with external flows.

5.2 Aerodynamic Drag Results

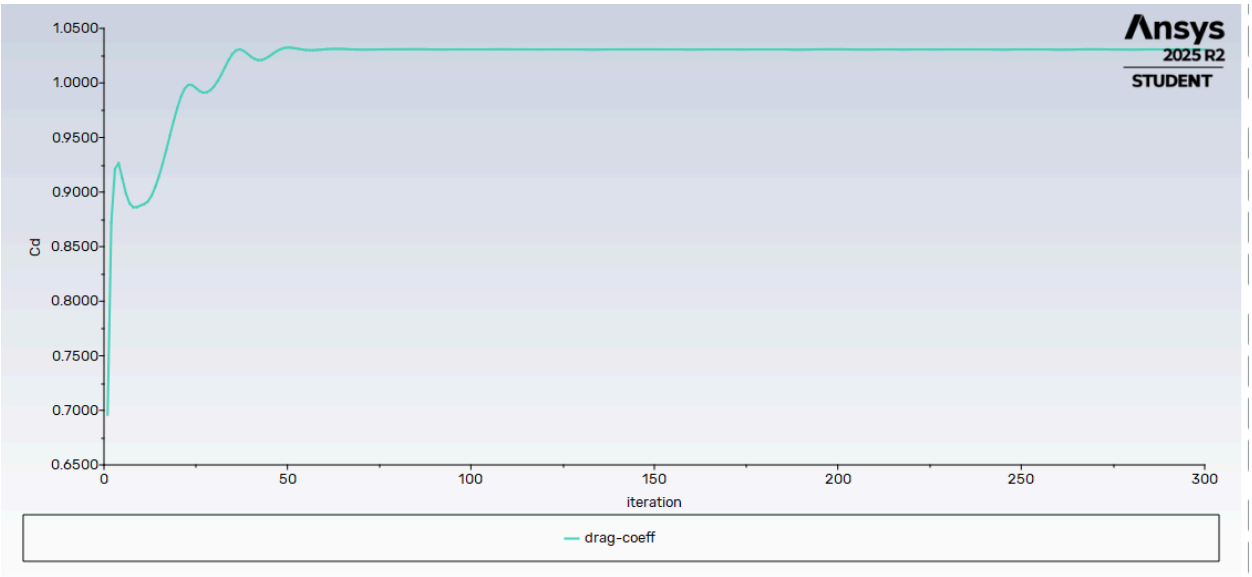
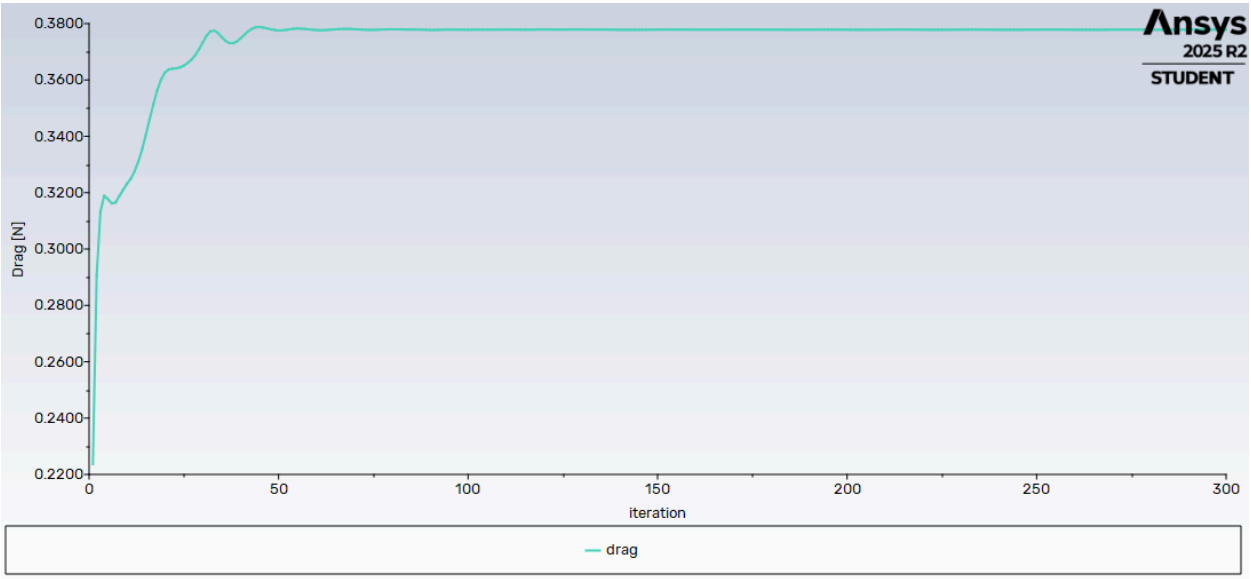


Figure 5.3: Drag coefficient results



298	1.9576e-03	1.5222e-07	7.3982e-08	6.7177e-08	6.3669e-04	1.1756e-05	1.0404e+00	3.7783e-01	0:00:00	2
299	1.9395e-03	1.4889e-07	7.2788e-08	6.7227e-08	6.3897e-04	1.1769e-05	1.0404e+00	3.7782e-01	0:00:00	1
300	1.8858e-03	1.4588e-07	7.1658e-08	6.7143e-08	6.3644e-04	1.1838e-05	1.0404e+00	3.7781e-01	0:00:00	0

Figure 5.4: Drag force results

The aerodynamic drag behavior of the CubeSat was evaluated in LEO flow conditions using the CFD setup described in Section 5.1. Figure 5.3 presents the convergence history of the drag coefficient and total drag force over the course of the simulation iterations. An initial transient response is observed during the early iterations as the flow field develops around the body, followed by a smooth approach toward a steady value. After 50 iterations, the drag coefficient and the drag force both converge. This is fairly quick, which indicates that a steady-state solution has been achieved.

The converged drag coefficient is consistent with expectations for a bluff-body geometry such as a cube aligned normal to the flow direction. The drag force reaches a stable peak at around .37, which ultimately reflects the balance between the freestream velocity, atmospheric density, LEO altitude, and the projected area of the CubeSat. These results confirm that the solver setup and turbulence model selection produce physically reasonable aerodynamic predictions. While the rarefied nature of the upper atmosphere limits the fidelity of continuum-based CFD methods, the obtained drag trends provide a first-order estimate suitable for comparative analysis, mission planning, and validation of the CubeSat's external geometry under nominal orbital conditions.

5.3 Visualization Contours

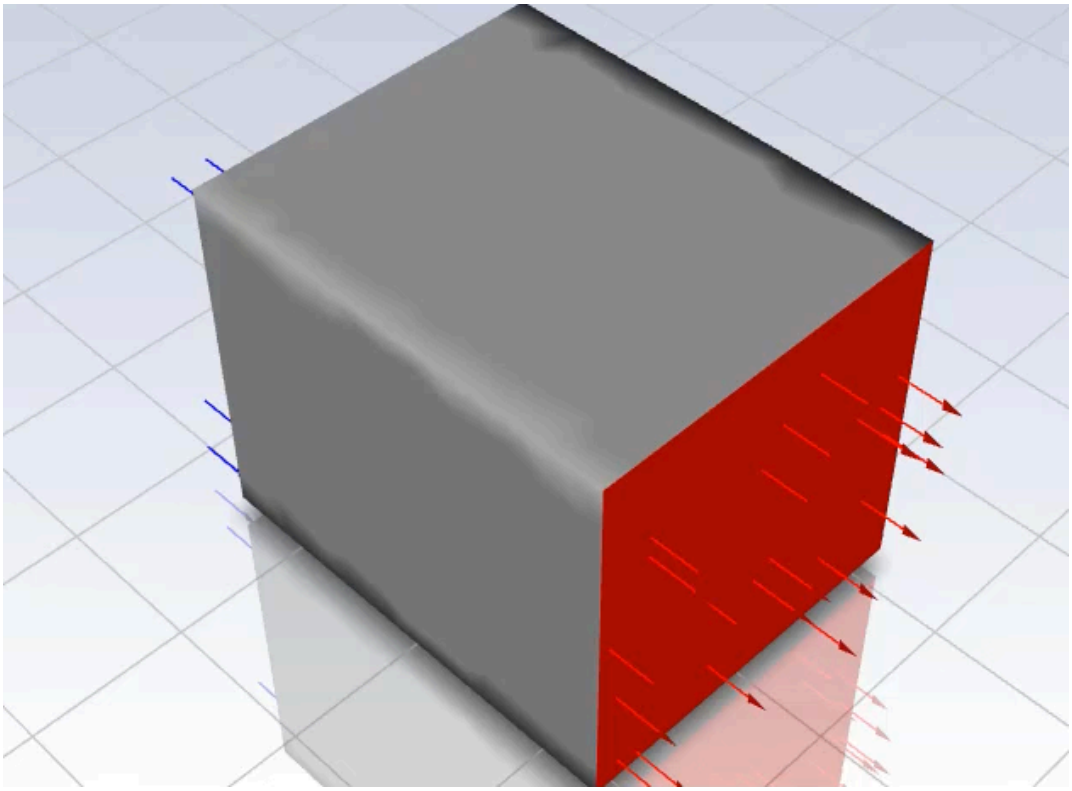


Figure 5.5: Flow direction

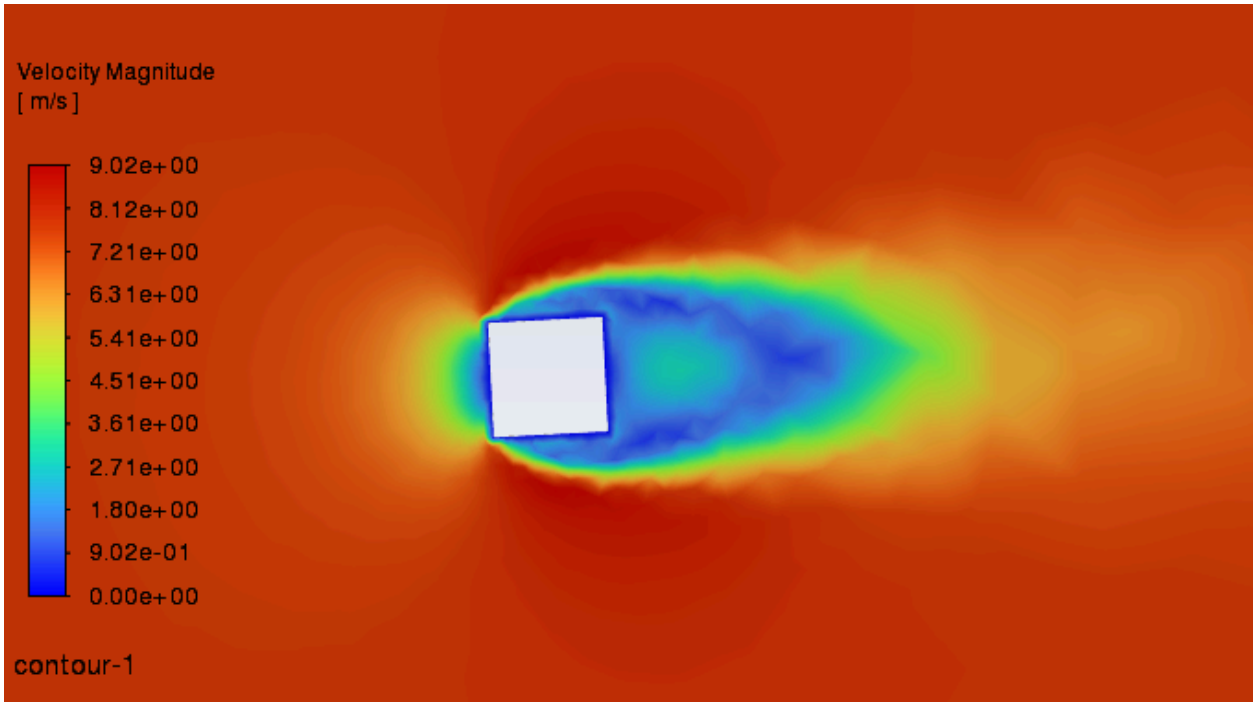


Figure 5.6: Velocity contour

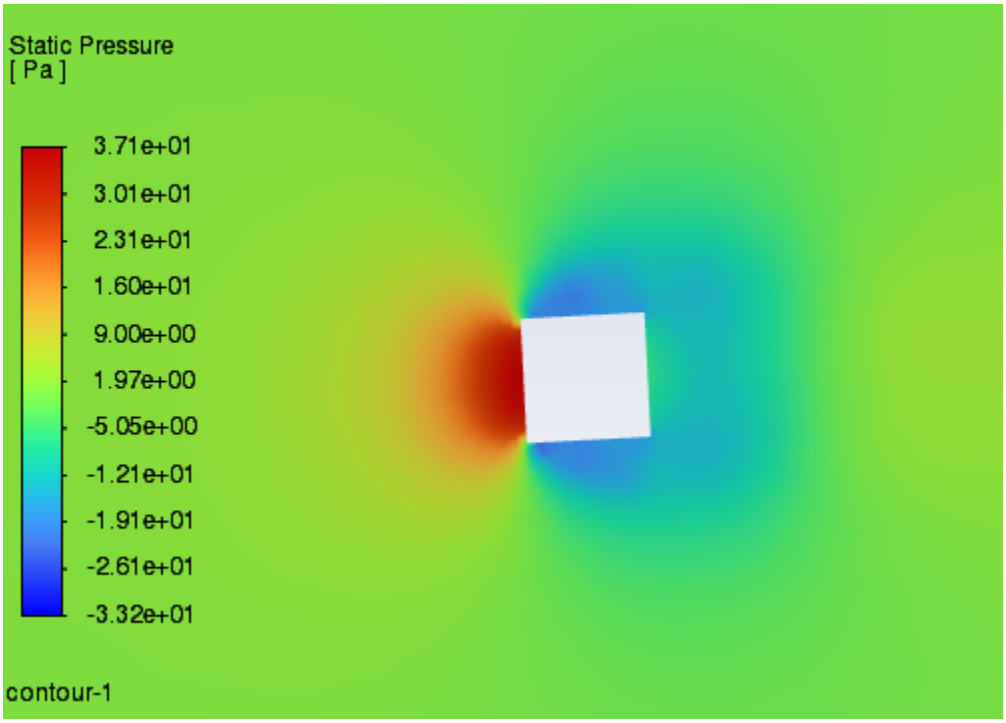


Figure 5.7: Static pressure contour

As a better visualization of the flow, we can see in Figure 5.5 the flow going from the inlet, through the enclosure, and out through the outlet. These flows match the contour results in Figures 5.6 and 5.7.

In Figure 5.6, we are presented with the velocity contour. As the freestream approaches the front of the cubesat, the flow quickly decelerates, forming a stagnation region which is characterized as low velocity. This can be seen in the blue coloring. The separation occurs in the leading edge due to the body's geometry, resulting in a wake region downstream of the CubeSat. This is defined as we can see the significantly reduced velocity and gradual recovery further downstream.

In Figure 5.7, we can see the static pressure contour. A region in the front face of the CubeSat is formed, which is consistent with the stagnation pressure effect we saw previously. A low-pressure region forms downstream of the CubeSat because there is flow separation and recirculation. The pressure difference between the front and the back is a huge factor in the pressure drag, which explains the high drag coefficient obtained in the results. Overall, the velocity and pressure contours are consistent with the body's geometry and provide a qualitative validation of the computed drag trends for a CubeSat under LEO flow conditions.

5.4 Discussion and Validation

After completing validation through simulation, we can finally compare our results against theoretical equations and handwritten calculations. The equation for the drag coefficient of a cube can be written as:

$$C_D = \frac{D}{A*0.5*r*V^2} \tag{5.5}$$

The $A * 0.5 * r * V^2$ can be written as the dynamic pressure, so we can simplify the drag equation to:

$$C_D = \frac{D}{q*A} \tag{5.6}$$

Knowing the values of ρ and V, we can calculate the dynamic pressure:

$$q = \frac{1}{2}\rho V^2 \tag{5.7}$$

$$q = 0.5(1.225)(59.29) = 36.3\,Pa \tag{5.8}$$

Lastly, we can validate our results by solving for the reference area:

$$C_D = \frac{D}{q^*A} = A = \frac{D}{qC_d} \tag{5.9}$$

$$A = \frac{0.3778}{(36.3)(1.0404)} = \frac{0.3778}{37.79} = 0.010m^2 \tag{5.10}$$

$$L = \sqrt{A} = \sqrt{0.010} = 0.100m = 100mm \tag{5.11}$$

With these calculations, we can say that these results are valid. The reference area result of 100 mm is exactly what our CubeSat's size is. Therefore, the reported drag and drag coefficients are consistent with the inlet speed that was used.

6. ESMD Assembly

6.1 Structure Assembly

6.1.1 CubeSat Assembly

The structural components of the 1U ESMD were 3D printed using polyethylene terephthalate glycol, also known as PETG. As mentioned in chapters one and two, aluminum alloy is too expensive, so a cheaper material was introduced. However, PETG was used instead of PLA due to its greater strength, durability, and temperature capacity. The pricing was justified and well within the allocated budget.

The structural components of the 1U ESMD CubeSat consist of a top panel, a bottom panel, three chassis walls, one modified chassis wall for payload access, four vertical corner beams, and four connector pins. These components were all individually fabricated using a 3D Printer, which will be summarized in Table 6.1.

Table 6.1: ESMD structural components

Structural Component	Amount	Unit Filament (g)	Total Filament (g)	Unit Print Time
Top Panel	1	27.93	27.93	0:45:47
Bottom Panel	1	27.93	27.93	0:45:47
Chassis Wall	3	16.43	49.29	0:30:55
Modified Chassis Wall	1	14.41	14.41	0:28:28
Corner Beam	4	19.34	77.36	0:32:19
Connector Pin	4	0.50	2.00	0:08:30

As we can see, Table 6.1 summarizes the structural components printed and used in the 1U ESMD CubeSat that were fabricated using PETG filament. The total weight of the CubeSat without electronics, taken from the table, is 198.92 grams. Again, PETG filament was used to improve the strength, thermal resistance, and durability. PETG's properties made it more suitable for prototyping the ESMD CubeSat while also remaining significantly lower cost than aluminum alloy.

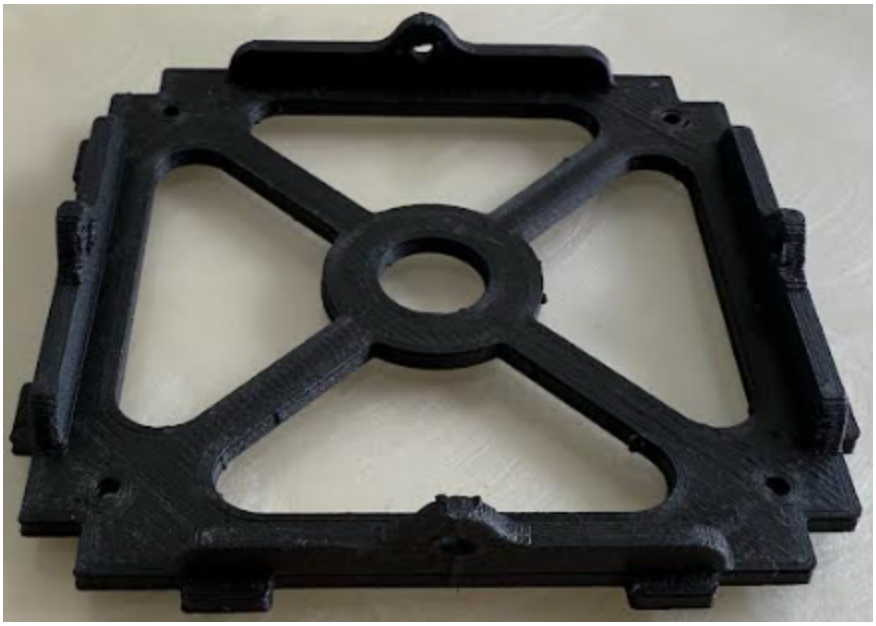


Figure 6.1: Printed top panel

The top and bottom structural panels provide the primary mounting surfaces for internal subsystems and electronic components. Therefore, they will be slightly different from the side chassis walls and will be a little heavier in weight. These panels include integrated mounting features and structural ribs to increase stiffness, as seen in Figure 6.1.

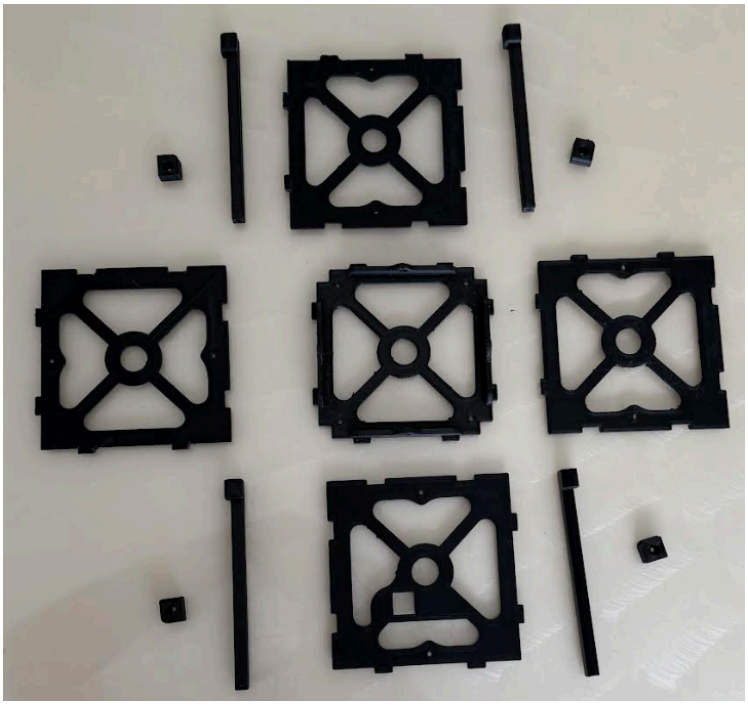


Figure 6.2: Laid out components

Before assembly, all printed components were inspected for dimensional accuracy and surface defects to ensure that they fit properly. The complete set of structural components used in the CubeSat frame is shown in Figure 6.2. As we can see, the top, the bottom panel, chassis walls, corner beams, and connector pins were all laid out and arranged before integration.

Once fabrication was completed and components were verified, the structural assembly process proceeded by attaching the corner beams to the base panel, followed by mounting the chassis walls and securing the structure using connector pins. The resulting assembly forms the primary CubeSat frame used to support the electronic payload and internal subsystems.

6.1.2 Base Panel Assembly

To start the assembly process, the CubeSat structure begins with the bottom structural panel. This serves as the primary foundation for the CubeSat frame. The bottom panel provides the mounting interface for the vertical structural elements and establishes the geometric alignment of the overall structure. The panel was positioned on a flat surface to ensure proper alignment before attaching the remaining structural components.



Figure 6.3: Vertical corner beams

Following placement of the base panel, the four vertical corner beams were installed at each corner of the panel. These beams function as the primary load-bearing members of the CubeSat structure and provide the vertical support necessary to connect the top and bottom panels. Each beam was aligned with the designated mounting points on the base panel and secured using the

printed connector pins. The beams ensure the structural rigidity of the CubeSat frame while maintaining the required 1U form factor dimensions.

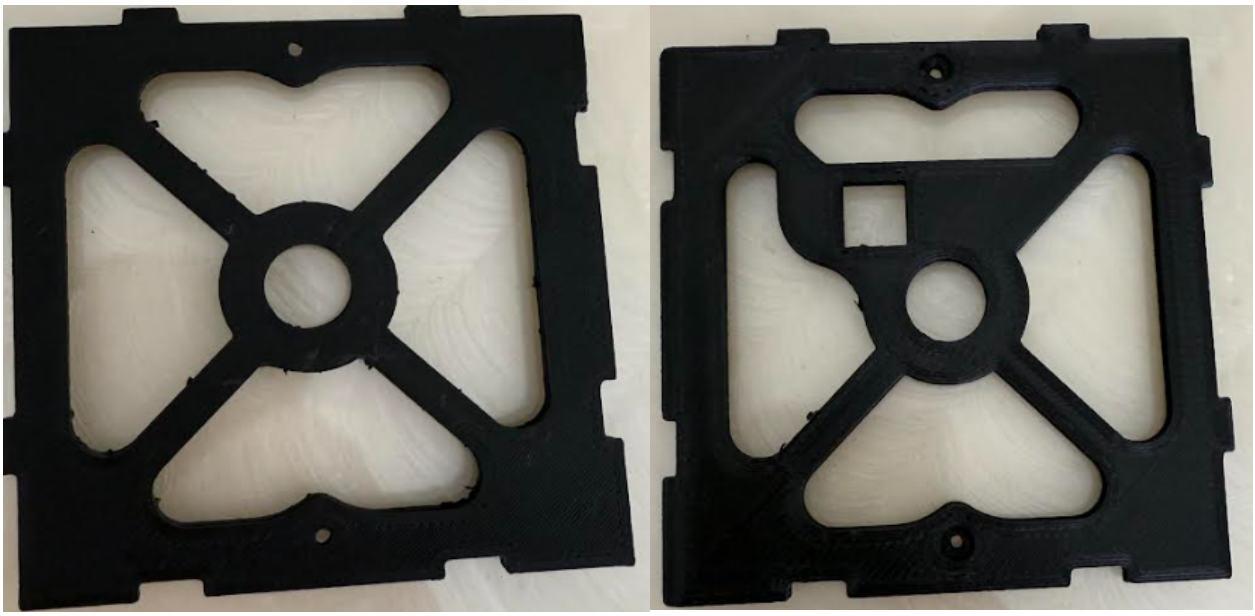


Figure 6.4: Chassis walls

Once the corner beams were secured to the base panel, the three standard chassis walls and one modified chassis wall were attached to the frame. The modified wall includes a dedicated opening to accommodate the payload and electronic subsystem interfaces. These walls provide lateral structural support and serve as mounting surfaces for internal components such as the electronics payload and sensor hardware.

To attach the vertical beams, chassis walls, and the top/bottom panels together, proper alignment was needed. The use of connector pins can be used to fasten and ensure that the structure maintains the correct CubeSat geometry. These connector pins are tied at the top of the CubeSat and can be seen in Figure 6.5.



Figure 6.5: Connector pins

After all structural panels were secured, the partially assembled structure formed a rigid frame extending upward from the base panel. This configuration provided the necessary support for the final installation of the top panel and the integration of the electronic payload described in the following section.

6.1.3 Payload Mounting Assembly

After finishing the construction of the outer structural frame, the CubeSat was then prepared for integration of the electronic payload and internal subsystems. The 3D printed structure provides a great mounting surface on the interior faces of the chassis walls. This allows the electronic components to be secured properly within the CubeSat. The internal layout was designed to ensure that the electronics remained properly supported while maintaining sufficient space for wiring and sensor placement.

The modified chassis wall was specifically designed to accommodate payload interfaces and sensor placement. The openings on the side panels provide external access for measurement devices and a mounting location for the radiation detector used in the ESMD. This configuration ensures that the sensor can be exposed to the surrounding environment while remaining protected within the structural frame.

Once the payload mounting locations were verified, the top structural panel was installed to complete the CubeSat frame. The top panel was aligned with the corner beams and secured using the connector pins, creating a rigid enclosure for the internal components. The completed structure forms a fully enclosed 1U CubeSat frame that supports the electronic payload and provides mechanical protection during handling and testing.

The fully assembled CubeSat structural frame is shown in Figure 6.5, illustrating the final configuration of the printed PETG structure before installation of the electronic subsystems described in the following section.

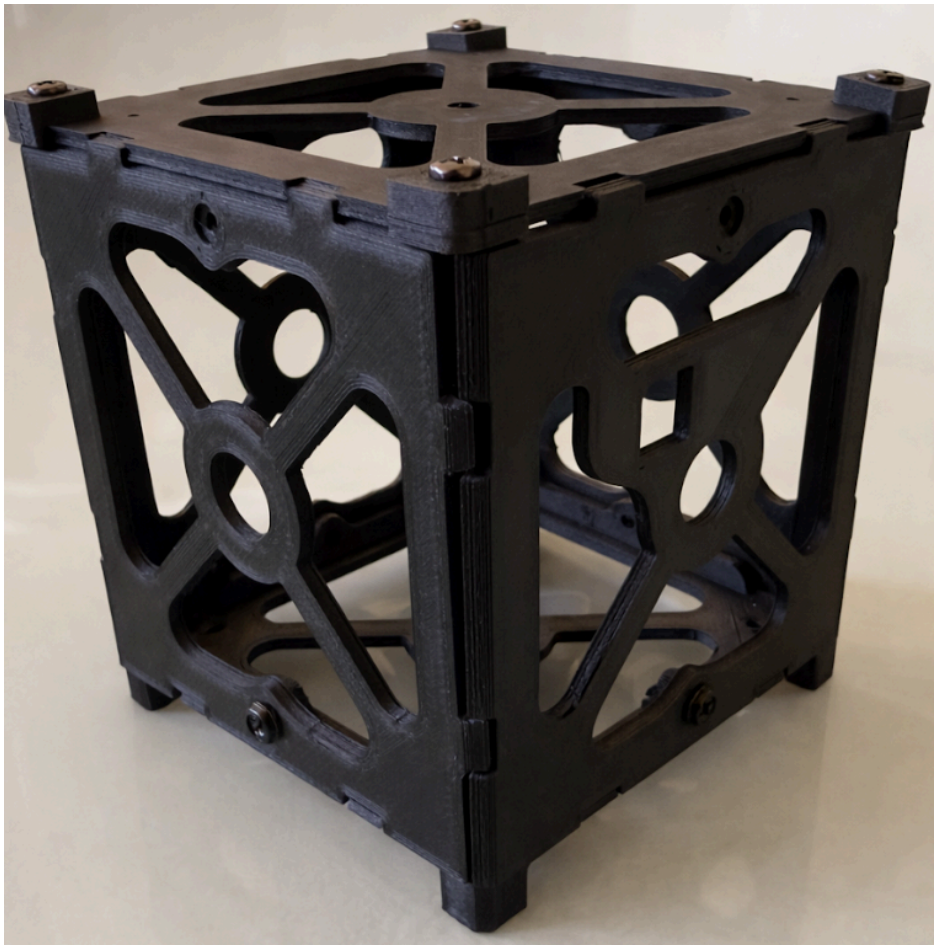


Figure 6.6: Cubesat skeleton completely assembled

6.2 Electrical Assembly

The next step is to assemble the electrical subsystem of the ESMD CubeSat. This subsystem consists of an Arduino, a power supply system, a radiation sensor, and a data acquisition chip. These components work together to detect radiation counts and record measurement data in the data acquisition chip for later analysis. All together, the electrical assembly integrates the Arduino, the Geiger counter radiation detector, a data logging system, and a portable power supply to create a mobile measurement device capable of detecting radiation in LEO.

6.2.1 Arduino Assembly

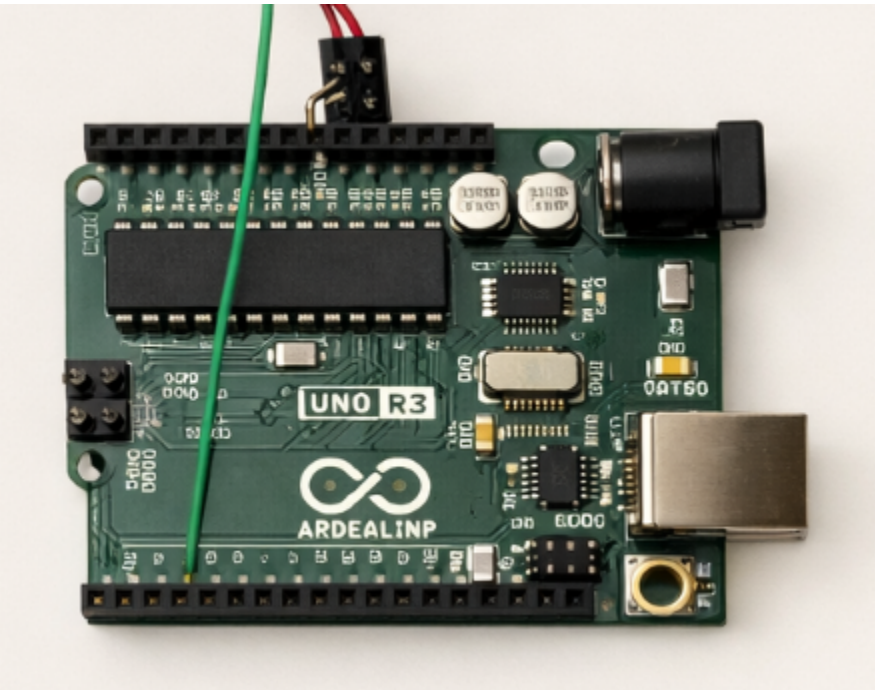


Figure 6.7: Arduino microcontroller used for the ESMD payload

The Arduino Uno R3 microcontroller serves as the main processing unit for the ESMD payload. The Arduino is responsible for receiving signals created by the radiation detector and converting these signals into measurable radiation counts. The Arduino processes the incoming signals, calculates radiation intensity values with a specific conversion rate stated in its code, and transmits the resulting data to the onboard storage system. The Arduino proves to be of great use to the ESMD because of its low cost, open-source architecture, and compatibility with the radiation geiger counter.

6.2.2 PCB and Power Supply Assembly

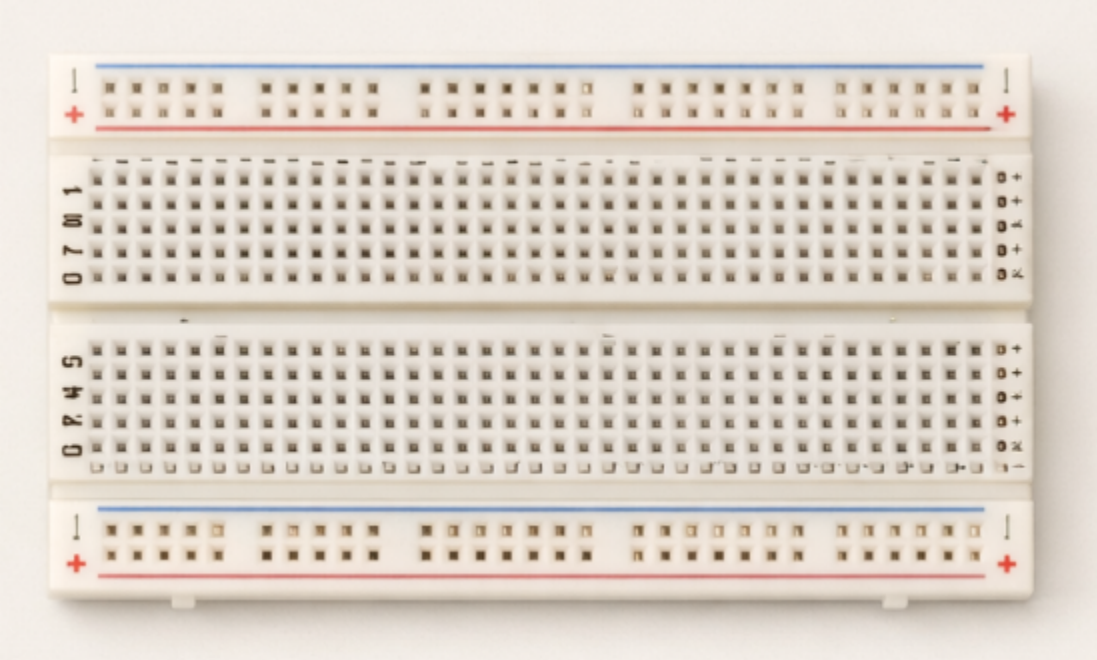


Figure 6.8: PCB breadboard used



Figure 6.9: 9v battery used for portable power

In order to have a smooth electrical flow between the various components, a PCB was incorporated into the electrical payload. The PCB allows the microcontroller, sensor modules, and data acquisition hardware to be connected. This helps enable rapid testing and modification of the electronic configuration. During initial testing and programming, the Arduino was powered directly through a USB connection to a laptop, which allowed the device to be controlled and monitored through the Arduino development environment.

For the ESMD to move freely throughout LEO, a 9V battery was integrated into the system to provide an independent power source. The battery is first connected to the PCB, and then the PCB is connected to the Arduino. This is done to reduce the risk of voltage fluctuations, shortages, and electrical damage that may occur when in LEO. In addition, the independent power source allows the system to operate as a portable radiation measurement device. Note that the bigger the power source used, the longer the mission can continue.

6.2.3 Data Acquisition System

The ESMD payload incorporates a data acquisition system to record radiation measurements during operation. An SD card chip that is compatible with the PCB and Arduino is connected to the electrical subsystem. This allows radiation count data to be stored locally on the ESMD CubeSat. During operation, the Arduino will continuously read the pulse signals generated by the radiation detector and record the corresponding radiation intensity values onto the SD card. This data logging capability enables long-duration measurements and allows the collected radiation data to be retrieved later for analysis and visualization. Not that the bigger the SD space, the longer the mission can go.



Figure 6.10: SD card compatible with arduino

6.2.4 Radiation Sensor Assembly

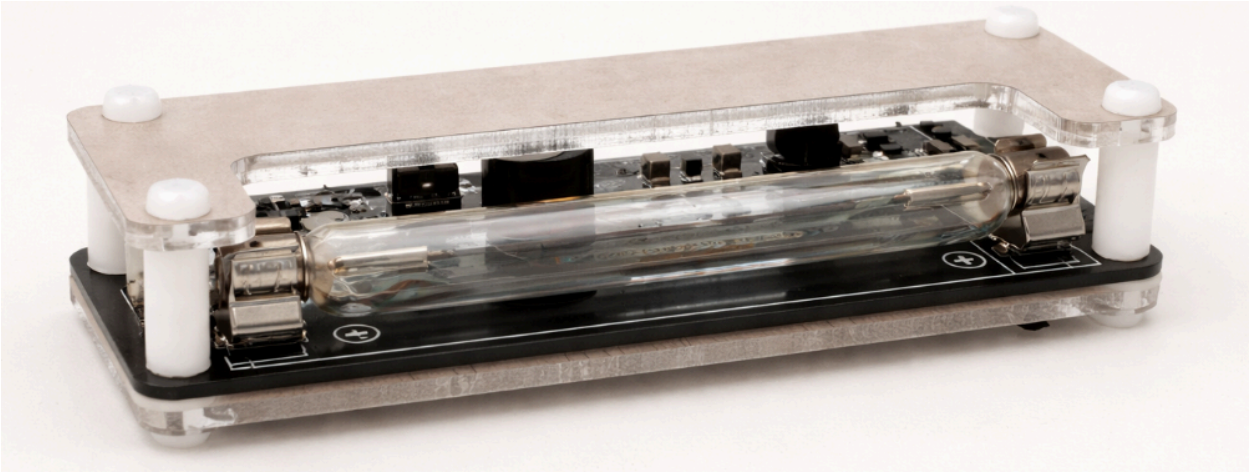


Figure 6.11: Geiger counter used

The primary sensing component of the ESMD payload is the Geiger counter radiation detector. The Geiger counter operates by detecting ionizing radiation particles that interact with the gas contained inside the Geiger–Müller tube. When radiation enters the tube, it ionizes the gas molecules, generating an electrical pulse that is detected by the sensor circuitry. Each pulse corresponds to a radiation event, which is then transmitted to the Arduino microcontroller.

The Arduino counts these pulses over a specified time interval and converts the measurement into radiation intensity values such as counts per minute or microsieverts per hour (μSv/h). This conversion is done by using a specific conversion rate written in Arduino's programming code. These measurements then indicate the surrounding radiation environment and form the basis for the radiation data collected by the CubeSat payload.

6.2.5 Wiring and Connection

The final stage of the electrical assembly involved establishing the wiring connections between the power supply, microcontroller, radiation sensor, and data acquisition components. As mentioned earlier, the electrical subsystem of the ESMD CubeSat consists of a 9 V battery power source, a PCB, an Arduino, a Geiger counter radiation detector, and an SD card. The wiring configuration used to integrate these components can be seen below in Figure 6.12.

Power is supplied to the system using a 9 V battery, which provides a portable and independent power source for the CubeSat electronics. The battery is first connected to the PCB distribution board, which serves as a centralized point for distributing electrical power to the remaining components. This configuration helps regulate the electrical connections and reduces the risk of voltage irregularities affecting the Arduino.

From the PCB distribution board, power is delivered to the Arduino, which serves as the central processing unit of the ESMD payload. The Arduino manages the communication between the radiation sensor and the data logging system by taking the data and using a specific conversion rate embedded in the Arduino's code. In addition, the Arduino will control the overall operation of the measurement device.

Next, the Geiger counter radiation detector is connected directly to the Arduino through its signal output line. This output line consists of electrical wiring that was taken apart and soldered onto the Arduino for peak connection. When ionizing radiation interacts with the Geiger–Müller tube inside the detector, an electrical pulse is generated and transmitted to the Arduino. The microcontroller continuously monitors this signal, counts the number of pulses detected within a specified time interval, uses a conversion rate, and determines the radiation intensity.

In addition to the radiation detector being connected to the Arduino, the SD module is also directly connected to the Arduino. This SD module serves as the data acquisition and storage system. Radiation measurements calculated by the Arduino's conversion rate are written to the SD card during operation, allowing the collected data to be retrieved later for analysis and visualization.

The complete wiring configuration between the battery power supply, PCB distribution board, Arduino microcontroller, Geiger counter module, and SD card data logging system is shown in Figure 6.12.

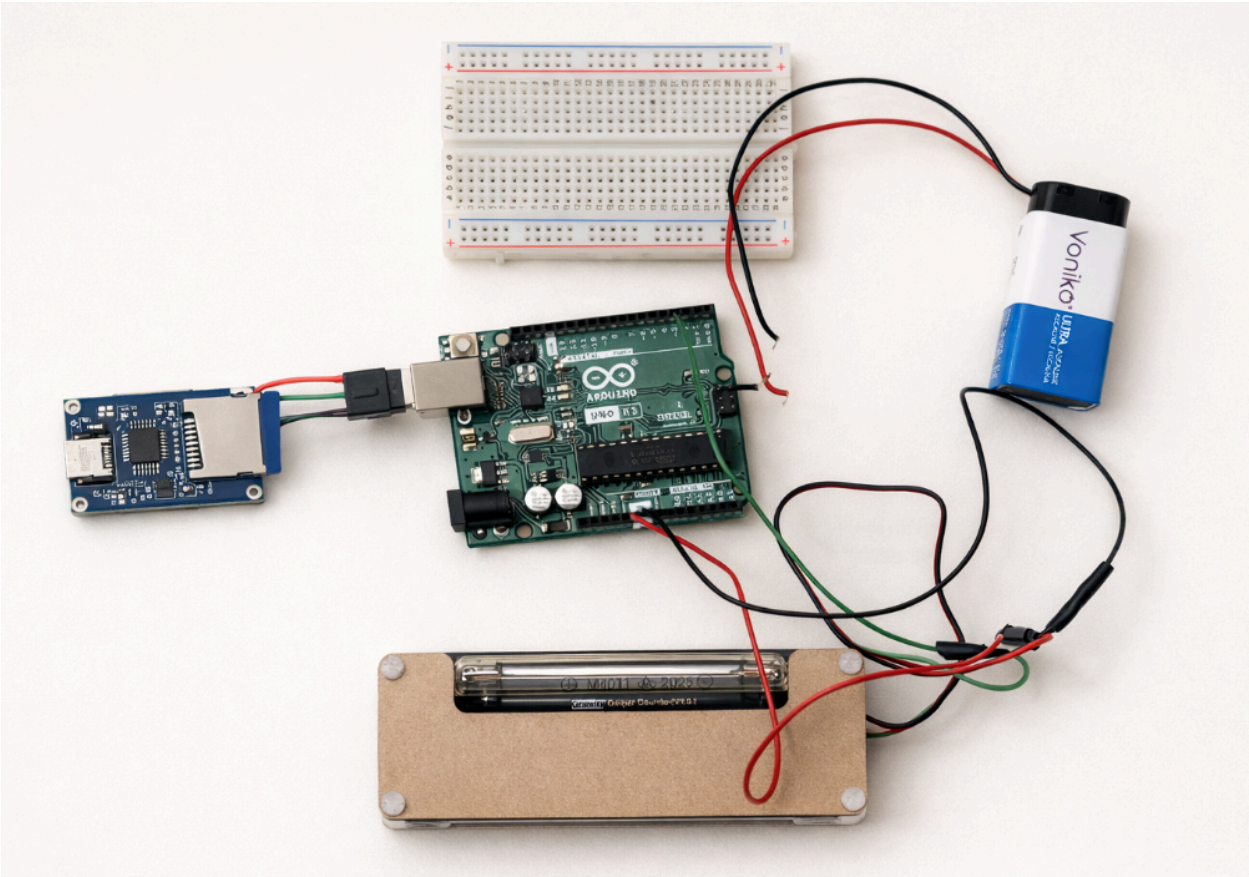


Figure 6.12: Completed electrical wiring

7. Verification and Validation testing

7.1 Verification

Now that we are finished with the wiring and the structural building, we can put together our cubesat. After putting together our cubesat, the fun begins. We can start turning on our system and running checks. After verifying our system works, we can validate our goal by incorporating integration tests and see if our mission goal is met.

The finished assembled cubesat can be seen below in Figure 7.1. As mentioned in Chapter 6, this fully assembled CubeSat includes the structural frame, Arduino, Geiger counter, power system PCB, and DAQ.

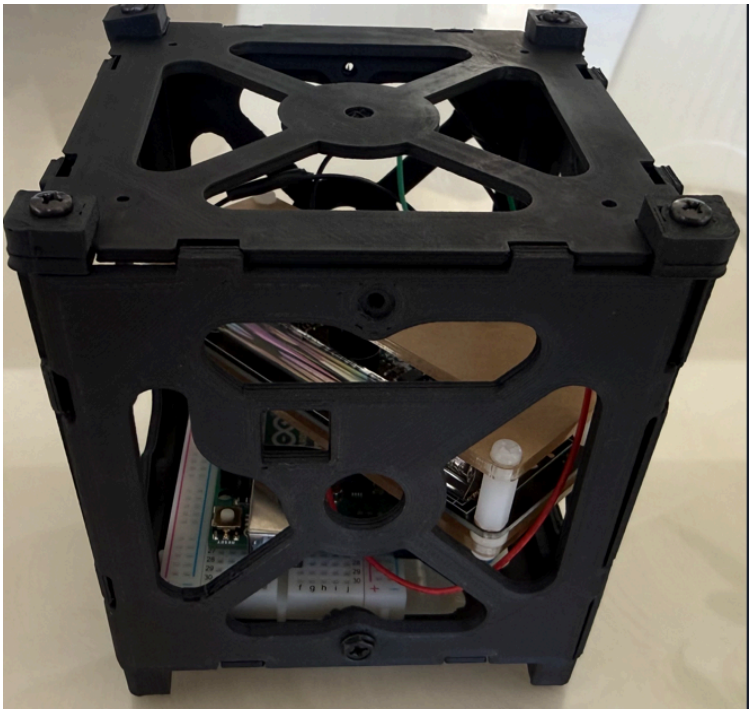


Figure 7.1: Fully assembled ESMD

7.1.1 Power On Test

The first test run on the ESMD CubeSat for verification is the power-on test. This test serves as a first-stage preliminary check to see if the electrical subsystems, the Geiger counter, and the Arduino work. The power on test will ultimately confirm that power is properly distributed throughout the system and that all electrical components respond properly when energized.



Figure 7.2: First power-on test



Figure 7.3: Second power-on test

During this test, the CubeSat was powered in two separate ways. The first way was using the adapter connected to the Arduino, and the second was to simulate mobile movement using the 9 V integrated battery. These tests were done at separate times, and the electrical connections between the PCB, Arduino, and the Geiger counter were mainly observed. There was a success in power distribution as the LEDs on both the Arduino and the Geiger counter lit up. Additionally, you can already hear the Geiger counter's buzzer going off, as there was no code interpreted in the machine, and it was powered on. When a code is implemented on the Arduino for the counter, it will play a beeping noise similar to a smoke detector.

The illuminated LED indicators shown in Figures 7.2 and 7.3 confirm that the Arduino received power from its adapter and the 9 V battery source. This verifies that the power supply, wiring, soldering, and components were correctly assembled and should be operational.

The power-on test does not verify the functionality of the Geiger counter or the data acquisition system. However, it confirms that the CubeSat is electrically stable and ready for the next step of subsystems verification and validation testing. Therefore, the power-on test is a critical step in identifying wiring faults, loose connections, and power-distribution issues before moving on to more advanced verification and validation tests.

7.1.2 Subsystems Check

After the successful power-on verification test, a series of quick and thorough subsystem-level checks was conducted to ensure that individual components of the ESMD CubeSat operate as intended. The purpose of these tests is to verify each subsystem's function.

The first subsystem that was tested and observed was the Geiger counter. When first powering the ESMD, the counter started generating periodic pulse noises. These are the pulses that transmit data signals to the Arduino through the configured input pins with proper wiring and coding. Because there was visual and auditory confirmation that the counter worked, this subsystem's check received a pass grade.

The Arduino microcontroller was then monitored to confirm proper signal processing. Using the serial interface, radiation measurements were observed as count rates, indicating that the microcontroller successfully interpreted incoming detector signals. The measured values increased incrementally over time, demonstrating continuous detection and processing of radiation events. Therefore, this also received a pass grade.

Additionally, the stability of the electrical subsystem was evaluated during operation. The system was left on for a few minutes and maintained consistent power delivery without interruptions. LEDs remained stable, confirming proper electrical behavior under operational conditions.

Although these subsystem checks confirm that the sensor and processing units are functioning correctly, they do not yet validate the data connectivity flow, as we have not received any data. Further verification testing is required to confirm data connectivity and flow.

7.1.3 Data Connectivity Test

After the subsystems are successfully verified, the next test is the data connectivity test. The purpose of the data connectivity test is to verify the integrity of the data transmission. This transmission starts from the radiation detector, then funnels to the Arduino, and feeds into the DAQ system.

To perform this test, the system was turned on and operated for approximately five minutes. During this period, the Geiger counter generated radiation pulse signals, which were processed by the Arduino and transmitted to the DAQ through the established communication interface.

After the set of test data was collected, the DAQ module was then connected to a computer and its associated software to analyze the time stamps and data collected. The resulting dataset should consist of two measurements. The x-axis will be time, and the y-axis will be the measured radiation value.

Table 7.1: DAQ dataset received

Time (s)	**Dose Rate (µSv/hr)**
17:45:20	0.12
17:45:21	0.10
17:45:22	0.15
17:45:23	0.13
17:45:24	0.11
17:45:25	0.14

As seen in Figure 7.4, the DAQ successfully recorded data, verifying that the signal pathway from the sensor to the Arduino to the data storage system is functioning correctly. We can see the specific time stamps that the DAQ recorded during the time of day, the time (in seconds), and the measurement of radiation within that area in the last column.

This test is critical in verifying system-level data integrity before deployment. Conducting this validation on the ground ensures that potential issues in data transmission are identified early, avoiding the loss of valuable data during extended mission operations in LEO, where testing opportunities are limited and costly.

Based on the successful retrieval and interpretation of the recorded dataset, the data connectivity test is considered to have passed, confirming proper integration of the sensor, microcontroller, and DAQ subsystems.

7.2 Validation

After completing subsystem verification, validation testing is needed to assess whether the ESMD CubeSat meets the mission objective. As mentioned in chapter one, the mission objective is to measure and record radiation levels in LEO environment. Verification ensures that individual components and subsystems function correctly, while validation determines whether the integrated system produces reasonable data consistent with expected physical behavior.

The validation phase focuses on evaluating the overall system performance, including sensor response, data consistency, and system-level integration. These tests are designed to simulate realistic operational conditions and confirm that the CubeSat is capable of collecting and storing radiation data over time.

7.2.1 Functional Integration Test

The functional integration test evaluates the performance of the fully assembled ESMD CubeSat as a complete system. The objective of this test is to confirm that all subsystems, such as the radiation sensor, Arduino, power system, and DAQ, operate together without any issues. In the end, we are checking if the ESMD produces continuous and meaningful radiation measurements.

To conduct this test, the CubeSat was powered on and operated continuously while collecting radiation data over a fixed duration. This test was set for approximately five minutes. During the operation, the Geiger counter detected radiation events and transmitted pulse signals to the Arduino, which could be audibly heard. The Arduino then processed the data and converted it into measurable radiation units. The processed data was sent directly to the DAQ and reviewed on the desktop for readable data.

Overall, the system remained stable throughout the entire test period. There were no interruptions in terms of power and data transmission. Radiation measurements were recorded continuously, and the data exhibited expected behavior. From previous research, it was expected that there would be a gradual variation in count rate over time. This indicates that the sensor is actively detecting background radiation and that the data pipeline functions correctly.

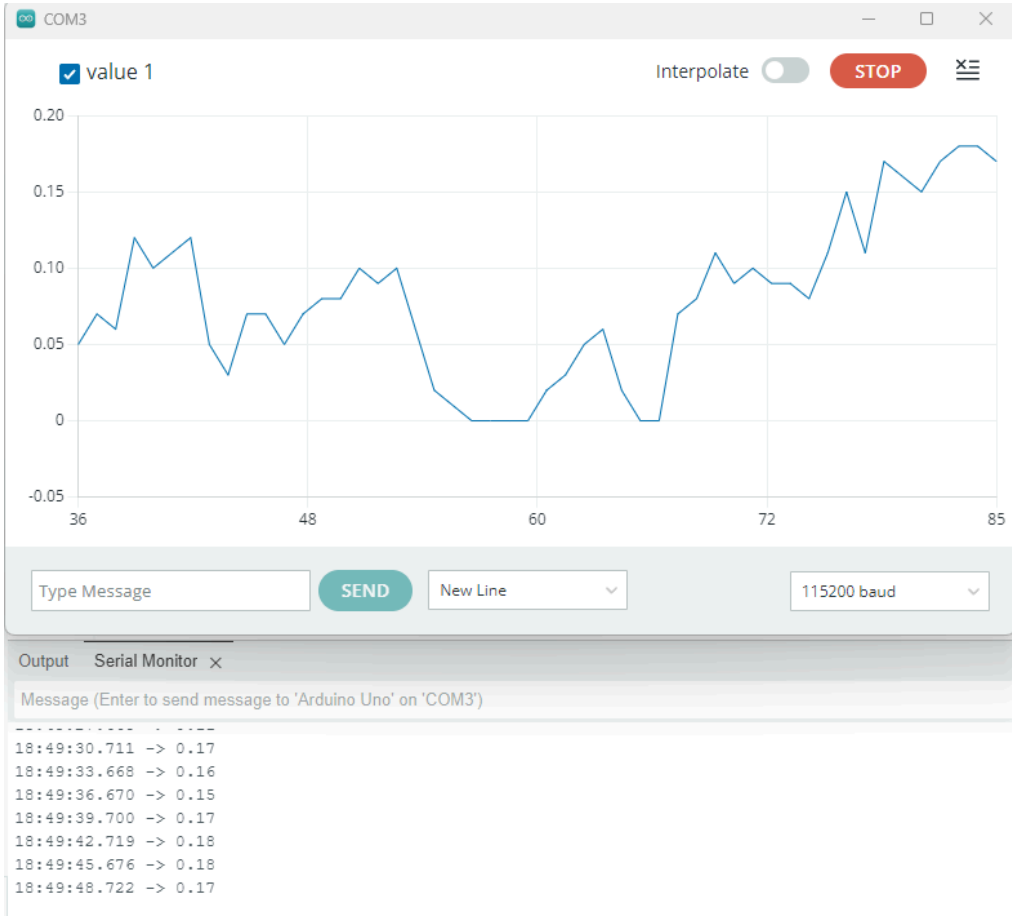


Figure 7.4: System integrated µSv/h plot

The results of this test demonstrate successful integration of all major subsystems. Figure 7.5 shows us the built-in Arduino IDE software and its serial monitor. As we can see in the figure, the system produces continuous radiation measurements over time with observable variation in the signal. This behavior is consistent and expected with the background radiation fluctuating. This actually indicates that the sensor and data processing pipeline are functioning correctly under operations. Unlike the verification tests in Section 7.1, which evaluated individual components, this test confirms that the entire ESMD CubeSat operates as a unified system capable of performing its intended function.

This validation step is critical before deployment, as it ensures that the system can reliably collect and store data under continuous operation. Based on the successful performance observed during testing, the functional integration test is considered to have passed, indicating that the CubeSat meets its primary operational requirement for radiation data collection.

7.2.2 Environmental Testing Conditions

To evaluate system performance under varying environmental conditions, a series of ground-based tests was conducted using the fully integrated ESMD CubeSat. These tests were designed to simulate different radiation interaction environments and assess how external surroundings influence measured radiation levels.

Two primary test conditions were selected:

1. Baseline Condition (Concrete surface)
2. Metal Interaction Condition (On top of a metallic structure)

Each test was conducted for a duration of approximately 10 minutes or 600 seconds. During the 10 minutes, radiation measurements were continuously recorded. This duration was selected to provide sufficient data for observing trends while maintaining consistency across test cases. It is noted that longer-duration testing is feasible and could be extended until battery depletion to better simulate long-term operation in LEO.

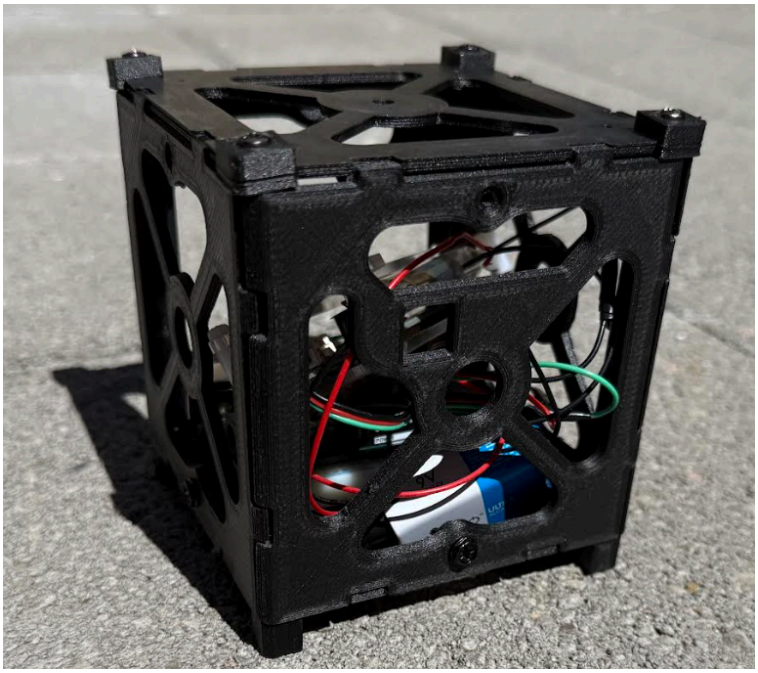


Figure 7.5: Baseline test condition

The baseline test was conducted with the CubeSat placed directly on a concrete surface in an open outdoor environment. As we can see in Figure 7.6, the ESMD was laid out on concrete. This condition represents a nominal ground reference with minimal nearby conductive or shielding materials. During this test, the system operated continuously and recorded background

radiation levels. This dataset serves as a reference for comparison against other environmental conditions.

To evaluate the effect of nearby conductive materials on radiation measurements, the CubeSat was placed on a metallic surface (the roof of a metal structure), as shown in Figure 7.7. Metallic environments can influence radiation detection through scattering, reflection, or partial shielding effects.

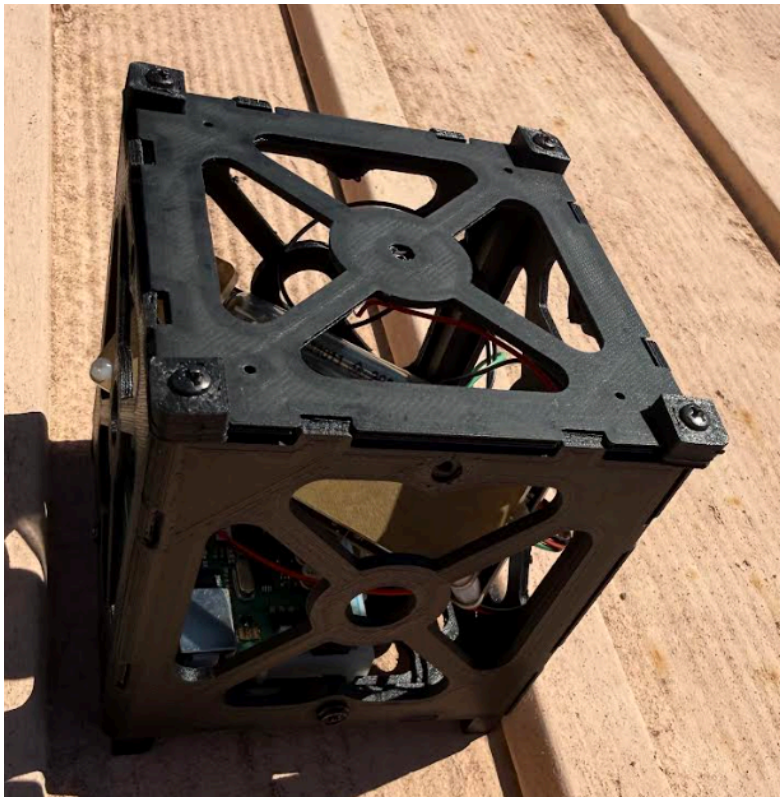


Figure 7.6: Metallic interaction test

The system was again operated for approximately 10 minutes under identical conditions to the baseline test. Any variation in recorded radiation levels between this test and the baseline condition provides insight into the environmental sensitivity of the sensor system.

All tests were conducted outdoors under clear sky conditions with direct solar exposure, as shown in Figure 7.8. Ambient environmental factors such as solar radiation, atmospheric conditions, and surrounding materials contribute to the measured radiation profile.

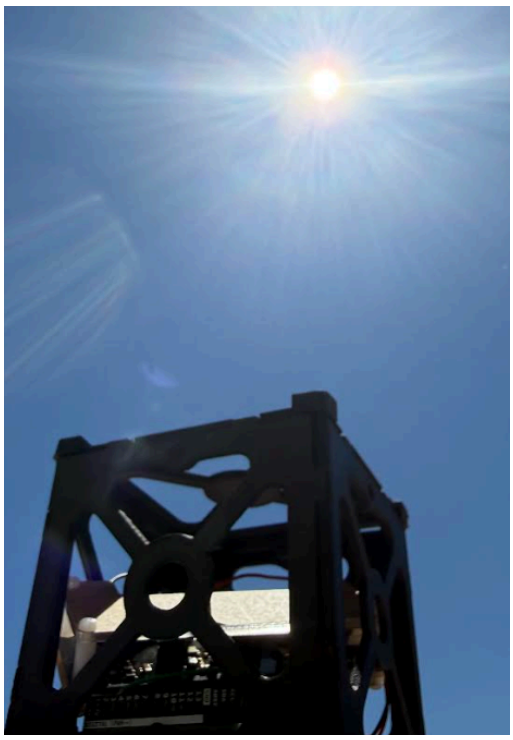


Figure 7.7: Test environment and solar conditions

These environmental tests are critical for validating system performance before deployment. In Low Earth Orbit, the CubeSat will be exposed to varying radiation environments influenced by spacecraft orientation, shielding, and external structures. Ground-based testing in different material conditions provides an initial assessment of how environmental factors may impact sensor readings.

By comparing results between baseline and metal-interaction tests, the system's sensitivity to surrounding materials can be evaluated. This ensures that the measured radiation data is interpreted correctly during mission operations.

7.2.3 Data Validation Test

The data validation test is performed to assess whether the radiation measurements collected by the ESMD CubeSat are physically meaningful and consistent across different environmental conditions. This test compares datasets obtained from a baseline condition and a metallic surface condition to evaluate system reliability and environmental sensitivity.

The baseline test results in Figures 7.9–7.10 represent radiation measurements collected on a concrete surface in an open outdoor environment. The time-series data shows continuous fluctuations in dose rate over the 10-minute interval, with values generally ranging between approximately 0.03 and 0.22 µSv/hr.

The raw data exhibit stochastic variation, which is expected due to the random nature of ionizing radiation detection. The smoothed curve highlights an underlying trend in the radiation levels, indicating stable sensor performance. The histogram distribution further shows that the majority of measurements cluster within a consistent range, confirming steady background radiation detection.

Overall, the baseline dataset demonstrates normal sensor behavior and provides a reference for comparison with other environmental conditions.

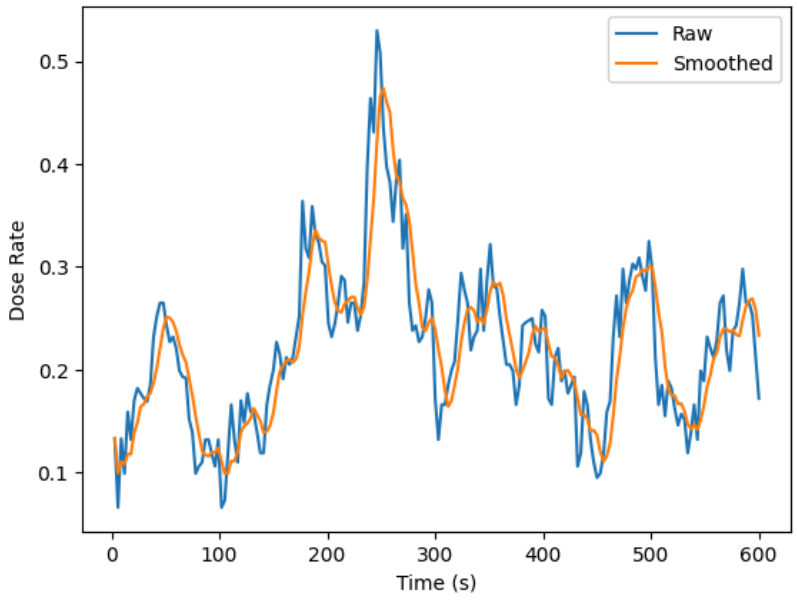


Figure 7.8: Baseline test results

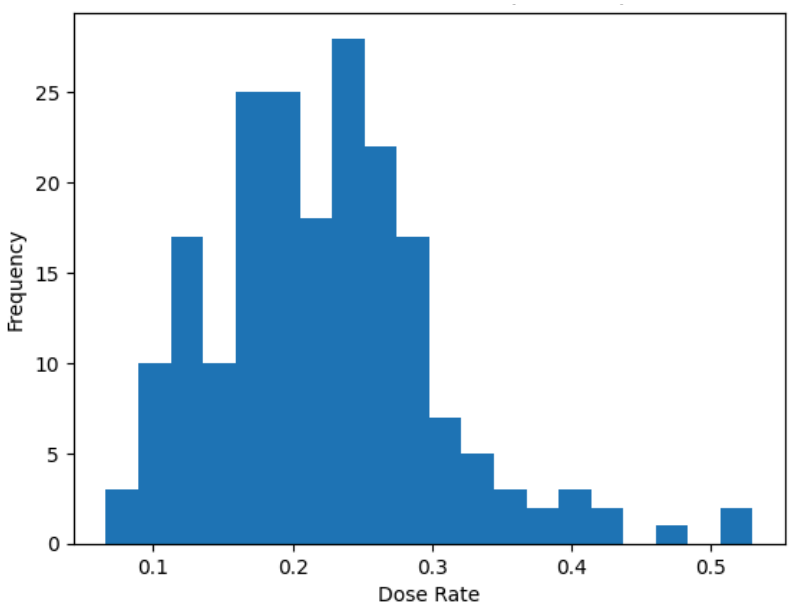


Figure 7.9: Baseline histogram of radiation dose rate

The metallic test results (Figures 7.11–7.12) were obtained by placing the CubeSat on a metallic surface under similar outdoor conditions. The time-series data again show continuous fluctuations in radiation dose rate over time, with values remaining within a comparable range to the baseline test.

Slight differences in the distribution and peak values are observed when compared to the baseline dataset. These variations are likely due to environmental interactions such as radiation scattering or partial shielding effects introduced by the metallic surface. Despite these differences, the overall behavior of the data remains consistent, with no abnormal spikes or system instability observed.

The histogram distribution for the metallic test also shows a similar spread of values, reinforcing that the sensor continues to operate reliably under different environmental conditions.

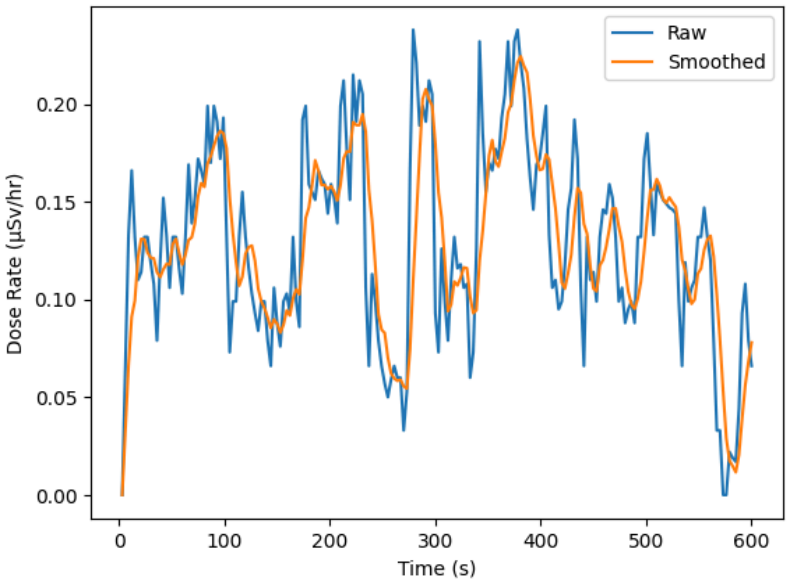


Figure 7.10: Metallic test result

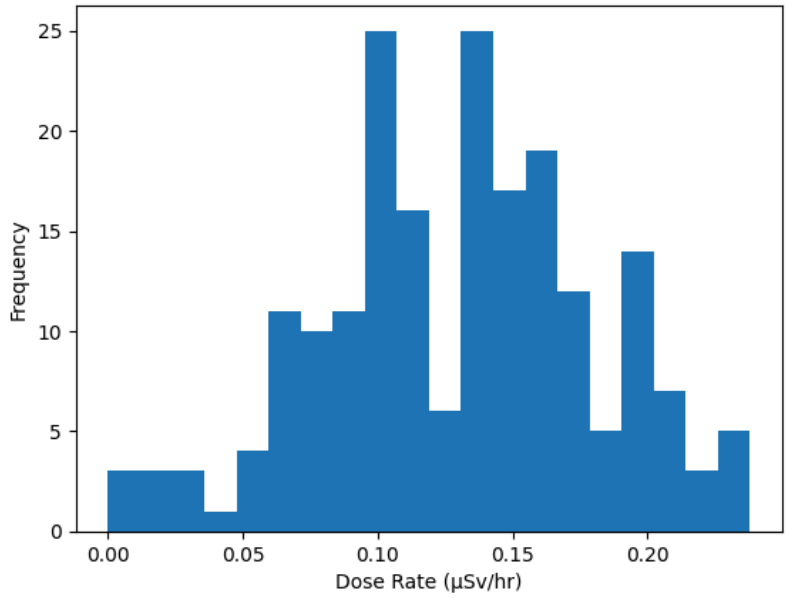


Figure 7.11: Metallic histogram of radiation dose rate

To further evaluate system performance, a direct comparison of the baseline and metallic datasets is shown in Figure 7.13.

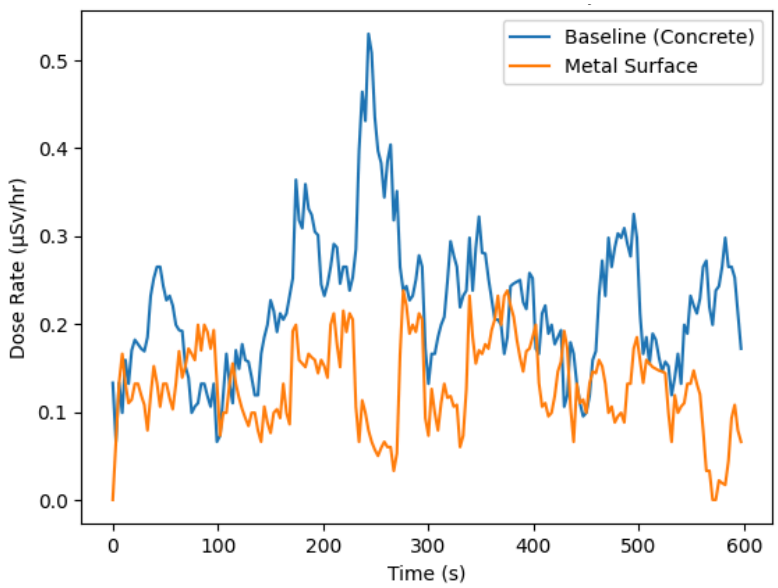


Figure 7.12: Comparison of dose rate measurements

From this comparison, both datasets exhibit similar trends and magnitudes in radiation levels. While minor deviations are present, the overall agreement between the two conditions indicates that the system produces consistent measurements regardless of environmental surface type.

The measured radiation dose rates in both tests fall within the expected range of natural background radiation (~0.05–0.20 µSv/hr). This confirms that the sensor is detecting realistic radiation levels and that the system is properly calibrated.

The observed fluctuations in both datasets are consistent with the probabilistic nature of radiation detection, where particle arrivals are inherently random. Additionally, the absence of signal dropouts or non-physical values confirms stable operation of the full data pipeline.

Based on the consistency between baseline and metallic datasets, agreement with expected radiation levels, and stable system performance, the data validation test is considered to have passed.

This validates that the ESMD CubeSat is capable of producing reliable and physically meaningful radiation measurements, supporting its intended application for radiation monitoring in Low Earth Orbit.

8. Conclusion and Future Recommendations

This work presented the design, development, and testing of a 1U CubeSat-based Energy Spectrum Measurement Device for radiation detection in Low Earth Orbit. The primary objective of this study was to demonstrate that a compact, low-cost system could reliably measure and record radiation data using a fully integrated sensor, microcontroller, and data acquisition architecture.

Through a series of verification and validation tests, the system was shown to operate as intended. Power-on testing confirmed proper electrical functionality, subsystem checks verified correct operation of individual components, and data connectivity testing validated the integrity of the signal pathway from the radiation sensor to the data acquisition system. Functional integration testing further demonstrated that the system could continuously collect and process radiation measurements over time without interruption.

Environmental testing under baseline and metallic surface conditions provided additional insight into how the system's performance will change under different conditions. The sets of data that were collected showed extreme fluctuation of ionizing radiation. The measured dose rates were then found to be consistent with expected radiation levels according to each background. The relationship between baseline and metallic test result behaviors confirmed that the system produced feasible data across different environmental conditions.

Overall, the ESMD CubeSat successfully meets its primary objective of detecting, processing, and recording radiation data. These results can verify that the system will be a viable platform for future radiation measurement missions in LEO.

While the current system demonstrates successful operation, several improvements can be made to enhance future performance and expand mission capability.

Future work should focus on incorporating a higher-sensitivity radiation detector. This will help enable more precise measurement of the energy spectra and the particle interactions in space. Additionally, the structural components can be further refined to use flight-grade materials such as aluminum alloys. This is used to improve the durability and thermal performance of the CubeSat in space. Lastly, a more advanced power system can be incorporated. This would include solar panels and a regulated distributed power system. A better power system would allow for extended mission duration beyond battery limitations.

Finally, the system can be expanded towards a full mission deployment. This can be done by integrating a full communication system for real-time data transmission and conducting orbital movements. With these improvements, the ESMD CubeSat has the potential to evolve into a fully operational platform for radiation monitoring and space environment characterization.

References

[1] Ginet, G. P., O'Brien, T. P., Huston, S. L., Johnston, W. R., Guild, T. B., Friedel, R., Lindstrom, C. D., Roth, C. J., Whelan, P., Quinn, R. A., Madden, D., Morley, S. K., and Su, Y.-J., "AE9, AP9, and SPM: New Models for Specifying the Trapped Energetic Particle and Space Plasma Environment," Space Science Reviews, Vol. 179, No. 1–4, 2013, pp. 579–615. Available: https://link.springer.com/article/10.1007/s11214-013-9964-y

[2] National Academies of Sciences, Engineering, and Medicine, Testing at the Speed of Light: The State of U.S. Electronic Parts Space Radiation Testing Infrastructure, The National Academies Press, Washington, DC, 2018. Available: https://www.nationalacademies.org/publications/24993

[3] Wertz, J. R., Everett, D. F., and Puschell, J. J., Space Mission Engineering: The New SMAD, Microcosm Press, El Segundo, CA, 2011.

[4] NASA, Mission Radiation Environment Modeling and Analysis, NASA Technical Report, 2022. Available: https://ntrs.nasa.gov/api/citations/20220011775/downloads/Mission_Radiation_Modeling_STI.pdf

[5] Angelopoulos, V., Tsai, E., Bingley, L., Shaffer, C., Turner, D. L., Runov, A., Li, W., Liu, J., Artemyev, A. V., Zhang, X.-J., Strangeway, R. J., Wirz, R. E., Shprits, Y. Y., Sergeev, V. A., Caron, R. P., Chung, M., Cruce, P., Greer, W., Grimes, E., Hector, K., Lawson, M. J., Leneman, D., Masongsong, E. V., Russell, C. L., Wilkins, C., Hinkley, D., and Blake, J. B., "The ELFIN Mission," Space Science Reviews, Vol. 216, No. 5, 2020. Available: https://link.springer.com/article/10.1007/s11214-020-00721-7

[6] Kanekal, S. G., Baker, D. N., Fennell, J. F., Blake, J. B., and Spence, H. E., "CeREs: The Compact Radiation Belt Explorer," Proceedings of the AIAA/USU Conference on Small Satellites, Logan, UT, 2018. Available: https://digitalcommons.usu.edu/smallsat/2018/all2018/259/

[7] European Space Agency, "Space Environment Information System (SPENVIS)," Available: https://www.spenvis.oma.be, retrieved Aug. 27, 2025.

[8] Hevner, R., Puig-Suari, J., Twiggs, R. J., and Kitts, C. A., "An Advanced Standard for CubeSats," Proceedings of the AIAA/USU Conference on Small Satellites, SSC11-V-2, Logan, UT, 2011. Available: https://digitalcommons.usu.edu/smallsat/2011/all2011/35/

[9] nanosats.eu, "CubeSat Size Statistics by Mission and Launch Status," Available: https://www.nanosats.eu, retrieved Aug. 27, 2025.

[10] NASA, “CubeSat Launch Initiative,” NASA Kennedy Space Center, 2024. Available: https://www.nasa.gov/kennedy/launch-services-program/cubesat-launch-initiative/

[11] Granja, C., Polansky, S., Vykydal, Z., Pospisil, S., Owens, A., Kozacek, Z., and Mellab, K., “The SATRAM Timepix Spacecraft Payload in Open Space on Board the Proba-V Satellite for Wide Range Radiation Monitoring in LEO Orbit,” Planetary and Space Science, Vol. 125, 2016, pp. 114–129. Available: https://www.sciencedirect.com/science/article/pii/S0032063316300112

[12] Holy, T., Jakubek, J., and Pospisil, S., “Radiation Imaging with Timepix Detectors,” Nuclear Instruments and Methods in Physics Research Section A, Vol. 591, No. 1, 2008, pp. 287–290. Available: https://www.sciencedirect.com/science/article/pii/S0168900207024658

[13] NASA, “Advanced Space Radiation Detectors,” NASA Glenn Research Center, 2014. Available: https://www.nasa.gov/glenn/research/advanced-space-radiation-detectors/

[14] Cullimore, B. A., “Thermal Desktop® and RadCAD® Software Overview,” International Conference on Environmental Systems, ICES-2009-01, 2009. Available: https://ttu-ir.tdl.org/items/917b1d68-b990-4ec7-996b-f8d7419b57ae

[15] Cacace, R., D’Agostino, D., Schettino, F., and Giove, D., “Measurement of the Energy Spectrum on LEO,” Electronics, Vol. 11, No. 20, 2022. Available: https://www.mdpi.com/2079-9292/11/20/3390

[16] California Polytechnic State University and Stanford University, CubeSat Design Specification, Rev. 13, Cal Poly SLO, San Luis Obispo, CA, 2020. Available: https://static1.squarespace.com/static/5418c831e4b0fa4ecac1bacd/t/56e9b62337013b6c063a655a/1458157095454/cds_rev13_final2.pdf

[17] Swartwout, M., “CubeSat Database and Lessons Learned from 150 Missions,” Proceedings of the AIAA/USU Conference on Small Satellites, 2013. Available: https://digitalcommons.usu.edu/smallsat/2013/all2013/

[18] Bruhn, E. F., Analysis and Design of Flight Vehicle Structures, Tri-State Offset Co., Cincinnati, OH, 1973.

[19] NASA, “CubeSat Launch Initiative,” NASA Kennedy Space Center, 2024. Available: https://www.nasa.gov/kennedy/launch-services-program/cubesat-launch-initiative/

[20] Arduino, “Arduino Mega 2560 Rev3 Technical Specifications,” Available: https://store.arduino.cc/products/arduino-mega-2560-rev3, 2023

[21] Microchip Technology Inc., ATmega640/1280/1281/2560/2561 Datasheet, 2020. Available: https://ww1.microchip.com/downloads/en/DeviceDoc/ATmega640-1280-1281-2560-2561-Datasheet-DS40002211A.pdf

[22] Arduino, “Arduino Mega 2560 Rev3 Pin Mapping and Hardware Documentation,” Available: https://docs.arduino.cc/retired/hacking/hardware/PinMapping2560/, 2023.

[23] Arduino, “Arduino Mega 2560 Rev3 Schematic,” Arduino Documentation, 2022. Available: https://docs.arduino.cc/resources/schematics/A000067-schematics.pdf

[24] Mouser Electronics, “Arduino Mega 2560 Development Board Technical Specifications,” Mouser Electronics, 2024. Available: https://www.mouser.com/

[25] Analog Devices, LTspice XVII Circuit Simulator User Guide, Analog Devices, Norwood, MA, 2024. Available: https://www.analog.com/en/resources/design-tools-and-calculators/ltspice-simulator.html

[26] Adafruit Industries, “AMS1117 LDO Voltage Regulator Datasheet,” 2023. Available: https://www.adafruit.com/

[27] SparkFun Electronics, “PCB Basics,” SparkFun Engineering Resources, 2023. Available: https://learn.sparkfun.com/tutorials/pcb-basics/all

[28] Pololu Corporation, “Connectors and Cables,” Pololu Engineering Reference, 2023. Available: https://www.pololu.com/category/19/connectors

[29] Mouser Electronics, “Circuit Protection Technical Resources,” Mouser Technical Library, 2024. Available: https://www.mouser.com/technical-resources/

[30] NASA, NASA Systems Engineering Handbook, NASA/SP-2016-6105 Rev. 2, 2016. Available: https://www.nasa.gov/reference/nasa-systems-engineering-handbook/

[31] Adafruit Industries, “Lithium Ion Battery Pack 3.7 V 2200 mAh,” Adafruit Technical Resources, 2024. Available: https://www.adafruit.com/product/1781

[32] Texas Instruments, “TPS63060 High Input Voltage Buck-Boost Converter,” Texas Instruments, 2023. Available: https://www.ti.com/product/TPS63060

[33] Wenzel, J., “Design and Testing of a CubeSat Power Distribution System,” Proceedings of the AIAA/USU Conference on Small Satellites, SSC18-V-07, 2018. Available: https://digitalcommons.usu.edu/smallsat/

[34] Oh, J., “Small Satellite Electrical Power System Architecture and Reliability,” IEEE Aerospace and Electronic Systems Magazine, Vol. 34, No. 5, 2019, pp. 18–27. Available: https://ieeexplore.ieee.org/

[35] Arduino, “SD Library,” Arduino Documentation, 2023. Available: https://docs.arduino.cc/libraries/sd/

[36] Adafruit Industries, “MicroSD Card Breakout Board + Logic Level Shifter,” 2024. Available: https://www.adafruit.com/product/254

[37] SparkFun Electronics, “Serial Peripheral Interface,” SparkFun Engineering Resources, 2023. Available: https://learn.sparkfun.com/tutorials/serial-peripheral-interface-spi/all

[38] Medipix Collaboration, “Timepix,” CERN Medipix Collaboration, 2022. Available: https://medipix.web.cern.ch/technology/timepix

[39] Varadis Ltd., “Radiation Detection Sensors Meet NASA Certification,” Varadis Ltd., 2023. Available: https://www.varadis.com/varadis-radiation-detection-sensors-meet-nasa-certification/

[40] Varadis Ltd., “Radiation Sensor Products,” Varadis Ltd., 2023. Available: https://www.varadis.com/

[41] Stanič, S., “RadFET Sensor Package Photograph,” University of Nova Gorica High Energy Physics Lab, Slovenia, 2022. Available: https://www2.ung.si/~sstanic/belle/radfet/photo-radfet/radfet-1.jpg

[42] Holmes-Siedle, A., and Adams, L., “RADFET: A Review of the Use of Metal-Oxide-Silicon Devices as Integrating Dosimeters,” Radiation Physics and Chemistry, Vol. 28, No. 2, 1986, pp. 235–244. Available: https://www.osti.gov/etdeweb/biblio/5883642

[43] Cook, R. D., Malkus, D. S., Plesha, M. E., and Witt, R. J., Concepts and Applications of Finite Element Analysis, 4th ed., John Wiley & Sons, New York, NY, 2002.

[44] Bathe, K. J., Finite Element Procedures, Prentice Hall, Upper Saddle River, NJ, 1996.

[45] Zienkiewicz, O. C., Taylor, R. L., and Zhu, J. Z., The Finite Element Method: Its Basis and Fundamentals, 7th ed., Butterworth-Heinemann, Oxford, UK, 2013.

[46] Dassault Systèmes, SolidWorks Simulation User Guide, Waltham, MA, 2024. Available: https://help.solidworks.com/

[47] NASA, Structural Design and Test Factors of Safety for Spaceflight Hardware, NASA-STD-5001B, 2016. Available: https://standards.nasa.gov/standard/NASA/NASA-STD-5001

[48] Anderson, J. D., Computational Fluid Dynamics: The Basics with Applications, McGraw-Hill, New York, NY, 1995.

[49] Versteeg, H. K., and Malalasekera, W., An Introduction to Computational Fluid Dynamics: The Finite Volume Method, 2nd ed., Pearson Education, Harlow, UK, 2007.

[50] Wilcox, D. C., Turbulence Modeling for CFD, 3rd ed., DCW Industries, La Cañada, CA, 2006.

[51] Launder, B. E., and Spalding, D. B., “The Numerical Computation of Turbulent Flows,” Computer Methods in Applied Mechanics and Engineering, Vol. 3, No. 2, 1974, pp. 269–289. Available: https://www.sciencedirect.com/science/article/pii/0045782574900292

[52] Pope, S. B., Turbulent Flows, Cambridge University Press, Cambridge, UK, 2000.

[53] White, F. M., Fluid Mechanics, 8th ed., McGraw-Hill Education, New York, NY, 2016.

[54] Bird, G. A., Molecular Gas Dynamics and the Direct Simulation of Gas Flows, Oxford University Press, Oxford, UK, 1994.

[55] ANSYS, Inc., ANSYS Fluent Theory Guide, Release 2024 R1, Canonsburg, PA, 2024. Available: https://ansyshelp.ansys.com/

Appendix A: Arduino Pin Mapping

Pin Number	Pin Name	Mapped Pin Name
1	PG5 (OC0B)	Digital pin 4 (PWM)
2	PE0 (RXD0/PCINT8)	Digital pin 0 (RX0)
3	PE1 (TXD0)	Digital pin 1 (TX0)
4	PE2 (XCK0/AIN0)	
5	PE3 (OC3A/AIN1)	Digital pin 5 (PWM)
6	PE4 (OC3B/INT4)	Digital pin 2 (PWM)
7	PE5 (OC3C/INT5)	Digital pin 3 (PWM)
8	PE6 (T3/INT6)	
9	PE7 (CLKO/ICP3/INT7)	
10	VCC	VCC
11	GND	GND

12	PH0 (RXD2)	Digital pin 17 (RX2)
13	PH1 (TXD2)	Digital pin 16 (TX2)
14	PH2 (XCK2)	
15	PH3 (OC4A)	Digital pin 6 (PWM)
16	PH4 (OC4B)	Digital pin 7 (PWM)
17	PH5 (OC4C)	Digital pin 8 (PWM)
18	PH6 (OC2B)	Digital pin 9 (PWM)
19	PB0 (SS/PCINT0)	Digital pin 53 (SS)
20	PB1 (SCK/PCINT1)	Digital pin 52 (SCK)
21	PB2 (MOSI/PCINT2)	Digital pin 51 (MOSI)
22	PB3 (MISO/PCINT3)	Digital pin 50 (MISO)
23	PB4 (OC2A/PCINT4)	Digital pin 10 (PWM)
24	PB5 (OC1A/PCINT5)	Digital pin 11 (PWM)

25	PB6 (OC1B/PCINT6)	Digital pin 12 (PWM)
26	PB7 (OC0A/OC1C/PCINT7)	Digital pin 13 (PWM)
27	PH7 (T4)	
28	PG3 (TOSC2)	
29	PG4 (TOSC1)	
30	RESET	RESET
31	VCC	VCC
32	GND	GND
33	XTAL2	XTAL2
34	XTAL1	XTAL1
35	PL0 (ICP4)	Digital pin 49
36	PL1 (ICP5)	Digital pin 48
37	PL2 (T5)	Digital pin 47

38	PL3 (OC5A)	Digital pin 46 (PWM)
39	PL4 (OC5B)	Digital pin 45 (PWM)
40	PL5 (OC5C)	Digital pin 44 (PWM)
41	PL6	Digital pin 43
42	PL7	Digital pin 42
43	PD0 (SCL/INT0)	Digital pin 21 (SCL)
44	PD1 (SDA/INT1)	Digital pin 20 (SDA)
45	PD2 (RXDI/INT2)	Digital pin 19 (RX1)
46	PD3 (TXD1/INT3)	Digital pin 18 (TX1)
47	PD4 (ICP1)	
48	PD5 (XCK1)	
49	PD6 (T1)	
50	PD7 (T0)	Digital pin 38

51	PG0 (WR)	Digital pin 41
52	PG1 (RD)	Digital pin 40
53	PC0 (A8)	Digital pin 37
54	PC1 (A9)	Digital pin 36
55	PC2 (A10)	Digital pin 35
56	PC3 (A11)	Digital pin 34
57	PC4 (A12)	Digital pin 33
58	PC5 (A13)	Digital pin 32
59	PC6 (A14)	Digital pin 31
60	PC7 (A15)	Digital pin 30
61	VCC	VCC
62	GND	GND
63	PJ0 (RXD3/PCINT9)	Digital pin 15 (RX3)

64	PJ1 (TXD3/PCINT10)	Digital pin 14 (TX3)
65	PJ2 (XCK3/PCINT11)	
66	PJ3 (PCINT12)	
67	PJ4 (PCINT13)	
68	PJ5 (PCINT14)	
69	PJ6 (PCINT 15)	
70	PG2 (ALE)	Digital pin 39
71	PA7 (AD7)	Digital pin 29
72	PA6 (AD6)	Digital pin 28
73	PA5 (AD5)	Digital pin 27
74	PA4 (AD4)	Digital pin 26
75	PA3 (AD3)	Digital pin 25
76	PA2 (AD2)	Digital pin 24

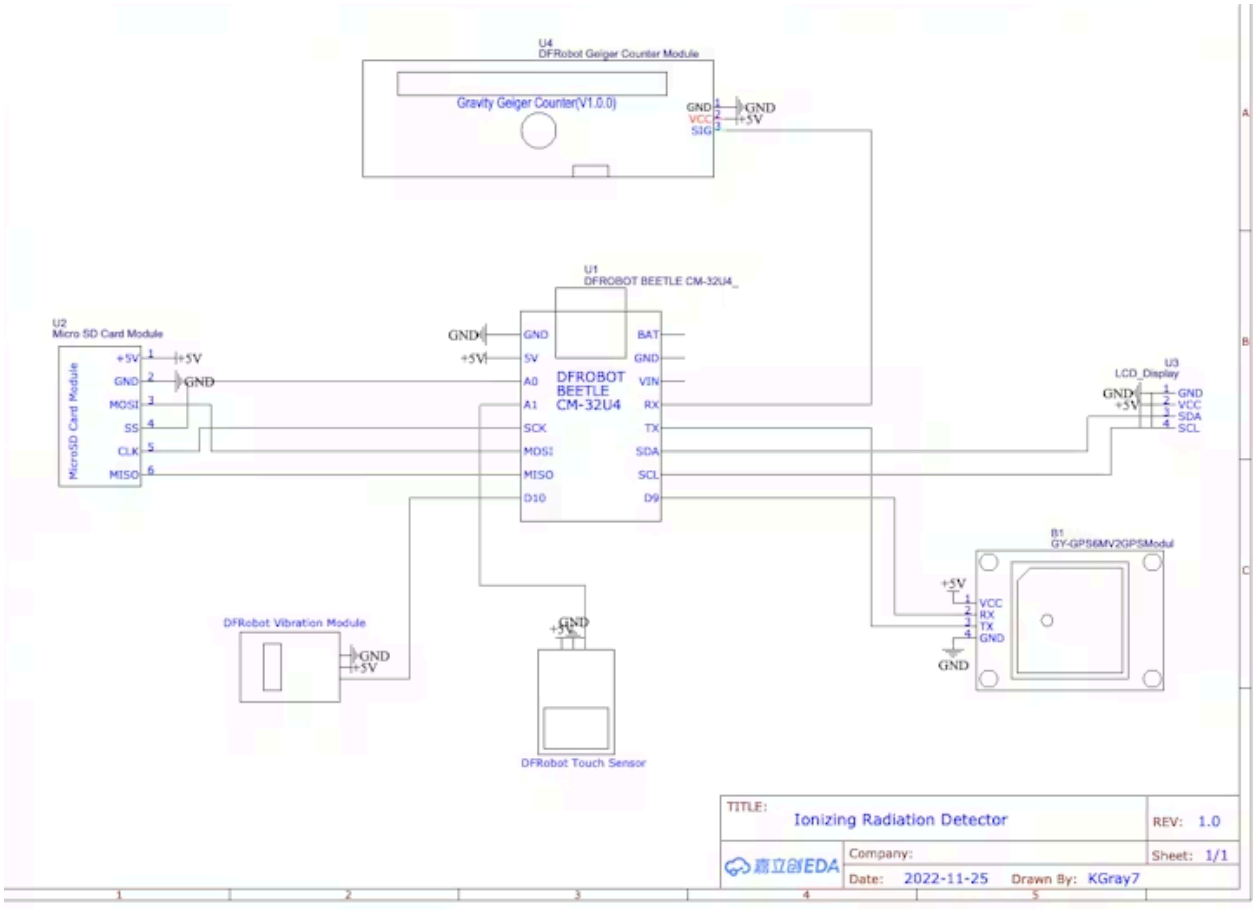
77	PA1 (AD1)	Digital pin 23
78	PA0 (AD0)	Digital pin 22
79	PJ7	
80	VCC	VCC
81	GND	GND
82	PK7 (ADC15/PCINT23)	Analog pin 15
83	PK6 (ADC14/PCINT22)	Analog pin 14
84	PK5 (ADC13/PCINT21)	Analog pin 13
85	PK4 (ADC12/PCINT20)	Analog pin 12
86	PK3 (ADC11/PCINT19)	Analog pin 11
87	PK2 (ADC10/PCINT18)	Analog pin 10
88	PK1 (ADC9/PCINT17)	Analog pin 9
89	PK0 (ADC8/PCINT16)	Analog pin 8

90	PF7 (ADC7/TDI)	Analog pin 7
91	PF6 (ADC6/TDO)	Analog pin 6
92	PF5 (ADC5/TMS)	Analog pin 5
93	PF4 (ADC4/TCK)	Analog pin 4
94	PF3 (ADC3)	Analog pin 3
95	PF2 (ADC2)	Analog pin 2
96	PF1 (ADC1)	Analog pin 1
97	PF0 (ADC0)	Analog pin 0
98	AREF	Analog Reference
99	GND	GND
100	AVCC	VCC

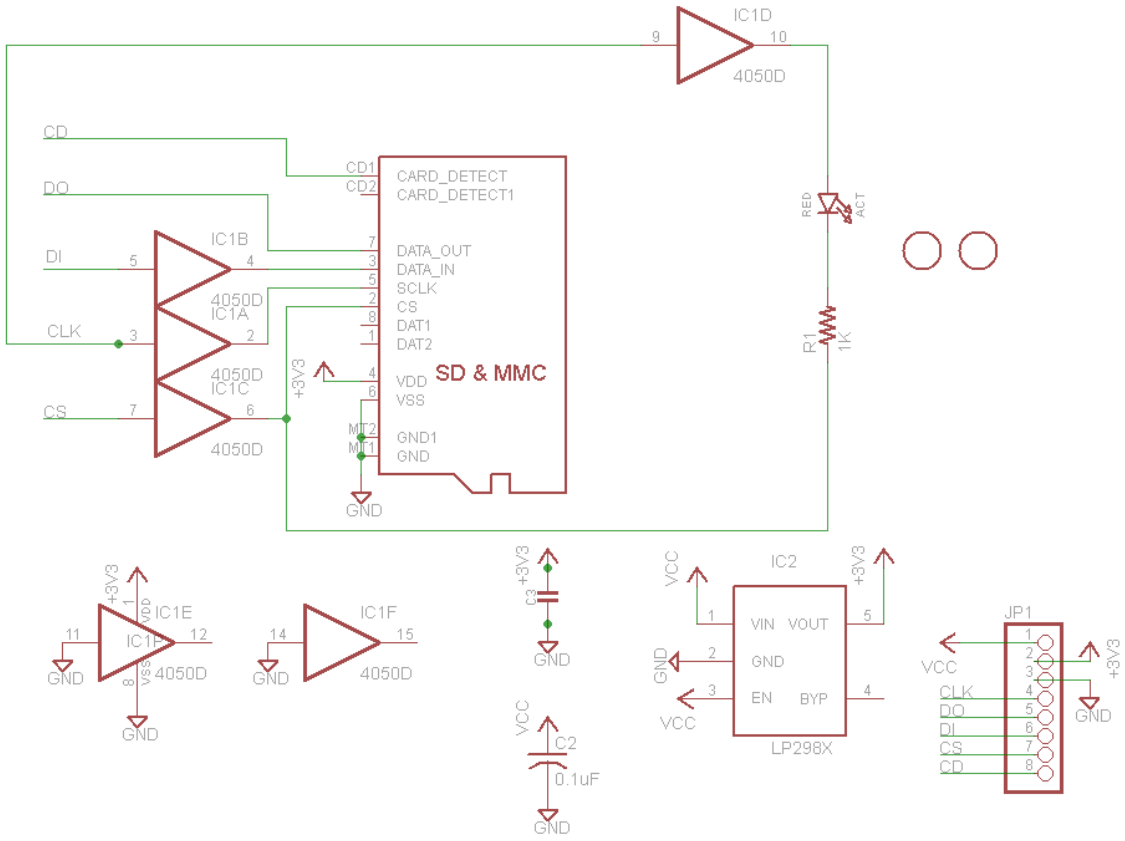
Appendix B: RadFET Pin Description

Pin No.	Pin name	Pin type	Description / Recommendations
1	Vdd	POWER	Positive power supply, this pin must be decoupled with 10 µF ceramic, low ESR capacitor.
2	GND	GND	Connect to power supply ground.
3	GND	GND	Connect to power supply ground.
4	CTRL_R2	Digital IN	RADFET R2 selection signal.
5	CTRL_EN	Digital IN	Enable signal.
6	CTRL_R1	Digital IN	RADFET R1 selection signal.
7	NC	-	Not connected; this pin should be left floating or connected to GND.
8	NC	-	Not connected; this pin should be left floating.
9	RADFET_OUT	Analog OUT	VT01 RADFET output voltage, selectable via control signals.
10-20	NC	-	Not connected; these pins can be left floating or connected to GND.

Appendix C: Radiation Detector Schematic



Appendix D: Micro SD Card Schematic



Appendix E: Arduino Code

```
#include <DFRobot_Geiger.h>

#if defined(ESP32)

  #define detect_pin D3

#else

  #define detect_pin 3   // Uno: D3. If you wired signal to D2, change to
2.

#endif

DFRobot_Geiger geiger(detect_pin);

// Choose your sample interval (ms)

const unsigned long SAMPLE_MS = 3000;


unsigned long t0_ms = 0;

void setup() {

  Serial.begin(115200);

  geiger.start();

  t0_ms = millis();

  // CSV header (makes Excel/Python happy)

  Serial.println("time_s,CPM,uSv_h");

}


void loop() {

  delay(SAMPLE_MS);

  float time_s = (millis() - t0_ms) / 1000.0;

  uint16_t cpm = geiger.getCPM();

  float uSv = geiger.getuSvh();

  // CSV row
```

```
  Serial.print(time_s, 1);
  Serial.print(",");
  Serial.print(cpm);
  Serial.print(",");
  Serial.println(uSv, 3);
}
```